

# UC Berkeley

## UC Berkeley Electronic Theses and Dissertations

### Title

Fundamental Studies of Lithium-Sulfur Reaction Intermediates

### Permalink

<https://escholarship.org/uc/item/7cf5q177>

### Author

Wang, Dunyang

### Publication Date

2018

Peer reviewed|Thesis/dissertation

Fundamental Studies of Lithium-Sulfur Reaction Intermediates

By

Dunyang Wang

A dissertation submitted in partial satisfaction of the requirements for the degree of

Doctor of Philosophy in

Engineering - Materials Science and Engineering

in the

Graduate Division of the

University of California, Berkeley

Committee in charge:

Professor Nitash Balsara, Co-Chair

Professor Andrew Minor, Co-Chair

Professor Kristin Persson

Professor Bryan McCloskey

Summer 2018

Fundamental Studies of Lithium-Sulfur Reaction Intermediates

© 2018

by Donyang Wang

## Abstract

### Fundamental studies of lithium-sulfur reaction intermediates

by

Dunyang Wang

Doctor of Philosophy in Engineering - Materials Science and Engineering

University of California, Berkeley

Professor Nitash Balsara, Co-Chair

Professor Andrew Minor, Co-Chair

Lithium-sulfur (Li-S) batteries have been considered as an attractive alternative to current Li-ion batteries due to their large theoretical capacity (1672 mA-h/g) and theoretical energy density (2600 Wh/kg) while having a low cost, an abundance of the material, and relatively non-toxic properties. However, the low cyclability and significant capacity fading during the first several cycles prevent Li-S rechargeable batteries from being commercialized. During discharge, elemental sulfur is reduced to the final product  $\text{Li}_2\text{S}$  through a series of soluble intermediate species, lithium polysulfides ( $\text{Li}_2\text{S}_x$ ,  $2 \leq x \leq 8$ ). Lithium polysulfides dissolved into the electrolyte in the separator can no longer participate in redox reductions, resulting in a loss of active materials, as well as a “shuttling effect” that causes capacity fading and low coulombic efficiency. Despite the fact that decades of research have attempted to solve this, the problem is still not resolved due to a lack of fundamental understanding of the system. This includes how lithium polysulfides are produced during discharge interactions with other components in the cell and the reaction mechanisms (the electrochemical and chemical processes) during cycling. The objective of this dissertation is to provide a fundamental understanding of lithium polysulfides produced during discharge of a Li-S cell. This is an essential piece of knowledge when designing and identifying the issues associated with Li-S batteries.

To begin, the morphology, thermal properties, and ionic conductivity of an ether-based nanostructured block copolymer containing lithium polysulfides were investigated. Previous work has shown that nanostructured block copolymer electrolytes containing an ion-conducting block and modulus-strengthening block has the potential of enabling solid-state lithium metal rechargeable batteries. This is of particular interest for a lithium-sulfur battery to fully explore its high energy density and capacity. Understanding the thermal and electrochemical properties of these block copolymer electrolytes containing lithium polysulfides is essential for evaluating their potential use in Li-S batteries. A systematic study of polystyrene-*b*-poly(ethylene oxide) (SEO) block copolymer mixed with  $\text{Li}_2\text{S}_x$  with an average  $x$  value of 4 and 8 was conducted. Small angle

X-ray scattering, differential scanning calorimetry, and ac impedance spectroscopy were used to measure the morphology, thermal properties, and ionic conductivities of all samples. The ionic conductivity of SEO/Li<sub>2</sub>S<sub>x</sub> mixtures were compared with those of poly(ethylene oxide) (PEO) mixed with Li<sub>2</sub>S<sub>x</sub> to quantify the effect of nanostructuring on ion transport. The conductivities of both SEO and PEO samples containing polysulfides with a longer average chain length higher than the same polymer containing polysulfides with a shorter average chain length at all salt concentrations, indicating that dissociation of long-chain polysulfides occurs more readily than short-chain polysulfides. Normalized conductivity was used to quantify the effect of morphology on ion transport. The results showed that SEO suppressed the migration of polysulfides relative to PEO. However, this suppression is inadequate for practical applications. In other words, cathode architectures that prevent polysulfides from entering the electrolyte are necessary for enabling Li-S batteries with block copolymer electrolytes. Nevertheless, the results obtained in this study are important as they enable quantification of polysulfide migration in Li-S batteries with imperfect polysulfide encapsulation, a limitation that applies to all known Li-S batteries.

Next, UV-vis spectroscopy with radiation wavelength in the range 200 - 800 nm was used to study different polysulfides in ether. Ex-situ UV-vis spectra were measured for chemically synthesized lithium polysulfides in TEGDME, Li<sub>2</sub>S<sub>x<sub>mix</sub></sub> | TEGDME solutions for x<sub>mix</sub> values of 4, 6, 8, and 10 and sulfur concentrations of 10, 50, and 100 mM. The peaks are generally more resolved at lower concentrations than at higher concentrations for all x<sub>mix</sub> values, suggesting a concentration dependence of spectra shape. The peak at 617 nm was used to confirm the existence of S<sub>3</sub><sup>•-</sup> radical anion, which supports the argument that polysulfide radical anions are stable in ether-based electrolytes, and may play an important role in Li-S reaction mechanism. Using in-situ UV-vis method was discussed and challenges for Li-S reaction mechanism study were evaluated. A new fluorinated-ether based electrolyte was explored. Its low polysulfide solubility makes it a good candidate to be used in in-situ Li-S reaction studies because UV-vis radiations do not have a large penetration path through high concentration of polysulfide-containing materials. However, the main challenge in using UV-vis spectroscopy to study Li-S reaction mechanism is the ambiguity in peak assignments arised both from a lack of spectra standards for different polysulfides. It is difficult to experimentally obtain polysulfide spectra standards because polysulfides cannot be separated.

The need for optical spectra standards for lithium polysulfides motivated a computational project to simulate optical spectra for different polysulfides solvated in ether theoretically. Configurations of a pure lithium polysulfide species can be obtained using computational methods, which circumvents the issue related to obtaining experimental spectrum for a pure polysulfide. Calculating optical spectra requires the calculation of both ground state and various excited states of solvated lithium polysulfides and this is not trivial work. The main goal was to find out the complexity necessary to compute reliable optical spectra for solvated lithium polysulfides using Time-Dependent Density Functional Theory. The configurations of lithium polysulfides solvated in diglyme were obtained using first-principles molecular dynamics simulations in a previous work. Gaussian calculations revealed that solvent played an important role in the calculated spectra and that explicit solvent molecules were needed to capture the local solvent-solution interactions.

The results calculated with Gaussian approximations were compared to those calculated with plane-wave approximations and the two methods were comparable at their most optimized state. For a large system such as lithium polysulfides with explicit ether solvents, plane-wave calculations are efficient at achieving numerical convergence. However, a high level of functional to approximate the exchange-correlation function such as cam-b3lyp or higher is needed to calculate physically representative optical spectra for solvated lithium polysulfides and the scientific community currently lacks the computational power to do these calculations.

X-ray Absorption (XAS) has the power of being elemental specific and detecting both amorphous and crystalline sulfur-containing species. The recent simulation by Pascal et al.<sup>1</sup> also provided a reliable set of spectral standards for species analysis. With the foundation of previous work, an in operando XAS study of a solid-state Li-S cell was conducted where all sulfur-containing species through the entire depth of a Li-S cell were detected.  $\text{Li}_2\text{S}_8$  was used as active material inside cathode instead of  $\text{S}_8$  to provide better contact between the active materials and the solid electrolyte. In operando XAS spectra were taken before and throughout the charge-discharge cycle. Inefficiency in the initial charge revealed that lithium polysulfide dissolved into the separator layer reacted with lithium metal at the anode. The relationship between the average discharge polysulfide chain length inside the cathode,  $x_{\text{avg,cathode}}$ , and the number of electrons passed per S atom,  $n_e$ , at different stages of discharge was evaluated. During the first voltage plateau, while a small amount of  $\text{S}_8$  was converted to  $\text{Li}_2\text{S}_8$ , the major electrochemical reaction was the reduction of  $\text{Li}_2\text{S}_8$  to  $\text{Li}_2\text{S}_6$  (about 75%). During the transition region between the two plateaus,  $\text{Li}_2\text{S}_8$  continued to be reduced to  $\text{Li}_2\text{S}_6$  while almost half of  $\text{Li}_2\text{S}_6$  was reduced to  $\text{Li}_2\text{S}_4$ . Evidence of the formation of  $\text{Li}_2\text{S}$  was observed from the beginning of the second voltage plateau, which supports the argument that chemical disproportionation reactions play an important role in the formation of  $\text{Li}_2\text{S}$ . The challenge of using XAS to study Li-S reaction mechanism is the similarity in the peak locations for different lithium polysulfides which makes it difficult to distinguish between different polysulfides. A spectroscopy with simple distinctive peaks for different polysulfides and well-established spectra standards would be better for Li-S reaction mechanism study.

## Table of Contents

Table of Contents .....	i
List of Figures .....	iii
Acknowledgements .....	v
Chapter 1 – Introduction .....	1
1.1 Background .....	1
1.2 Li – S batteries .....	2
1.3 Li – S battery problems .....	3
1.4 Reaction Mechanism review .....	4
1.5 Reactions proposed in literature .....	5
1.6 Outline of dissertation .....	6
1.7 Supporting Information .....	7
Chapter 2 – Conductivity of Block Copolymer Electrolytes Containing Lithium Polysulfides.....	8
2.1 Introduction .....	8
2.2 Experimental Section .....	10
2.2.1 Materials .....	10
2.2.2 Sample Preparation.....	10
2.2.3 Small-Angle X-ray Scattering (SAXS) .....	11
2.2.4 Differential Scanning Calorimetry (DSC).....	12
2.2.5 AC Impedance Spectroscopy.....	12
2.2.6 X-ray Absorption Spectroscopy (XAS).....	13
2.3 RESULTS AND DISCUSSION .....	15
2.3.1 Morphology .....	15
2.3.2 Thermal Properties .....	16
2.3.3 Electrochemical Properties .....	19
2.4 Conclusions .....	25
2.5 Acknowledgements .....	26
2.6 Supporting Information .....	27
Chapter 3 – Experimental Uv-vis Spectra of Solvated Lithium Polysulfides .....	28
3.1 Background .....	28
3.2 Ex-situ UV-vis Study on lithium polysulfides dissolved in ether .....	31
3.2.1 Lithium polysulfide solution preparation .....	31

3.2.2 UV–vis Spectroscopy measurements .....	31
3.2.3 Ex-situ UV-vis spectra for lithium polysulfides dissolved in TEGDME.....	32
3.3 In-situ UV-vis Setup for Li-S Mechanism Study .....	35
3.3.1 Reported in-situ Li-S study using UV-vis Spectroscopy.....	35
3.3.2 Perfluoropolyether electrolyte .....	36
3.3.3 Challenges with in-situ UV-vis study for Li-S reactions .....	38
3.4 Conclusions .....	39
3.5 Acknowledgements .....	39
Chapter 4 – Computational Optical Spectra of Solvated Lithium Polysulfides .....	40
4.1 Introduction .....	40
4.2 Structures.....	40
4.3 Results and Discussion.....	41
4.3.1 Gaussian Calculations: Basis set and Functionals.....	41
4.3.2 Gaussian Calculations: Solvent Effect .....	42
4.3.3 Plane-wave calculations .....	46
4.4 Conclusions .....	49
4.5 Acknowledgements .....	49
4.6 Supporting Information .....	50
Chapter 5. Discharge Mechanism in a Solid-State Lithium-Sulfur Cell by Operando X-ray Absorption Spectroscopy .....	51
5.1 Introduction .....	51
5.2 Experimental Section .....	53
5.3 Results and Discussion.....	55
5.3.1 Theoretical XAS spectra analysis.....	55
5.3.2 Total Sulfur signal .....	<b>Error! Bookmark not defined.</b>
5.3.3 Discharge products from spectra .....	<b>Error! Bookmark not defined.</b>
5.3.4 Relating average discharge products to $n_e$ .....	60
5.4 Conclusion.....	67
5.5 Acknowledgements .....	67
5.6 Supporting Information .....	68
Chapter 6 – Summary .....	70
Chapter 7 – References .....	72



## List of Figures

Figure 1.1 Theoretical Specific Energy for different rechargeable battery systems.....	1
Figure 1.2 Schematic of a Li-S cell in its charged stage.....	2
Figure 1.3 Typical discharge voltage profile for a Li-S cell.....	3
Figure 2.1 Typical simulation results of lithium polysulfide configurations in ether .....	11
Figure 2.2 Equivalent circuit and experimental Nyquist plot for determining the ionic resistance of the polymer/salt electrolytes with blocking electrodes.....	13
Figure 2.3 SAXS profiles and domain spacing for SEO/Li <sub>2</sub> S <sub>x</sub> samples.....	15
Figure 2.4 DSC profiles and crystallinity for SEO/Li <sub>2</sub> S <sub>x</sub> samples .....	16
Figure 2.5 Melting temperatures for SEO/Li <sub>2</sub> S <sub>x</sub> samples and PEO/Li <sub>2</sub> S <sub>x</sub> samples .....	17
Figure 2.6 Glass transition temperatures for SEO/Li <sub>2</sub> S <sub>x</sub> samples and PEO/Li <sub>2</sub> S <sub>x</sub> samples .....	18
Figure 2.7 Ionic conductivity for polymer/salt mixtures .....	19
Figure 2.8 Ionic conductivity vs domain spacing for SEO/Li <sub>2</sub> S <sub>x</sub> samples .....	21
Figure 2.9 Temperature dependence of normalized conductivity for SEO/salt samples.....	22
Figure 2.10 Temperature dependence coefficient of normalized conductivity for SEO/salt samples.....	22
Figure 2.11 Temperature-averaged normalized conductivity for SEO/salt samples .....	23
Figure 2.12 Suppression of migration of SEO compared to PEO .....	24
Figure 2.13 XAS spectra of PEO/Li <sub>2</sub> S <sub>x</sub> samples at various temperatures .....	25
Figure S2.1 DSC profiles and crystallinity for PEO/Li <sub>2</sub> S <sub>x</sub> samples .....	27
Figure S2.2 Expanded view of DSC profiles for PEO/Li <sub>2</sub> S <sub>8</sub> samples showing T <sub>g</sub> .....	27
Figure 3.1 Photographs of UV–Vis Cuvettes Filled with Li <sub>2</sub> S <sub>x<sub>mix</sub></sub>   TEGDME Solutions.....	32
Figure 3.2 UV–vis spectra for lithium polysulfides dissolved in TEGDME solutions at various sulfur concentrations.....	33
Figure 3.3 Chemical structure for perfluoropolyether .....	36
Figure 3.4 Schematic of ex-situ UV-vis measurement for a Li-S cell containing PFPE electrolyte .....	36
Figure 3.5 UV-vis transmission spectra of Li-S cell electrolyte with and without PFPE electrolyte layer after 5 cycles.....	37
Figure 3.6 Schematic of in-situ UV-vis setup for Li-S reaction mechanism study using PFPE electrolyte.....	38
Figure 4.1 Different basis sets and functionals used to calculate Li <sub>2</sub> S Spectra .....	41
Figure 4.2 Schematic of an S <sub>8</sub> molecule with implicit solvent around it.....	42
Figure 4.3 Comparing calculations of vacuum vs implicit solvent model .....	43
Figure 4.4 Schematic of adding explicit molecules into the calculation .....	44
Figure 4.5 Calculated uv-vis spectra for Li <sub>2</sub> S in diglyme with different number of solvent molecules .....	45
Figure 4.6 Experimental spectra of Li <sub>2</sub> S in diglyme.....	46
Figure 4.7 Schematic and calculated spectra of repeating unit cells of Li <sub>2</sub> S <sub>3</sub> with two diglyme molecules coordinating the lithium ions in a vacuum box using plane wave method.....	47
Figure 4.8 Comparing plane wave calculations to Gaussian calculations .....	48

Figure 4.9 Schematic of infinitely repeating unit cells of $\text{Li}_2\text{S}_3$ with 27 DMF molecules .....	49
Figure 5.1 Theoretical XAS spectra of solvated $\text{Li}_2\text{S}_x$ , the linear relationship between $x$ for $\text{Li}_2\text{S}_x$ ( $3 \leq x \leq 8$ ) and the area ratio of main-edge peak to pre-edge peak, and the sum of pre-edge and main-edge peak areas per mole of $\text{Li}_2\text{S}_x$ ( $4 \leq x \leq 8$ ) .....	55
Figure 5.2 All raw XAS spectra and relative total sulfur signal before and during cycling .....	56
Figure 5.3 Normalized and self-absorption corrected in operando XAS spectra and (b) voltage profile and average polysulfide chain length during discharge .....	58
Figure 5.4 Illustration of peaks with areas $A_p$ , $A_m$ , and $A_s$ for a discharged spectrum .....	59
Figure 5.5 Formation of $\text{Li}_2\text{S}$ during discharge .....	60
Figure 5.6 Theoretical and experimental average chain length in the cell vs moles of electrons delivered to cathode per mole of $\text{S}_8$ .....	61
Figure 5.7 Theoretical and experimental average chain length in the cathode vs moles of electrons delivered to cathode per mole of $\text{S}_8$ .....	62
Figure 5.8 Average chain length of polysulfides, $\text{Li}_2\text{S}_x$ ( $2 \leq x \leq 8$ ), inside the cathode and molar ratio of $\text{Li}_2\text{S}$ to polysulfides vs moles of electrons delivered to cathode per mole of $\text{S}_8$ .....	63
Figure 5.9 Comparing experimental measures and the predicted values of (a) $x_{\text{avg,cathode}}$ , (b) $x_{\text{avg,PS}}$ , (c) $m_{\text{Li}_2\text{S}}$ , and (d) $n_e$ versus $t$ , time in hours, using the three-reaction model .....	65
Figure 5.10 Concentration profile of $\text{Li}_2\text{S}_8$ , $\text{Li}_2\text{S}_4$ , $\text{Li}_2\text{S}_2$ , and $\text{Li}_2\text{S}$ predicted by model .....	66
Figure S5.1 Example of fitting an experimental XAS spectra with 6 Gaussian functions and an arctangent step function .....	68
Figure S5.2 Example of fitting a theoretical XAS spectra for polysulfides, $\text{Li}_2\text{S}_x$ ( $2 \leq x \leq 8$ ), with Gaussian functions .....	68
Figure S5.3 Fitting theoretical XAS spectra for $\text{Li}_2\text{S}$ with Gaussian functions .....	69

## Acknowledgements

I would like to start by thanking my parents for their love and support throughout my life. They have taught me the values of independence and fortitude with their own behavior ever since I was little. After I came to America they continued to be my life-coach as well as my source of strength. Whenever I felt frustrated during graduate school they would tell me not to complain, but to face whatever problems with courage and wisdom. They constantly reminded me the importance of persistency in any work. I would not be who I am without their love and guidance. I am extremely grateful to be their daughter.

I am grateful to Dr. Nitash Balsara for his guidance and support over the past five year. I am extremely fortunate to have worked with Nitash. Often, I would feel discouraged by the seemingly tedious and dry data, but he had the ability to see beyond the apparent results, explain to me the importance of the data and showed me how to craft an exciting story. I have learned so much about research and life from Nitash. Nitash always thinks the best of his students. He fully trusts all of his students and only speaks of how lucky he is to have good students. He truly cares about all of his students. and always tries his best to make every student feel included and supported in the group. I am very thankful to have had him as my advisor.

With a special mention to my fiancé, Dr. Justin Freedman, who has been extremely supportive over the past five years. Having done a PhD himself, he understands the difficulties of graduate school and has always been there for me through all the highs and lows. When I felt like I wasn't making important contributions to the scientific community he helped me understand the true importance of fundamental research by showing me the ones in history that didn't seem important at the time but made a significant influence years later. When I felt like giving up he would encourage me by sharing the difficulties he went through during his graduate school. Though he is a true workaholic, he loves hiking and skiing with me and would always encourage me to do out-door activities to brighten my mood when I feel down.

I would like to thank those who I worked closely with on this project. Dr. Kevin Wujcik was the first person in our lab to start on the lithium-sulfur reaction mechanism project. He taught me not only about lithium-sulfur and XAS, but also about designing and building parts. I learned to become a better researcher from observing his hard-working attitude, perseverance in problem solving, and patience in readings and writings. Kevin has been a great colleague, friend, and mentor to me. I would also like to thank Dr. David Prendergast, Dr. Tod Pascal, and Dr. Kristi Closser, who have helped tremendously in my learning of computational work. Coming from an experimental group I had no knowledge about computational simulations, but Tod provided tremendous guidance to me. Kristi was always so patient at answering my questions and would always be there to help me with coding problems. David was like an adviser to me while I worked on computational simulations. From him I learned about the complexity of theoretical calculations and how to present my work confidently. Deep Shah, a fellow graduate student of the Balsara group, was very helpful in obtaining some of the results shown here. Deep is an intelligent young researcher in the group. I am impressed by the work he has done with fluorinated ether electrolytes.

Thank you to the beamline scientists who have helped me. Jun Feng was generous and gave me extra time at ALS beamline 5.3.1 during my last year when I was stressed about beamtime. He was accommodating in my need to adjust the beam settings as well. He was always enthusiastic about science and research and was willing to support his users to achieve their research goals. I also thank Erik Nelson and Mathew Lattice at SSRL. They were helpful at the beam setup as well as teaching me how to use the software. Erik also developed a program that automated the spectra acquisition, which made life during the beamtime experiments much easier.

I would like to thank all the members of the Balsara Lab, both past and present. Dr. Chelsea Chen was my mentor in my first year when I worked with TEM. She spent a lot of time teaching me how to image soft materials with using the TEM and supervised me during my first several TEM sessions. Dr. Inna Gurevitch and Dr. Sebnem Inceoglu were inspiring to me for their hard-working attitude and enthusiasm about research. Dr. Nikos Petzetaks and Dr. Pepa Cotanda were patient while explaining the work done by various group members and helped me learn about polymer electrolytes in the beginning of my graduate school. Dr. Didier Devaux was an expert in battery cycling and I was always impressed by how much he knew and I wish I had consulted him more about battery cycling when he was still in the lab. Dr. Mahesh Bhatt was an expert in polymer synthesis and he was helpful at providing useful advice to younger students in the lab. Didier and Mahesh also kept the Building 62 lab well maintained and were always the go-to people when the rest of us were having difficulties with anything in the lab. Dr. Katherine Harry was always a positive influence in the group through her hard-working attitude and critical thinking. Dr. Jacob Thelen was the go-to person if anyone had any questions about polymer scattering. Dr. Mahati Chintapalli was always nice and patient in answering my questions. I enjoyed working alongside with Dr. Chaeyoung Shin, for she was always nice and fun to talk to. I had the opportunity to work with Dr. Adriana Rojas on imaging single-ion conducting polymer during my first year. I was always impressed at how well she organized all her materials. She was also an awesome lab safety coordinator. Dr. Alex Wang had a challenging project during his PhD and I respected his hard-working attitude and persistency in research. Dr. Doug Greer was adventurous. He bravely switched to a completely different project in the middle of his graduate school and did impressive work in both bio-fuel field and peptoid synthesis field. Finally, Dr. Irune Villaluenga was a special resource in the lab as she could synthesize anything you asked her to and always had creative ideas of how to study a system when things seemed to hit a dead-end.

Thank you to the members of the Balsara lab who joined at the same time as me. Danielle Pesko sat beside me and this gave us the opportunity to discuss academic and non-academic topics. She is a talented researcher, as well as a good person. She was organized and clean in her laboratory duties like no one else. I could never believe how clean the fume hoods or the gloveboxes could be until she had cleaned them! Ksenia Timachova was a great colleague to me. At first I found her difficult to get close to, but after being with her for a while, I found her one of the most kind-hearted people I knew. Ksenia has been the most helpful person to me through my two most important presentation preparations; my qualifying exam talk and my job interview talk. I was impressed by how good she was at putting information together and presenting it in an understandable way. She is also a talented skier and I've enjoyed skiing with her.

I would also like to thank the younger students in the group. Jacqueline Maslyn has synthesized various high molecular weight SEO that are essential in all battery related work in our group. I am grateful that she kindly allowed me to use the polymer that she synthesized. Whitney Loo has replaced Jacob to be the expert in polymer scattering in our lab. I am amazed at how she quickly became an expert in SEO synthesis and has become a teacher to other people in our lab on the subject. Gumi Sethi is absolutely a favorite of mine in the Balsara lab. Besides being a great researcher, she is a kind and warm person. No matter how busy she is she is always willing to make time to help. I was touched when she offered to come to a three-day beamtime through a weekend with me to help me with the experiment so I could get some sleep! Michael Galluzzo is bravely exploring using ether-based electrolyte against lithium metal and I am impressed with the progress he has already made. Lorena Grundy and Kevin Gao joined the lab a year ago. They have brought new energy to the lab and have already made progress in their research. I wish them well as they advance the work of the group and carry on the polymer legacy of the Balsara Lab.

I have also benefited from the support of some more recent post docs. Dr. Hee Jeung Oh has done doing interesting research in polymer membranes for biomedical applications. I am so glad that Dr. Louise Frenck came back to our lab after being a temporary visiting scholar in our lab previously. She has brought expertise in the field of battery cycling. I didn't get to work with Dr. Katrina Mongcopa much but I am very impressed by her work in neutron scattering.

Lastly, I would like to thank the Bay Area Ultimate Frisbee community. I spent a great deal of my time playing competitive Ultimate Frisbee, both during the competitive club season in the summers with all experienced players in the Bay Area and the less competitive regular season leagues. Ultimate Frisbee is the one thing that can always brighten me up no matter how stressed or sad I am. I am thankful to Mimosas Ultimate, the club team that I had played with for the past three seasons. When I first moved to the Bay Area, I thought I would never find friends and teammates like the ones I had during college. But it only took me one season to regret not even trying. I am so happy that I joined Mimosas three years ago when the team had just started. To my teammates past and present, thank you all for creating a supportive environment and making this team like a home to me. I treasure all the moments when we practice and fight together, working out conflicts and gain trust in each other, and sharing all the stressful and joyful moments on the field. I look forward to continue playing with all of you for the rest of this season and in the future as long as I am healthy and still in the Bay Area.

## Chapter 1 – Introduction

### 1.1 Background

Rechargeable battery systems with high energy and capacity storage are of great interest today due to a great increase in demand of energy. Li-ion batteries have played central roles in energy storage systems in the past several decades because of their relatively high specific energy density and volumetric energy density compared to lead-acid, nickel-cadmium and nickel metal hydride systems.<sup>2,3</sup> However, the maximum energy density of current Li-ion batteries, even when fully developed, cannot meet the demands of future key energy market, such as transport, in the long term.<sup>4</sup> Therefore, we need to reach beyond Li-ion batteries for systems with new electrochemistry and new materials to achieve higher energy density and capacity. Figure 1.1 compares the theoretical specific energy for several rechargeable battery systems.

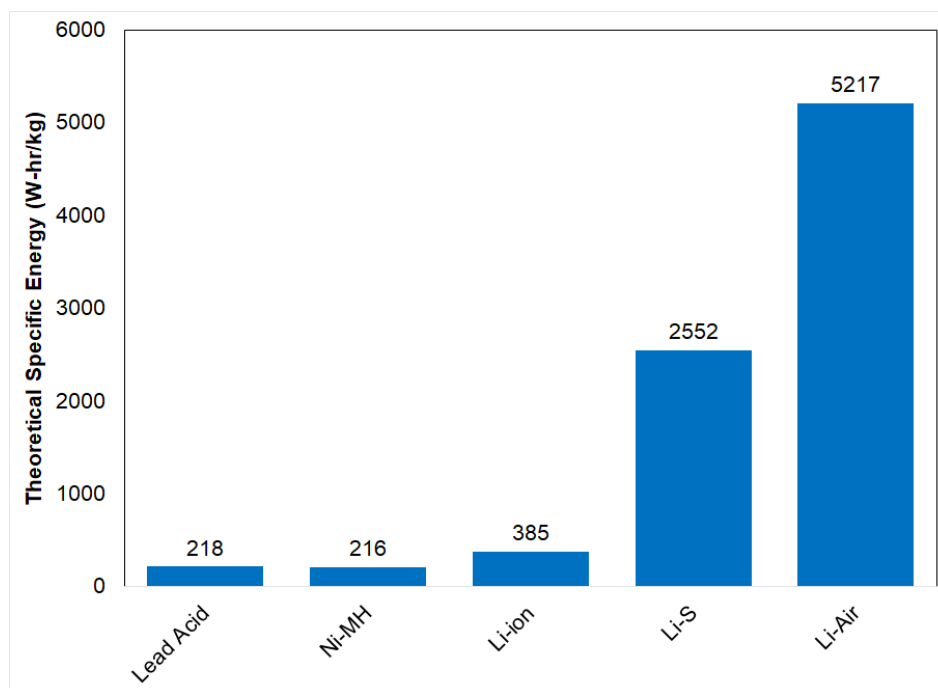


Figure 1.1 Theoretical Specific Energy for different rechargeable battery systems, calculated using the weight of the materials participate in the electrochemical reactions in the supporting information

Current Li-ion batteries use transition metal oxides inside the cathode. These metal oxides have a layered structure that allows lithium ions to be inserted or extracted during charge and discharge, respectively. The large dead weight of these transition metals and the limited amount of lithium they can take limits the theoretical specific energy and capacity. As shown in Figure 1.1, lithium – sulfur (Li-S) and Li-air both have a much larger theoretical specific energy. This arises because  $\text{Li}_2\text{S}$ ,  $\text{Li}_2\text{O}_2$ , the complete discharge product of the two systems, respectively, can store more Li, and hence charge, than  $\text{LiCoO}_2$  per unit mass.<sup>4</sup> While Li-air batteries have the highest theoretical specific energy, major problems need to be solved for them to succeed.<sup>5,6</sup> We focus on Li-S

systems in our study.

## 1.2 Li – S batteries

Figure 1.2 shows a schematic for a typical Li-S cell in its charged state. Lithium metal is used as the anode. The cathode contains elemental sulfur, S<sub>8</sub>, as the actively material, carbon black that facilitates charge transport, and a binder. A separator that only allows ion transport is used to separate the electrodes. An electrolyte facilitate ion transport penetrate through the cathode and the electrolyte. A nickel foil is used as the anode current collector and an aluminum foil used as the cathode current collector. Aluminum is stable with all materials in the cathode, but not with lithium in the anode, while nickel is stable with lithium but not with sulfur.

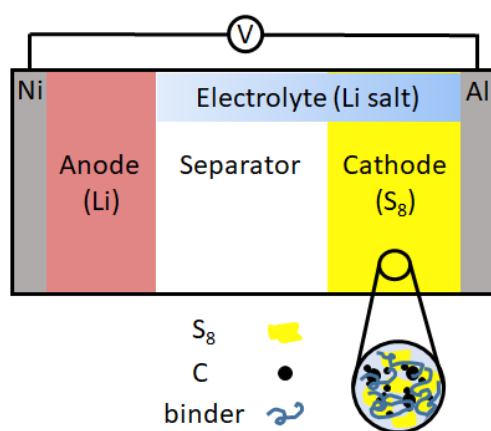


Figure 1.2 Schematic of a Li-S cell in its charged stage

During discharge, Li atoms in the anode dissociate into lithium ions and electrons as shown in equation (1.1). Li<sup>+</sup> ions transport through the separator while electrons transport through an outside circuit to react with S<sub>8</sub> in the cathode. The complete discharge reaction in the cathode is shown in equation (1.2).



The theoretical specific energy for Li-S cell can be calculated based on the free energy of formation,  $\Delta G_f^0$ , of the species in equation (1.2). The values of  $\Delta G_f^0$  for pure elements are zero, while the value of  $\Delta G_f^0$  for Li<sub>2</sub>S is reported to be -422 kJ/mol. (kw review 9) This gives a specific energy density of 2552 Wh/kg for a Li-S cell, five times that of current Li-ion cells.

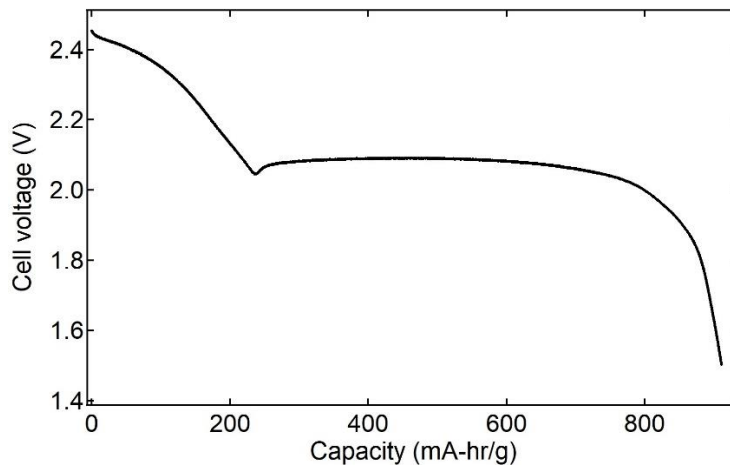


Figure 1.3 Typical discharge voltage profile for a Li-S cell

Figure 1.3 shows a typical discharge voltage profile for a Li-S cell. Here the cell starts at roughly 2.46 V. As S<sub>8</sub> is reduced, the cell voltage goes through three voltage regions: a higher voltage plateau region centered around 2.39 V, a transition region, and a lower voltage plateau centered around 2.09 V. The higher voltage plateau region is ascribed to the reduction of solid S<sub>8</sub> to soluble intermediate species, and the lower plateau region is ascribed to the reduction of soluble intermediate species to insoluble intermediate species as well as solid-phase Li<sub>2</sub>S.<sup>7</sup>

### 1.3 Li – S battery problems

Good battery systems requires the following: high energy storage capability (high specific energy and capacity), low cost, mechanical and chemical stability, a wide temperature range of operation, minimum self-discharge, reversibility upon cycling and long cycle time. Although Li-S batteries have a high theoretical energy storage capability, and sulfur is earthly abundant, low cost, and non-toxic, they face significant challenges in other aspects. First of all, the electronic insulating nature of the active materials, S<sub>8</sub> and Li<sub>2</sub>S, results in unstable electrochemical contact within the cathode.<sup>8</sup> In addition, the electrochemical transformation of S<sub>8</sub> to Li<sub>2</sub>S during discharge, or Li<sub>2</sub>S to S<sub>8</sub> during charge, involves structural changes resulting in loss of contact between the electrolyte and active materials, as well as delamination between the cathode and the separator. There is a 20% increase in volume if all S<sub>8</sub> is converted to Li<sub>2</sub>S due to their density difference. Furthermore, multiple complex intermediate species, called lithium polysulfides, Li<sub>2</sub>S<sub>x</sub> (2 ≤ x ≤ 8), are produced during the electrochemical reduction of S<sub>8</sub>. These polysulfides are highly soluble in most organic electrolytes, and therefore will diffuse out of the cathode and into the separator carried by the electrolyte.<sup>9</sup> Besides a permanent loss of active materials in the cathode, the dissolved Li<sub>2</sub>S<sub>x</sub> species can travel through the separator layer, and reacted with lithium metal at the anode, resulting in “shuttle effect” that compromises cycling life.<sup>10</sup> The undesired reaction site at the anode/separator interface causes self-discharge and decreases the cell capacity during discharge.<sup>11</sup> The shuttle effect also prevents Li-S cells from being charged: while lithium ions and



electrons are being stripped away from the cathode upon charging, aiming to oxidize  $\text{Li}_2\text{S}$  and  $\text{Li}_2\text{S}_x$  back to  $\text{S}_8$ ,  $\text{Li}_2\text{S}_x$  at the anode/separator interface can absorb these ions and electrons and therefore being further reduced, resulting an infinite  $\text{Li}_2\text{S}_x$  oxidation and reduction loop!

Recent work has focused on designing nanostructured cathodes that confine sulfur and polysulfides within the cathode without impeding transport of lithium ions and electrons that are necessary for the redox reactions.<sup>12–15</sup> The nanostructured materials act as hosting matrix for active materials to accommodate the volume change during cycling, as well as to increase their contact with the conducting materials, resulting in improved mechanical stability and cycling life of Li-S cells. However, the diffusion of polysulfides out of the cathode towards the anode and the resulting shuttle effect has not been completely eliminated. One missing key in attempting to solve the polysulfide shuttle problem is the lack of knowledge of the lithium-sulfur redox reaction mechanism. Design mechanism requires a better understanding of the polysulfide intermediate species formed during the redox reactions, such as which species and when they are formed, how much of them are formed and how they interact with other materials within the cathode, in order to provide chemical and physical methods to solve the problem.

#### 1.4 Reaction Mechanism review

In the past decade, different techniques have been used to study the reaction mechanism in Li-S cells. Electrochemical measurements such as cyclic voltammetry (CV) have been popular in relating the number of electrons transferred and the redox reactions upon charge and discharge. For example, Jung et al.<sup>16</sup> used CV to investigate the effects of solvents on the electrochemical reduction of sulfur, and found that solvents had a large effect on the overall electrochemical reactions based on different CV curves and peak potentials. Lu et al.<sup>17</sup> combined CV and a rotating-ring disc electrode (RRDE) technique, and concluded that the mismatch between the number of electrons in reaction products and the number of electrons calculated from RRDE indicate that 80% of the discharge products are from chemical reactions instead of electrochemical reductions. These electrochemical techniques can be powerful in determining the state of charge and discharge based on number of electrons transferred, but lack of the ability to distinguish different reaction products.

X-ray diffraction (XRD) has been used to determine when crystalline species such as  $\text{Li}_2\text{S}$  and  $\text{S}_8$  are formed during discharge and charge, respectively. Using in-situ XRD, Waluś et al.<sup>18</sup> found that after discharging and charging a Li-S cell, the final product is a monoclinic  $\beta$ -sulfur (which is a metastable phase at room temperature) instead of the original orthorhombic  $\alpha$ -sulfur. Different in-situ XRD studies generated different results on the production of  $\text{Li}_2\text{S}$  during discharge. Nelson et al.<sup>19</sup> did not detect any XRD patterns associated with crystalline  $\text{Li}_2\text{S}$  in an ether-based electrolyte, while Lowe et al.<sup>20</sup> and Cañas et al.<sup>21</sup> both detected  $\text{Li}_2\text{S}$  at the very end of the second voltage plateau. On the other hand, Waluś et al.<sup>18</sup> detected crystalline  $\text{Li}_2\text{S}$  throughout the second voltage plateau, and suggested that  $\text{Li}_2\text{S}$  were formed simultaneously with short-chain

polysulfides, contradicting to a generally assumed successive reduction mechanism.

Different spectroscopy have been used to study lithium polysulfides. For example, See at al.<sup>22</sup> used <sup>7</sup>Li NMR spectroscopy to study the evolution of sulfur species and found that the lithium nuclei resonance shifted to a higher frequency as the polysulfide chain length decreased and the concentration increased. However, due to the lack of difference in the frequency shift for different polysulfides, NMR cannot be used to differentiate different polysulfides. Uv-vis<sup>23–25</sup> and Raman<sup>26,27</sup> spectroscopy have been widely used to study Li-S reaction mechanism. While the spectra for different lithium polysulfides have different peak locations, the lack of reliable spectral standards prevent distinguishing the species produced with in-situ studies. X-ray Absorption (XAS) has also been widely used provided with the power of being elemental specific and can detecting both amorphous and crystalline sulfur-containing species. The recent simulation by Pascal et al.<sup>1</sup> provides a reliable set of spectral standards for species analysis, and has been used to interpret experimental spectra.<sup>28</sup> There are a lot of other techniques being used. Each technique has its own advantages and limitations, and cannot alone solve the Li-S reaction mechanism problem.<sup>29</sup> Recent review papers by Zhao et al.<sup>7</sup> and Zheng et al.<sup>10</sup> gave a detailed description and comparison of using these techniques in Li-S reaction mechanism studies.

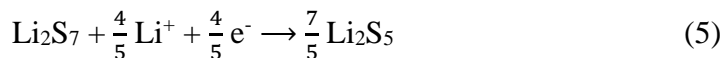
## 1.5 Reactions proposed in literature

The proposed Li-S reaction mechanism differs in literature. Discharge can generally be separated into three categories: the first voltage plateau, the transition region, and the second voltage plateau. Equation (1.3) – (1.22) are the mostly proposed reactions at different stages of discharge. The main product(s) during each stage is bolded.

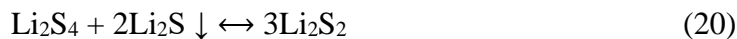
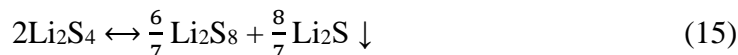
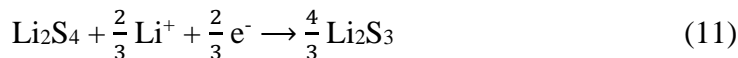
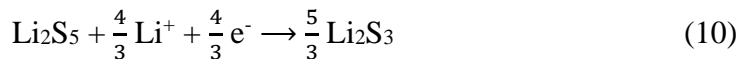
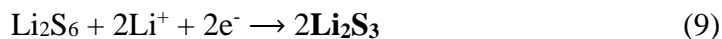
First voltage plateau:



Transition Region:



Second voltage plateau:



## 1.6 Outline of dissertation

In this work, a solid block-copolymer containing salt is used both as the separator and the electrolyte. In Chapter 2, we begin by studying how chemically synthesized lithium polysulfides interact with a polystyrene-b-poly(ethylene oxide) block-copolymer (SEO) electrolyte material. Small-Angle X-ray Scattering (SAXS), Differential Scanning Calorimetry (DSC), and a potentiostat are used to explore the morphology, thermal properties, and ionic conductivities of the SEO/Li<sub>2</sub>S<sub>x</sub> mixture, respectively. The surprising result from this chapter is that solvated lithium polysulfides can dissociate into charged species and affect ion transport in Li-S systems. In Chapter 3, we use UV-vis spectroscopy to examine the optical absorption of lithium polysulfides at different concentration and different Li:S ratio. Lack of spectra standards due to incapability of experimentally separate lithium polysulfides limits our analysis in speciation. In Chapter 4, we aim to compute UV-vis spectra standards for different lithium polysulfides using Time-Dependent Density Functional Theory (TDDFT). We will systematically explore the necessary steps needed to produce physically representative optical spectra in these systems. In Chapter 5, we conduct in operando study of Li-S reactions using sulfur K-edge XAS while discharge and charge a Li-S cell at a constant rate. Computational XAS spectra standards for lithium polysulfides were used to analyze the average discharge products. The relationship between the average polysulfide chain length and the number of electrons passed into the system is evaluated.

## 1.7 Supporting Information

Table 1.1 Reactions used to compute the specific energy in Figure 1.1:

Battery Type	Reactions
Lead-acid	$\text{Pb} + \text{PbO}_2 + 2\text{H}_2\text{SO}_4 \rightarrow 2\text{PbSO}_4 + 2\text{H}_2\text{O}$
Nickel – metal-hydride (Ni-MH)	$\text{Pd}_2\text{H} + \text{NiOOH} \rightarrow 2\text{Pd} + \text{Ni}(\text{OH})_2$
Li-ion	$2\text{Li}_{0.5}\text{CoO}_2 + \text{LiC}_6 \rightarrow 2\text{LiCoO}_2 + \text{C}_6$
Li-S	$\text{S}_8 + 16 \text{Li} \rightarrow 8\text{Li}_2\text{S}$
Li-air	$\text{O}_2 + 2\text{Li} \rightarrow 2\text{Li}_2\text{O}$

## Chapter 2 – Conductivity of Block Copolymer Electrolytes Containing Lithium Polysulfides<sup>†</sup>

### ABSTRACT

Lithium-sulfur batteries are attractive due to their high theoretical specific energy, but the dissolution of lithium polysulfide intermediate species formed during discharge results in capacity fade and limited cycle life. In this study we present the first measurements of ionic conductivity of the polysulfides in a nanostructured block copolymer. The morphology, thermal properties, and the conductivities of polystyrene-*b*-poly(ethylene oxide) (SEO) containing lithium polysulfides,  $\text{Li}_2\text{S}_x$  ( $x=4, 8$ ), were studied using small-angle X-ray scattering (SAXS), differential scanning calorimetry (DSC), and ac impedance spectroscopy. We also measured conductivities of mixtures of poly(ethylene oxide) (PEO) and  $\text{Li}_2\text{S}_x$ . X-ray absorption spectroscopy was used to confirm the nature of dissolved polysulfides. SAXS measurements on SEO/ $\text{Li}_2\text{S}_x$  mixtures indicated that all samples had a lamellar morphology. DSC measurements indicated that SEO/ $\text{Li}_2\text{S}_8$  interactions were more favorable than SEO/ $\text{Li}_2\text{S}_4$  interactions. The effect of nanostructure on transport of  $\text{Li}_2\text{S}_x$  was quantified by calculating a normalized conductivity, which is proportional to the ratio of the conductivity of SEO/ $\text{Li}_2\text{S}_x$  to that of the PEO/ $\text{Li}_2\text{S}_x$ . The normalized conductivities of both polysulfides peaked at intermediate concentrations. The efficacy of block copolymer electrolytes in Li-S batteries was evaluated by comparing ionic conductivities of polymer electrolytes containing  $\text{Li}_2\text{S}_x$  with those containing lithium bis(trifluoromethanesulfonyl)imide (LiTFSI), a common salt used in PEO-based battery electrolytes. The transport of  $\text{Li}_2\text{S}_x$  species in SEO is suppressed by factors ranging from 0.4 to 0.04 relative to LiTFSI, depending on  $x$  and salt concentration. To our knowledge, this study represents the first systematic investigation of the effect of molecular structure of polymer electrolytes on polysulfide migration.

### 2.1 Introduction

There is considerable interest in rechargeable lithium-sulfur batteries because their theoretical specific energy, 2600 Wh/kg, is five times greater than that of current lithium-ion batteries.<sup>30,31</sup> Elemental sulfur is abundant, nontoxic, and inexpensive compared to cobalt- and iron-based cathodes in conventional lithium-ion batteries.<sup>31</sup> There are, however, many challenges that must be addressed before lithium-sulfur batteries become a commercial reality.<sup>32</sup> During the discharge of lithium-sulfur batteries, lithium polysulfide intermediates with chemical formulae  $\text{Li}_2\text{S}_x$  where  $x$  ranges from 2 to 8, are formed. Some of these polysulfides dissolve in the electrolyte and diffuse out of the cathode.<sup>9</sup> Besides a permanent loss of active materials in the cathode, the dissolved  $\text{Li}_2\text{S}_x$  species participate in a parasitic shuttle between electrodes, resulting in capacity fade and self-discharge.<sup>11</sup> The reaction between polysulfides and active materials in the anode results in the formation of an insulating layer that increases cell resistance and compromises cycle life.<sup>33</sup> It is thus important to quantify diffusion and migration of lithium polysulfides in lithium battery electrolytes.

---

<sup>†</sup> This work was reported in *Macromolecules* **48**, 4863-4873 (2015)

Recent work has focused on designing nanostructured cathodes that confine sulfur and polysulfides within the cathode without impeding transport of lithium ions and electrons that are necessary for the redox reactions.<sup>12–15,34</sup> While these efforts have improved the cycle life of lithium-sulfur batteries, the diffusion of polysulfides out of the cathode has not been completely eliminated. It is conceivable that nanostructuring the electrolyte may be another approach for controlling the diffusion of polysulfides.

The theoretical specific energy of a battery with a sulfur cathode and a graphite anode is only 576 Wh/kg, a factor of four lower than that of a lithium-sulfur battery.<sup>35</sup> It is thus essential to have an electrolyte that is stable against lithium metal, as the lithium metal anode will be a necessary component of high specific energy batteries with sulfur cathodes. Dendrite formation on the lithium anode is a prominent failure mode in these batteries.<sup>36–38</sup> Previous work has shown that nanostructured block copolymer electrolytes, mixtures of polystyrene-*b*-poly(ethylene oxide) (SEO) and lithium bis(trifluoromethanesulfonyl)imide (LiTFSI), slow down the dendrite growth in lithium metal batteries.<sup>39–45</sup> This approach was motivated by theoretical calculations by Monroe and Newman, who predicted that electrolytes with high shear moduli were needed to stabilize lithium metal anodes.<sup>46</sup> The glassy polystyrene microphases endow SEO electrolytes with high moduli while the poly(ethylene oxide) (PEO) microphases provide channels for ion transport.<sup>39–45</sup> Understanding the electrochemical properties of SEO electrolytes containing lithium polysulfides is essential for evaluating their potential use in lithium-sulfur batteries.

Since polysulfides are ionic in nature, they may also migrate under the influence of electric fields. The importance of polysulfide migration can only be assessed after measuring transport properties such as conductivity, transference number, etc.<sup>47</sup> A significant problem in obtaining such data is that lithium polysulfides cannot be isolated.<sup>48</sup> Thus, making mixtures of solvents and polysulfides is non-trivial. Furthermore, polysulfides can undergo numerous spontaneous reactions: e.g. disproportionation reactions such as  $2S_x^{2-} \rightleftharpoons S_{x+m}^{2-} + S_{x-m}^{2-}$ .<sup>23,49</sup> In a study of polysulfide species dissolved in PEO and SEO, Wujcik et al. showed that at a particular sulfur concentration (0.44 g S/g PEO) only  $Li_2S_4$  and  $Li_2S_8$  exist as pure species. In contrast,  $Li_2S_2$  undergoes a disproportionation reaction to form  $Li_2S$  and  $Li_2S_4$ . Similarly,  $Li_2S_6$  undergoes a disproportionation reaction to form  $Li_2S_4$  and  $Li_2S_8$ .<sup>50</sup> Interpreting conductivity measurements of SEO/ $Li_2S_2$  and SEO/ $Li_2S_6$  systems would be complicated due to the presence of more than one polysulfide anion species. Therefore, in this study we focus on SEO mixed with  $Li_2S_4$  and  $Li_2S_8$ . Conductivity of these mixtures is compared with that of PEO/ $Li_2S_4$  and PEO/ $Li_2S_8$  mixtures to quantify the effect of nanostructuring on ion transport. In a practical lithium-sulfur battery, one would like to choose an electrolyte wherein the ion transport of the salt, such as LiTFSI, used in the electrolyte is much more rapid than that of the polysulfides. We therefore compare the conductivity of SEO/polysulfide and PEO/polysulfide mixtures with that of SEO/LiTFSI and PEO/LiTFSI. For simplicity, we refer to both  $Li_2S_x$  and LiTFSI as salts.

To our knowledge, there are limited published reports on the conductivity of polysulfide/solvent mixtures; Chang et al. reported the conductivity of  $Li_2S_8$  in tetraglyme,<sup>51</sup> and

Agostini et al. reported the conductivity of a ball milled mixture of Li<sub>2</sub>S<sub>8</sub> in a PEO based electrolyte containing additional salt.<sup>52</sup>

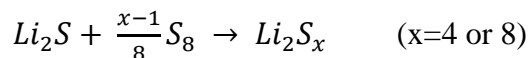
## 2.2 Experimental Section

### 2.2.1 Materials

PEO homopolymer with a number-averaged molecular weight,  $M_n$ , of 100 kg/mol was obtained from Sigma-Aldrich. The polymer was purified by dissolution in dichloromethane and subsequent precipitation in hexane. The purification process was repeated three times. The polymer was then dried in a vacuum oven at 90 °C for 24 hours. The SEO block copolymer was synthesized on a high vacuum line via sequential anionic polymerization.<sup>52</sup> The number averaged molecular weights of the polystyrene (PS) and PEO blocks were 47 kg/mol and 45 kg/mol, respectively. Both PEO and SEO were dried under vacuum at 90 °C for 24 hours in the antechamber of an argon (Ar) glove box and then taken into the glove box. Sulfur (S<sub>8</sub>) and lithium sulfide (Li<sub>2</sub>S) were received under Ar from Alfa Aesar, opened in an Ar-filled glove box, and used as received.<sup>50</sup> LiTFSI salt was received in an air-free package from Novolyte, transferred into a vial inside of the Ar glovebox, and then dried at 120 °C under vacuum for 3 days before using.<sup>53</sup>

### 2.2.2 Sample Preparation

Five types of samples were made for this study: PEO/Li<sub>2</sub>S<sub>8</sub>, PEO/Li<sub>2</sub>S<sub>4</sub>, SEO/Li<sub>2</sub>S<sub>8</sub>, SEO/Li<sub>2</sub>S<sub>4</sub>, and SEO/LiTFSI, following procedures established in previous works.<sup>50,53</sup> The polysulfide samples were made by dissolving the polymer of interest in dimethylformamide (DMF) by mixing at 90 °C on a heating plate for 5 hours. Separately, an Li<sub>2</sub>S<sub>x</sub> solution was made by mixing Li<sub>2</sub>S and S<sub>8</sub> in DMF at 90 °C for 5 hours in a sealed vial. The Li<sub>2</sub>S to S<sub>8</sub> ratio was determined by the stoichiometric reaction:



The Li<sub>2</sub>S<sub>x</sub>/DMF solution and the polymer/DMF solution were then mixed together at 90 °C for 24 hours in a sealed vial. The polymer/Li<sub>2</sub>S<sub>x</sub> samples were obtained by drying the mixed solutions in a Teflon petri-dish at 75 °C under Ar for 3 days, followed by drying at 50 °C under vacuum for 15 hours. Removal of the solvent and retention of the polysulfides in the samples were confirmed using elemental analysis to determine the relative ratios of C, H, N and S at the Microanalytical Laboratory in the College of Chemistry, University of California, Berkeley.

SEO/LiTFSI samples were prepared by dissolving the components separately in DMF and mixing the two solutions at 90 °C for 24 hours. The mixed solutions were dried at 90 °C in an Ar environment for 24 hours, and then dried at 90 °C under vacuum in the glove box antechamber for 24 hours to get the sample.

In our previous studies, the concentration of lithium salts in PEO-containing polymers is defined as the molar ratio of lithium atoms to ethylene oxide moieties,  $r = [\text{Li}^+]/[\text{EO}]$ . Whether or not the same definition should be used to describe PEO/Li<sub>2</sub>S<sub>x</sub> and SEO/Li<sub>2</sub>S<sub>x</sub> mixtures is an interesting open question. In most publications, lithium polysulfides are depicted as linear chains with charged sulfur and lithium ions at the chain ends.<sup>54-56</sup> Such depictions suggest that both lithium ions might, in principle, dissociate from the polysulfide chains. Simulations of polysulfides in PEO by Pascal et al. show a different molecular configuration, as shown in Figure 2.1. The S<sub>4</sub><sup>2-</sup> and S<sub>8</sub><sup>2-</sup> chains form a claw-like structure, with one Li<sup>+</sup> localized within the claw and the other outside of the claw.<sup>1</sup> It is thus likely that Li<sub>2</sub>S<sub>x</sub> molecules dissociate into LiS<sub>x</sub><sup>-</sup> and Li<sup>+</sup>. In this paper, we thus define our salt concentration,  $R$ , as

$$R = \frac{[\text{Li}^+]}{|z^-|[\text{EO}]} \quad (1)$$

where  $|z^-|$  is the magnitude of the charge of the anion. For Li<sub>2</sub>S<sub>x</sub>,  $|z^-| = 2$ , and for LiTFSI,  $|z^-| = 1$ . Given our current understanding, it is best, in our opinion, to compare polymer/Li<sub>2</sub>S<sub>x</sub> and polymer/LiTFSI mixtures with the same value of  $R$ .

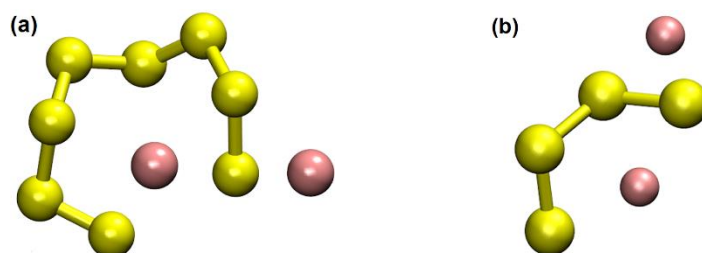


Figure 2.1 Typical simulation results of (a) Li<sub>2</sub>S<sub>8</sub> and (b) Li<sub>2</sub>S<sub>4</sub> configurations in a matrix of short PEO chains (matrix not shown for simplicity) taken from reference 36.

### 2.2.3 Small-Angle X-ray Scattering (SAXS)

The morphology of the polymer/Li<sub>2</sub>S<sub>x</sub> samples were determined by SAXS. Each sample was pressed into a 1 mm thick fiberglass reinforced silicone spacer with a diameter of 3.18 mm inside an Ar glove box. Both ends of the spacer were sealed with Kapton windows in a custom-designed airtight sample holder. All samples were annealed at 120 °C under Ar for 24 hours to eliminate any strain induced during sample preparation.

SAXS measurements were performed at beamline 7.3.3 at the Advanced Light Source (ALS) at Lawrence Berkeley National Laboratory using 10 keV monochromatic X-rays.<sup>57</sup> Samples were mounted in a custom-built heating stage, and the sample-to-detector distance and beam center were calibrated using a silver behenate standard. The samples were heated from 30 °C to 120 °C and cooled 60 °C, with increments of 30 °C during heating and increments of 10 °C during cooling, before being cooled back to room temperature. The samples were held at each temperature for 30-60 min before taking the measurements. All images were obtained using 2 s exposures. The Nika



macro for Igor Pro developed by Jan Ilavsky was used to reduce the two dimensional SAXS patterns,<sup>58</sup> and the azimuthally averaged intensity,  $I$ , was plotted against the magnitude of the scattering vector,  $q = 4\pi \sin\left(\frac{\theta}{2}\right)/\lambda$ , where  $\theta$  was the scattering angle and  $\lambda$  was the wavelength of the X-ray. Each scattering data was further processed by subtracting the background scattering from the blank, an empty sample cell, using equation (2).

$$I = I_{\text{Sample}} - \frac{T_{\text{Sample}}}{T_{\text{Blank}}} \times I_{\text{Blank}} \quad (2)$$

where  $I_{\text{Sample}}$  and  $I_{\text{Blank}}$  are the raw scattering intensities from the sample and the empty cell respectively, and  $T_{\text{Sample}}$  and  $T_{\text{Blank}}$  are transmission coefficients of the sample and the blank respectively.

#### 2.2.4 Differential Scanning Calorimetry (DSC)

PEO/Li<sub>2</sub>S<sub>x</sub> and SEO/Li<sub>2</sub>S<sub>x</sub> samples were sealed in hermetic aluminum pans in an Ar glove box for DSC experiments, which were performed on a Thermal Advantage 2920 instrument. All samples were heated to 150 °C at a rate of 10 °C/min, cooled to -70 °C at a rate of 5 °C/min, and heated again to 150 °C at a rate of 10 °C/min. Data from the second heating are presented in this paper.

#### 2.2.5 AC Impedance Spectroscopy

The ionic conductivity of each sample was measured by ac impedance spectroscopy. Each sample was mechanically pressed into a 0.125 mm thick epoxy fiberglass, Garolite-10 spacer with a diameter of 4.76 mm. Two high purity, 18 μm thick Aluminum electrode foils were pressed on each side of the polymer contained spacer. The area of the sample was determined by the size of the hole in the spacer, and the thickness of the sample was measured with a micrometer. Two aluminum tabs were attached to each of the electrode foils to make electrical contacts. The samples were then placed in a laminated aluminum pouching material and sealed under vacuum before removing them from the glove box.

A Biologic VMP3 potentiostat was used to measure the real and imaginary impedances,  $Z'$  and  $Z''$ , of the samples using an ac signal with 80 mV amplitude and frequencies varying from 1 Hz to 1 MHz. The impedance spectrum was interpreted by an equivalent circuit shown in Figure 2.2a. The equivalent circuit is composed of  $R_2$ , the electrolyte resistance, in series with  $Q_2$ , the blocking electrode/electrolyte interfaces pseudo-capacitance, together in parallel with  $C_1$ , the geometrical capacitance due to the a finite dielectric constant of the electrolyte between the two parallel metallic electrodes, and together in series with the apparatus resistance,  $R_1$ , and the inductance,  $L_1$ .<sup>59,60</sup> The impedance locus simulated by using this equivalent circuit is used to determine  $R_2$ , the resistance due to ion transport in the electrolyte.

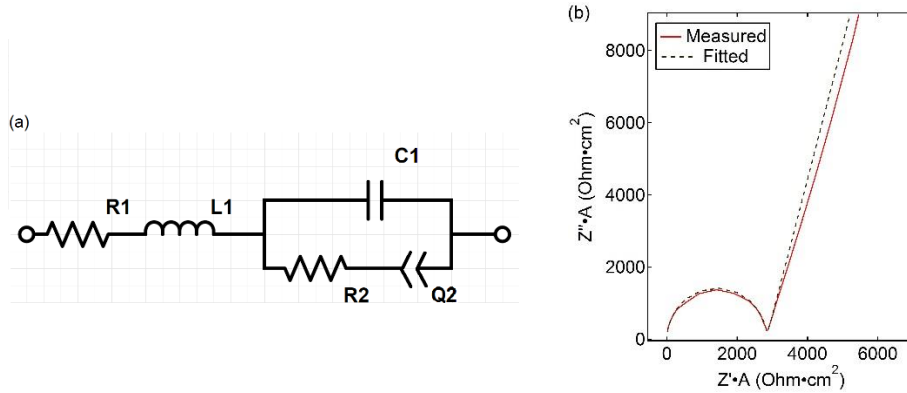


Figure 2.2 (a) Equivalent circuit for determining the ionic resistance of the polymer/salt electrolytes with blocking electrodes. (b) Typical experimental data plotted in the Nyquist format of SEO/Li<sub>2</sub>S<sub>4</sub> at 70 °C ( $R = 0.025$ ). The simulated impedance diagram is indicated by a dashed line

The conductivity of the electrolyte is determined by equation (3),

$$\sigma = \frac{l}{R_2 A} \quad (3)$$

where  $l$  is the sample thickness, which is re-measured after the measurements, and  $A$  is the area. The conductivity of salt-containing samples is reported after subtracting the measured conductivities of pure PEO and SEO. Values for conductivities of pure polymers range between  $1.91 \times 10^{-7}$  S/cm and  $5.33 \times 10^{-7}$  S/cm. Three independent replicates at each salt concentration were used to determine the conductivity of SEO/Li<sub>2</sub>S<sub>x</sub> and PEO/Li<sub>2</sub>S<sub>x</sub> samples. Only one sample at a given salt concentration was used to determine the conductivity of SEO/LiTFSI samples.

## 2.2.6 X-ray Absorption Spectroscopy (XAS)

Thin film samples for concentration-dependent XAS experiments were prepared by spin coating solutions of PEO containing Li<sub>2</sub>S<sub>8</sub> and Li<sub>2</sub>S<sub>4</sub> in DMF as described in our previous study<sup>29</sup>. The samples for each ‘x’ value were prepared from one single bulk solution (e.g. Li<sub>2</sub>S<sub>8</sub> at a concentration of 0.2 g S/ g PEO was prepared from the same Li<sub>2</sub>S<sub>8</sub>/DMF solution as the 0.5 g S/g PEO). The range of  $R$  values covered are 0.034 to 0.086 for Li<sub>2</sub>S<sub>8</sub> and 0.069 to 0.172 for Li<sub>2</sub>S<sub>4</sub>. This means that the observed spectra only reflect the different salt concentrations and not small differences in ‘x’ values. The experimental Li<sub>2</sub>S<sub>x</sub> ‘x’ values were 7.97 and 4.01 for the Li<sub>2</sub>S<sub>8</sub> and Li<sub>2</sub>S<sub>4</sub> solutions, respectively. The PEO used to make the thin film samples had a molecular weight of 55 kg/mol (Polymer Source Inc.). Samples were spin coated at 2000 RPM for 60 seconds, at room temperature, with 30  $\mu$ L of solution.

Thin film samples are not appropriate for temperature studies due to the potential of sulfur loss during measurements. We thus conduct these measurements on liquid samples. Polysulfide solutions were prepared by mixing Li<sub>2</sub>S and S<sub>8</sub> in PEO at 90 °C for three days. The molecular

weight of the PEO was 600 g/mol, and was obtained from Polymer Source Inc. The experimental  $\text{Li}_2\text{S}_x$  'x' value for the  $\text{Li}_2\text{S}_8$  solution was 7.97, and that of the  $\text{Li}_2\text{S}_4$  solution was 4.00. The concentration of polysulfide species in the  $\text{Li}_2\text{S}_8$  sample corresponded to  $R = 0.005$  and the concentration of the  $\text{Li}_2\text{S}_4$  sample corresponded to  $R = 0.015$ . These low salt concentrations were used to avoid X-ray overabsorption. After three days of mixing, solutions were brought to the Stanford Synchrotron Radiation Lightsource (SSRL) and placed in an Ar glovebox. Prior to measurement, approximately 0.3 mL of each solution was loaded into an air-tight, custom made liquid cell containing a 3 $\mu\text{m}$  thin film of Mylar that served as an X-ray transparent window.

Unfortunately, due to instrumental limitations, the concentration and temperature range over which XAS experiments were performed are different from those used in our morphology and conductivity studies. Entirely different XAS setups would be needed to cover the concentrations used in our morphology and conductivity studies.

XAS experiments were performed at beamline 4-3 at SSRL. Samples were measured in fluorescence mode using a 4-element silicon Vortex detector. The beamline energy was calibrated using sodium thiosulfate, setting the first centroid peak to 2472.02 eV. Spectra were taken over the range of 2440 to 2575 eV with an energy resolution as low as 0.08 eV near the absorption edge. Three consecutive scans were taken for each sample, and at each temperature, without any movement of the sample stage between scans and then averaged for further data analysis. Samples were allowed to rest for 20 minutes after each change in temperature to allow for full equilibration. X-ray spectra were normalized and background subtracted using SIXPACK.

## 2.3 RESULTS AND DISCUSSION

### 2.3.1 Morphology

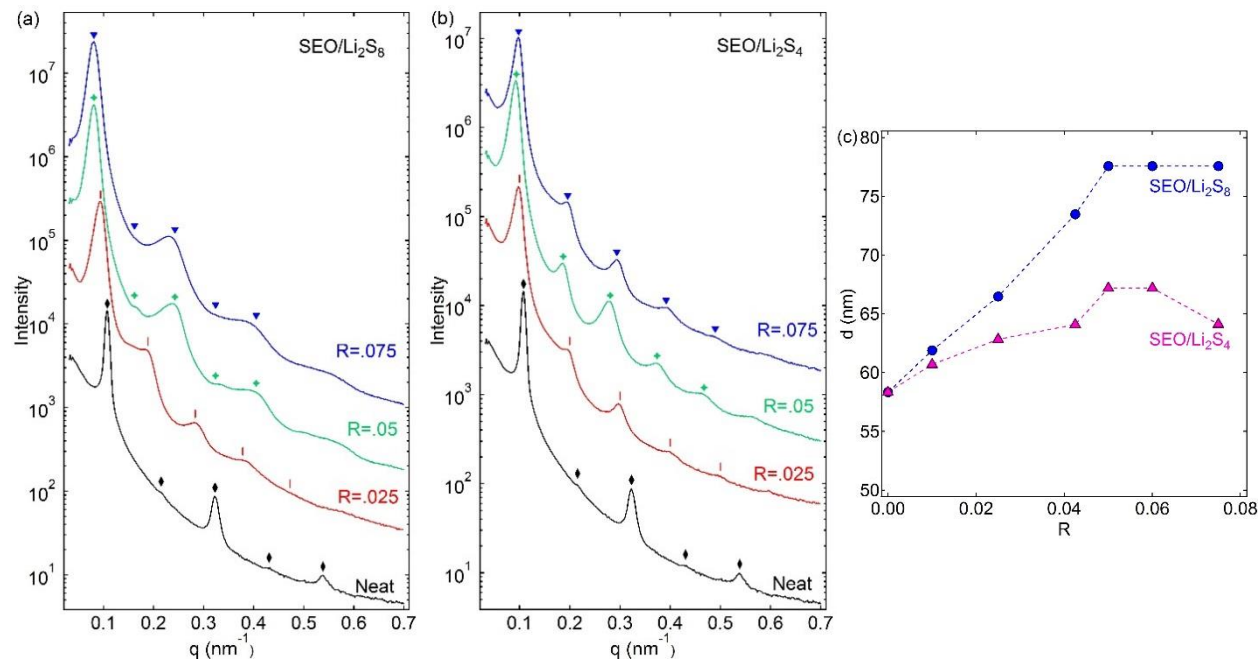


Figure 2.3 SAXS intensity versus magnitude of the scattering vector,  $q$ , for (a) SEO/Li<sub>2</sub>S<sub>8</sub> and (b) SEO/Li<sub>2</sub>S<sub>4</sub> at 90 °C. Profiles are offset for clarity. Markers on top of each profile indicate the expected locations for  $q^*$ ,  $2q^*$ ,  $3q^*$ ,  $4q^*$  and  $5q^*$ . (c) Lamellar domain spacing,  $d$ , versus the Li<sub>2</sub>S<sub>x</sub> concentration,  $R$ .

We first examine the morphology of SEO/Li<sub>2</sub>S<sub>x</sub> mixtures. Figures 2.3a and 2.3b show selected SAXS profiles of the block copolymer with Li<sub>2</sub>S<sub>8</sub> and Li<sub>2</sub>S<sub>4</sub>, respectively, over a range of salt concentrations,  $R = 0 - 0.075$ . All of the SAXS profiles in Figure 2.3 are consistent with a lamellar morphology. The center-to-center distance between adjacent PS lamellae,  $d$ , is given by  $2\pi/q^*$ , where  $q^*$  is the value of  $q$  at the primary peak. Higher order peaks at  $2q^*$ ,  $3q^*$ ,  $4q^*$  and  $5q^*$  are evident in most samples. The even order peaks are absent in the  $R = 0$  sample due to the minima in the form factor of lamellae. The dependence of  $d$  on  $R$  is shown in Figure 2.3c. For SEO/Li<sub>2</sub>S<sub>8</sub> samples,  $d$  increases more-or-less linearly with  $R$  for values less than 0.05 from 58 nm to 78 nm, approaching a plateau for higher values of  $R$ . In contrast, for SEO/Li<sub>2</sub>S<sub>4</sub> samples,  $d$  is a non-monotonic function of  $R$ , with a shallow maximum at  $R$  between 0.05 and 0.06, as shown in Figure 2.3c. We are not sure of the reason for the slight decrease in  $d$  with increasing  $R$  at  $R > 0.06$ . The domain spacing at fixed  $R$  is higher for SEO/Li<sub>2</sub>S<sub>8</sub> samples compared to SEO/Li<sub>2</sub>S<sub>4</sub> samples. The SAXS profiles of SEO/Li<sub>2</sub>S<sub>x</sub> mixtures were insensitive to changes in temperature; the maximum change in  $d$  over the temperature range from 60 to 120 °C was 1.6%.

### 2.3.2 Thermal Properties

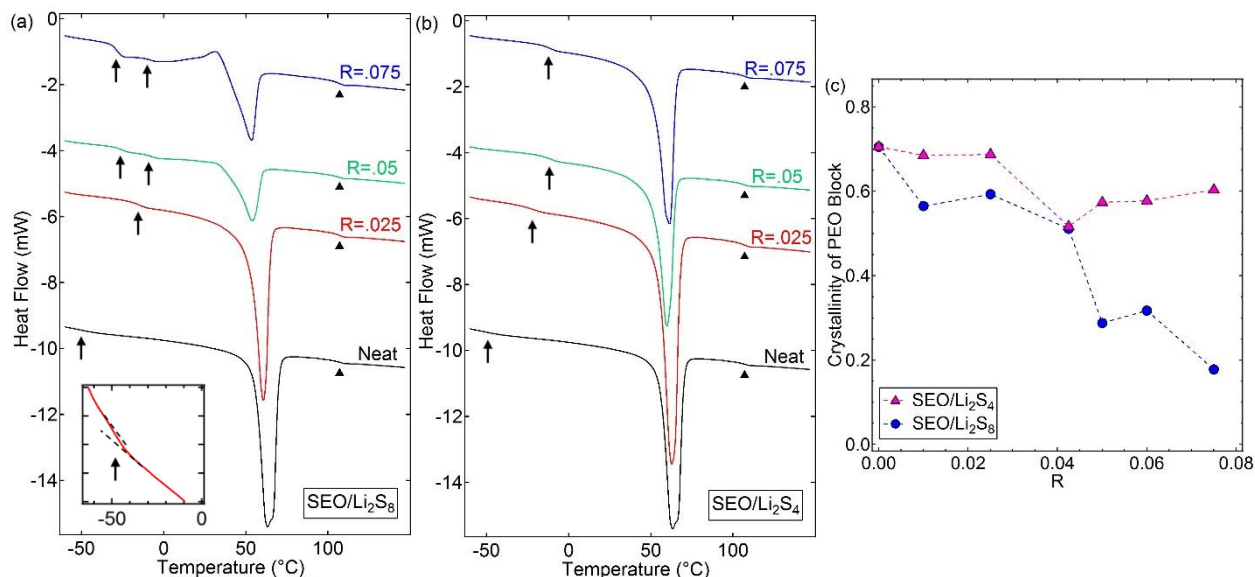


Figure 2.4. DSC scans of (a) SEO/Li<sub>2</sub>S<sub>8</sub> and (b) SEO/Li<sub>2</sub>S<sub>4</sub>. Scans are offset for clarity. Inset in (a) shows the DSC scan of neat PEO on an expanded scale. Arrows show  $T_g^{\text{PEO}}$  and triangles show  $T_g^{\text{PS}}$ . (c) Effect of salt concentration,  $R$ , on the crystallinity of the PEO microphase for SEO/Li<sub>2</sub>S<sub>x</sub> samples.

Figures 2.4a and 2.4b show DSC scans for selected concentrations of SEO/Li<sub>2</sub>S<sub>8</sub> and SEO/Li<sub>2</sub>S<sub>4</sub>, respectively. The enthalpy of melting of the PEO crystals in our samples,  $\Delta H_m$ , is related to the area under the melting peak seen in Figure 2.4.  $\Delta H_m$  generally decreases with increasing salt concentration in both samples. As  $R$  increases from 0 to 0.075,  $\Delta H_m$  decreases from 64 to 14 J/g in SEO/Li<sub>2</sub>S<sub>8</sub>, and from 64 to 46 J/g in SEO/Li<sub>2</sub>S<sub>4</sub>. The degree of crystallinity was calculated according to equation (4),

$$\text{Crystallinity} = \frac{\Delta H_m}{\omega_{\text{EO}} \Delta H_m^0} \quad (4)$$

where  $\omega_{\text{EO}}$  is the weight fraction of ethylene oxide (EO) in each sample,  $\Delta H_m$  is the melting enthalpy of the sample, which is evaluated by integrating the area under the melting endothermic peak in the second heating scan, and  $\Delta H_m^0$  is the melting enthalpy of 100% crystalline PEO. Literature value for  $\Delta H_m^0$  ranges from 134 to 214 J/g.<sup>61–67</sup> Here, for concreteness, we use a value of 186 J/g for  $\Delta H_m^0$ . The effect of Li<sub>2</sub>S<sub>8</sub> and Li<sub>2</sub>S<sub>4</sub> concentrations on the crystallinity of the PEO/Li<sub>2</sub>S<sub>x</sub> microphase in SEO/Li<sub>2</sub>S<sub>x</sub> samples is shown in Figure 2.4c. The polarity of ether oxygen atoms on PEO backbones and the suitable distance between them enables coordination of lithium ions,<sup>68</sup> causing lithium salts to segregate into PEO microphases. This suppresses crystallization of PEO chains, and crystallinity generally decreases with increasing salt concentrations in both SEO/Li<sub>2</sub>S<sub>8</sub> and SEO/Li<sub>2</sub>S<sub>4</sub> samples. The suppression of crystallinity in SEO/Li<sub>2</sub>S<sub>4</sub> samples is less significant than that in the SEO/Li<sub>2</sub>S<sub>8</sub> samples, indicating that PEO/Li<sub>2</sub>S<sub>8</sub> interactions are more favorable than PEO/Li<sub>2</sub>S<sub>4</sub> interactions.

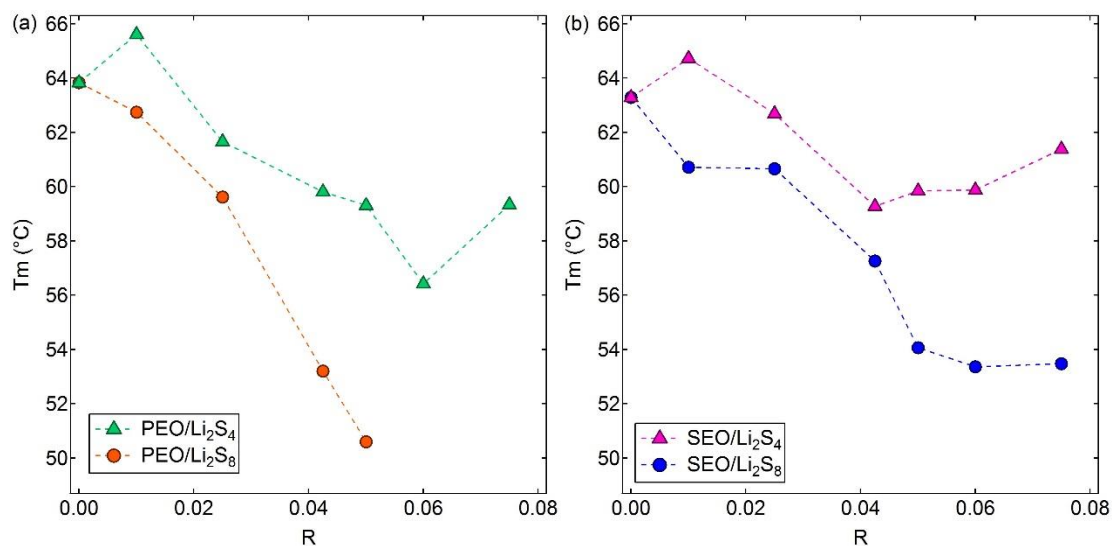


Figure 2.5. Melting temperature of PEO,  $T_m$ , versus salt concentration,  $R$ , for (a) PEO/Li<sub>2</sub>S<sub>x</sub> samples and (b) SEO/Li<sub>2</sub>S<sub>x</sub> samples.

Figure 2.5a plots the measured melting temperature of crystalline PEO,  $T_m$ , of PEO/Li<sub>2</sub>S<sub>8</sub> and PEO/Li<sub>2</sub>S<sub>4</sub> samples obtained from the DSC scans shown in Figure S2.1 in the supporting information. In the PEO/Li<sub>2</sub>S<sub>8</sub> samples,  $T_m$  decreases monotonically from 64 to 51 °C as  $R$  increases from 0 to 0.05. We do not see a melting peak for  $R > 0.05$ , indicating that the crystallinity of PEO is completely suppressed in high Li<sub>2</sub>S<sub>8</sub> concentration samples. In the range  $R = 0 - 0.075$ ,  $T_m$  of PEO/Li<sub>2</sub>S<sub>4</sub> samples range from 56 to 66 °C. Figure 2.5b shows  $T_m$  of SEO/Li<sub>2</sub>S<sub>8</sub> and SEO/Li<sub>2</sub>S<sub>4</sub> samples obtained from the DSC scans shown in Figure 2.4. In the SEO/Li<sub>2</sub>S<sub>8</sub> samples,  $T_m$  monotonically decreases from 63 to 54 °C as  $R$  increases from 0 to 0.05, and reaches a plateau for  $R > 0.05$ . In the range  $R = 0 - 0.075$ ,  $T_m$  of SEO/Li<sub>2</sub>S<sub>4</sub> samples range from 65 to 59 °C. Reproducibility of measured  $T_m$  values is about 1 °C. It is clear that  $T_m$  is a weak function of salt concentration in both PEO/Li<sub>2</sub>S<sub>4</sub> and SEO/Li<sub>2</sub>S<sub>4</sub> samples. The  $T_m$  values of both PEO/Li<sub>2</sub>S<sub>4</sub> and SEO/Li<sub>2</sub>S<sub>4</sub> samples with  $R = 0.01$  are slightly higher than those of the neat polymers. We do not know the reason for this observation.

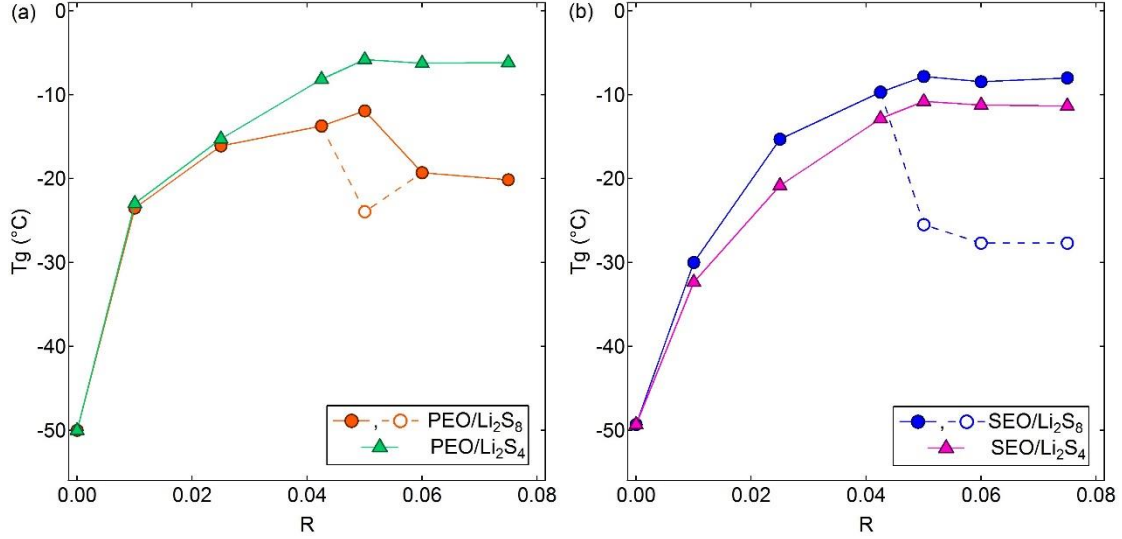


Figure 2.6. Glass transition temperature of PEO,  $T_g^{\text{PEO}}$ , versus salt concentration,  $R$ , for (a) PEO/Li<sub>2</sub>S<sub>x</sub> samples and (b) SEO/Li<sub>2</sub>S<sub>x</sub> samples.

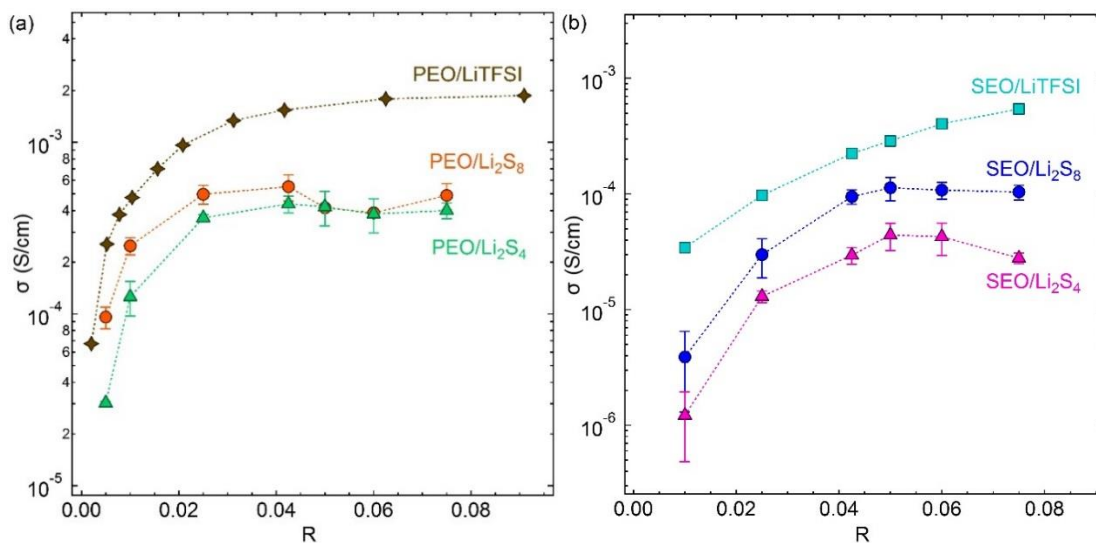
The DSC scans of SEO/Li<sub>2</sub>S<sub>8</sub> and SEO/Li<sub>2</sub>S<sub>4</sub> show glass transition temperatures below 0 °C and above 100 °C. The former corresponds to the glass transition of the PEO-rich microphase while the latter corresponds to the glass transition of the PS-rich microphase. The DSC scans of PEO/Li<sub>2</sub>S<sub>8</sub> and PEO/Li<sub>2</sub>S<sub>4</sub>, shown in Figure S2.1 of the supporting information, only show glass transitions below 0 °C. Figure 2.6a plots the measured glass transition temperature,  $T_g^{\text{PEO}}$ , of PEO/Li<sub>2</sub>S<sub>8</sub> and PEO/Li<sub>2</sub>S<sub>4</sub> samples. In the low salt concentration limit PEO/Li<sub>2</sub>S<sub>8</sub> samples exhibit a single glass transition;  $T_g^{\text{PEO}}$  increases from -50 to -14 °C as  $R$  increases from 0 to 0.0425. At  $R = 0.05$ , two glass transitions are observed. This can be seen if one carefully examines the DSC scan in Figure S2.1a. To clarify this phenomenon, expanded views of the DSC scans at  $R = 0.0425$  and 0.05 are shown in Figure S2.2 in the supporting information. A single glass transition is clearly obtained at  $R = 0.0425$  while two glass transitions at -24 and -12 °C are obtained at  $R = 0.05$ . A single  $T_g^{\text{PEO}}$  is recovered upon increasing  $R$  to 0.06 and beyond as shown in Figure 2.6a. All PEO/Li<sub>2</sub>S<sub>4</sub> samples exhibit a single  $T_g$  which increases from -50 to -6 °C as  $R$  increases from 0 to 0.05, and reaches a plateau for  $R > 0.05$ . Figure 2.6b shows  $T_g^{\text{PEO}}$  of SEO/Li<sub>2</sub>S<sub>8</sub> and SEO/Li<sub>2</sub>S<sub>4</sub> samples obtained from the DSC scans shown in Figure 2.4. In the SEO/Li<sub>2</sub>S<sub>8</sub> samples,  $T_g^{\text{PEO}}$  increases from -49 to -10 °C as  $R$  increases from 0 to 0.0425. For  $R \geq 0.05$ , two  $T_g^{\text{PEO}}$  values are observed, a higher  $T_g^{\text{PEO}}$  value at  $-8.1 \pm 0.4$  °C and a lower  $T_g^{\text{PEO}}$  value at  $-26.1 \pm 1.6$  °C. The dependence of  $T_g^{\text{PEO}}$  on  $R$  in the SEO/Li<sub>2</sub>S<sub>4</sub> samples is similar to that in the PEO/Li<sub>2</sub>S<sub>4</sub> samples;  $T_g^{\text{PEO}}$  increases from -49 to -11 °C as  $R$  increases from 0 to 0.05, and reaches a plateau for  $R > 0.05$ .

The presence of two glass transitions in both PEO/Li<sub>2</sub>S<sub>8</sub> and SEO/Li<sub>2</sub>S<sub>8</sub> samples appears to be related to both salt concentration and crystallinity. In dilute samples with  $R \leq 0.0425$ , a single  $T_g^{\text{PEO}}$  is obtained in both systems (Figure 2.6). Increasing  $R$  to 0.05 results in two glass transitions in PEO/Li<sub>2</sub>S<sub>8</sub> and SEO/Li<sub>2</sub>S<sub>8</sub>. These samples are semi-crystalline in the vicinity of their glass

transition temperatures. It is reasonable to assume that salt molecules are localized in the amorphous portions of PEO. We propose that two glass transitions reflect two different amorphous regions, one with high salt concentration and the other with low salt concentration. The heterogeneity in salt distribution disappears when crystallinity is lost as is the case in PEO/Li<sub>2</sub>S<sub>8</sub> at  $R = 0.06$  and beyond. Further work is needed to determine the underpinnings of the observed behavior of glassy and semi-crystalline PEO-rich microphases containing Li<sub>2</sub>S<sub>x</sub>. The main focus of this work is to quantify ion transport at temperatures above the melting temperature of PEO. Our limited understanding of salt distribution in crystalline samples does not affect interpretation of ion transport data given below.

The glass transition temperature of the PS microphase,  $T_g^{\text{PS}}$ , in the SEO/Li<sub>2</sub>S<sub>x</sub> samples at all salt concentrations are at  $107 \pm 1$  °C. The insensitivity of  $T_g^{\text{PS}}$  of PS microphase with salt concentration indicates that Li<sub>2</sub>S<sub>x</sub> molecules do not interact with PS.

### 2.3.3 Electrochemical Properties





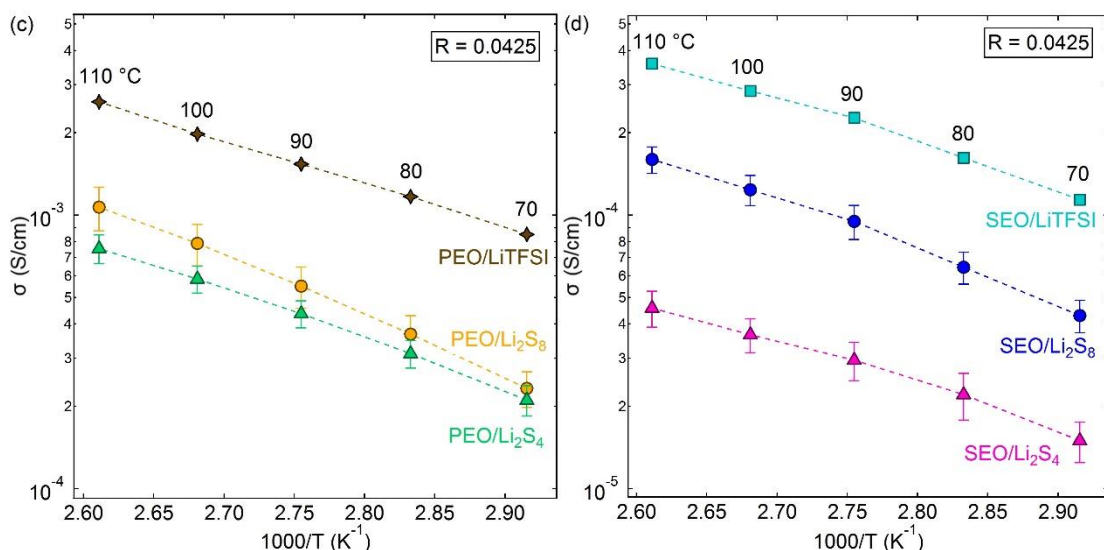


Figure 2.7. Conductivity,  $\sigma$ , versus salt concentration,  $R$ , for (a) PEO/salt samples, and (b) SEO/salt samples at 90 °C. Conductivity,  $\sigma$ , versus inverse temperature,  $1000/T$ , for (c) PEO/salt samples, and (d) SEO/salt samples at  $R = 0.0425$ .

Our electrochemical characterization experiments are limited to temperatures above the melting temperature of PEO. Figure 2.7a plots the measured conductivity of PEO/Li<sub>2</sub>S<sub>8</sub> and PEO/Li<sub>2</sub>S<sub>4</sub> samples at 90 °C. Also shown in Figure 2.7a is the conductivity of PEO/LiTFSI, taken from the work of Lascaud et al.<sup>69</sup> The conductivity of PEO/Li<sub>2</sub>S<sub>x</sub> increases rapidly at low  $R$  values, and reaches a plateau at  $R = 0.0425$ . The conductivity of PEO/Li<sub>2</sub>S<sub>8</sub> is higher than that of the PEO/Li<sub>2</sub>S<sub>4</sub> samples at  $R < 0.05$ , and becomes similar at  $R \geq 0.05$ . Within this concentration range, the conductivity of PEO/LiTFSI increases monotonically with salt concentration. (The conductivity of PEO/LiTFSI measured by Lascaud et al. peaks at  $R = 0.085$ , and decreases slowly until  $R = 0.5$ .) The conductivity of mixtures containing Li<sub>2</sub>S<sub>x</sub> are generally lower than that of mixtures containing LiTFSI. At high salt concentrations ( $R > 0.04$ ), the conductivity of Li<sub>2</sub>S<sub>x</sub> mixtures is about a factor of five lower than that of LiTFSI mixtures.

Figure 2.7b shows the conductivity of SEO/Li<sub>2</sub>S<sub>8</sub> and SEO/Li<sub>2</sub>S<sub>4</sub> samples. Also shown in Figure 2.7b is the conductivity of SEO/LiTFSI. The trends seen in Figure 2.5b can be anticipated from the PEO data in Figure 2.5a. The conductivity versus  $R$  curves of SEO/Li<sub>2</sub>S<sub>8</sub> and SEO/Li<sub>2</sub>S<sub>4</sub> are nearly parallel to each other; the conductivity of SEO/Li<sub>2</sub>S<sub>8</sub> is about a factor of two higher than that of SEO/Li<sub>2</sub>S<sub>4</sub> at all salt concentrations. The conductivity of SEO/LiTFSI is higher than that of both polysulfide mixtures at all concentrations. The conductivity of SEO/Li<sub>2</sub>S<sub>4</sub> mixtures at  $R > 0.05$  is a weak function of salt concentration. It is well-known that increasing the glass transition temperature lowers the conductivity of polymer electrolytes.<sup>40,48</sup> The glass transition temperature of our PEO/Li<sub>2</sub>S<sub>x</sub>, and that of the PEO microphase in SEO/Li<sub>2</sub>S<sub>x</sub>,  $T_g^{\text{PEO}}$ , increases with increasing  $R$  (Figure 2.6). The increase in conductivity with increasing  $R$  (Figures 2.7a and b) might have been larger if  $T_g^{\text{PEO}}$  were unaffected by  $R$ . Figure 2.7c and 2.7d show the conductivity of PEO/salt

and SEO/salt respectively at  $R = 0.0425$ . All conductivities increase with temperature.

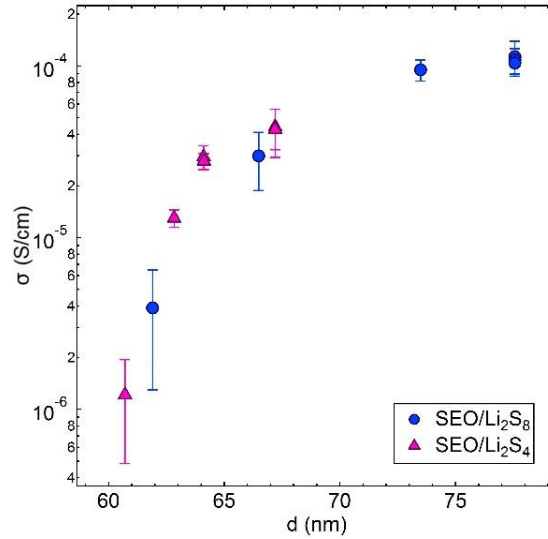


Figure 2.8. Conductivity,  $\sigma$ , versus domain spacing,  $d$ , for SEO/Li<sub>2</sub>S<sub>x</sub> samples at 90 °C.

In Figure 2.8, we plot  $\sigma$  as a function of  $d$  for SEO/Li<sub>2</sub>S<sub>8</sub> and SEO/Li<sub>2</sub>S<sub>4</sub> at 90 °C. Both sets of data appear to collapse onto a single curve, suggesting a relationship between transport and thermodynamics; the values of  $d$  reflect thermodynamic interactions between polysulfides and PEO chains.

The effect of morphology on conductivity of block copolymer/salt mixtures can be quantified by examining normalized conductivities. The normalized conductivity,  $\sigma_n$ , is defined by equation (5),

$$\sigma_n = \frac{\sigma_{\text{SEO/salt}}}{f \phi_{\text{EO/salt}} \sigma_{\text{PEO/salt}}} \quad (5)$$

where  $\sigma_{\text{SEO/salt}}$  and  $\sigma_{\text{PEO/salt}}$  are conductivities of the two systems at the same value of  $R$ ,  $\phi_{\text{EO/salt}}$  is the volume fraction of the PEO/salt microdomains, and  $f$  is the morphology factor that accounts for the geometry of the conducting microdomains. Since all of the SEO/salt mixtures have a lamellae morphology,  $f = 2/3$ .<sup>22</sup>

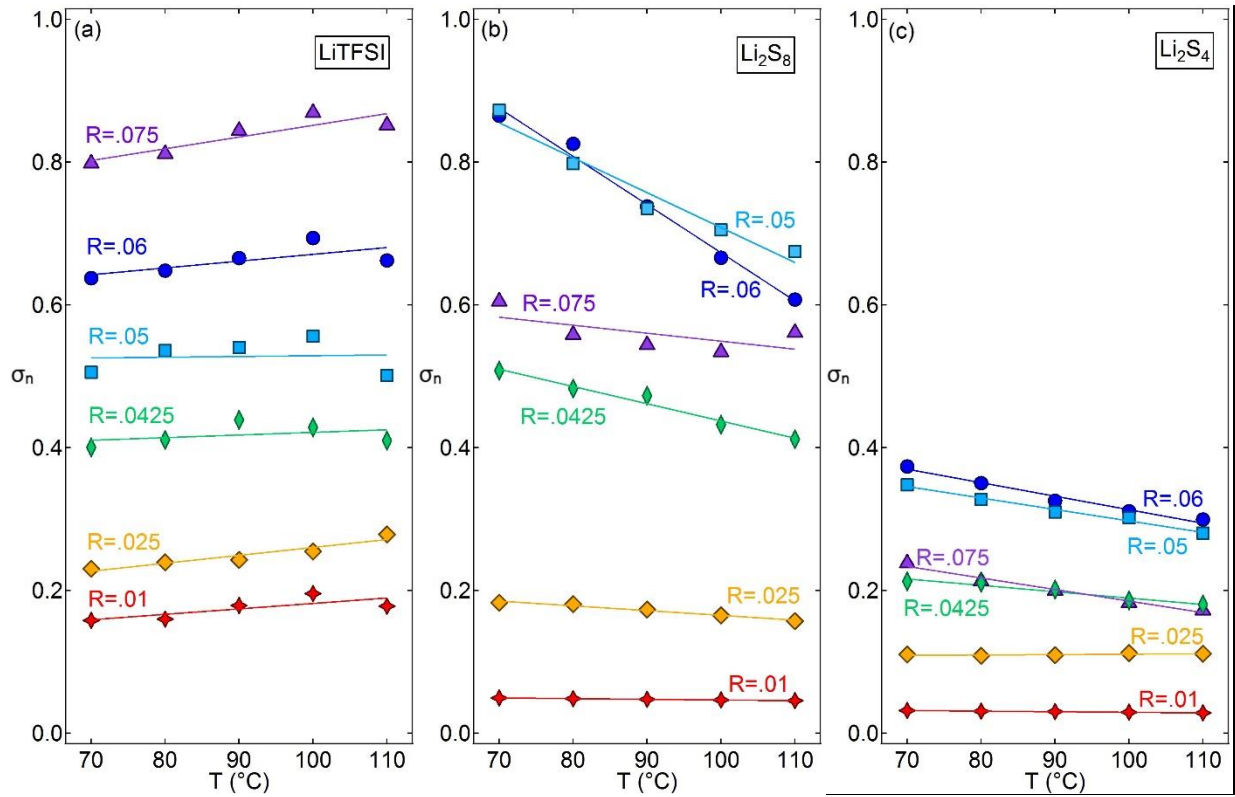


Figure 2.9. Normalized Conductivity,  $\sigma_n$ , of (a) SEO/LiTFSI, (b) SEO/ $\text{Li}_2\text{S}_8$ , and (c) SEO/ $\text{Li}_2\text{S}_4$  versus Temperature,  $T$ .

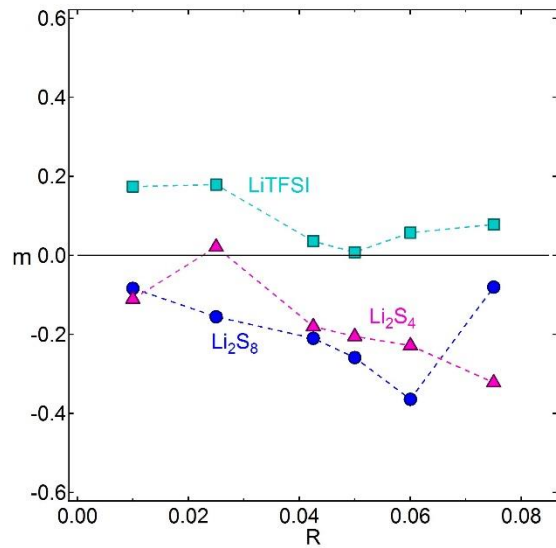


Figure 2.10. Plot of  $m$  versus salt concentration,  $R$ . The parameter  $m$  is a non-dimensional measure of the temperature dependence  $\sigma_n$  as defined in equation (6).

In Figure 2.9 we plot  $\sigma_n$  versus  $T$  of SEO/LiTFSI, SEO/ $\text{Li}_2\text{S}_8$ , and SEO/ $\text{Li}_2\text{S}_4$  samples in the

temperature range 70 to 110 °C. The normalized conductivity of SEO/LiTFSI increases with increasing temperature, while the normalized conductivities of SEO/Li<sub>2</sub>S<sub>8</sub> and SEO/Li<sub>2</sub>S<sub>4</sub> decrease with increasing temperature. The SEO/salt data indicates a slight suppression of migration of Li<sub>2</sub>S<sub>x</sub> species in SEO compared to PEO with increasing temperature. If the proposed normalization scheme accurately described transport of salt through block copolymers, then  $\sigma_n$  would be independent of temperature. The finite slopes of linear fits through the data in Figure 2.9 indicate limitations in the proposed normalization scheme. We quantify this by fitting the data in Figure 2.9 to the following linear equation,

$$\sigma_n = \sigma_n^\circ \left[ 1 + m \frac{(T-90)}{40} \right] \quad (6)$$

where  $\sigma_n^\circ$  is the fitted value of  $\sigma_n$  of each sample at a reference temperature of 90 °C ( $\sigma_n^\circ = a + 90b$ , where  $a$  and  $b$  are intercepts and the slope of the fitted line, respectively, as shown in Figure 2.9a-c). The parameter  $m$  signifies the relative change of  $\sigma_n$  in the temperature range of interest. The plot of  $m$  versus  $R$  in Figure 2.10 shows that the magnitude of  $m$  averages around 0.2. We do not know the reason for the observed slight suppression of polysulfide migration as a function of increasing temperature. In the discussion below, we present the temperature-averaged values of  $\sigma_n$ .

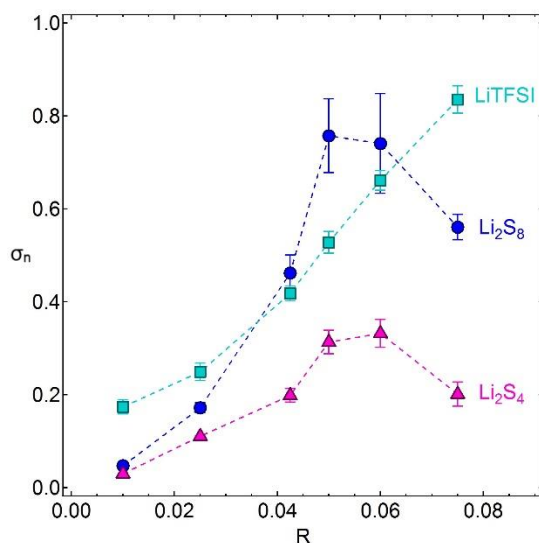


Figure 2.11. Temperature-averaged normalized conductivity,  $\sigma_n$ , versus salt concentration,  $R$ . The error bars represent the standard deviation of  $\sigma_n$ .

Figure 2.11 shows the temperature-averaged normalized conductivities,  $\sigma_n$ , for all three salts. The  $\sigma_n$  for LiTFSI samples increases monotonically over the measured concentration range, while the  $\sigma_n$  for both Li<sub>2</sub>S<sub>8</sub> and Li<sub>2</sub>S<sub>4</sub> samples increases initially with salt concentration, peaks between  $R = 0.05$  and  $R = 0.06$ , and decreases at higher concentrations. The  $\sigma_n$  for Li<sub>2</sub>S<sub>4</sub> is lower than that of Li<sub>2</sub>S<sub>8</sub> at all salt concentrations, indicating that SEO hinders the migration of Li<sub>2</sub>S<sub>4</sub> more significantly than it hinders the migration of Li<sub>2</sub>S<sub>8</sub>. This effect is more prominent at higher salt concentrations.

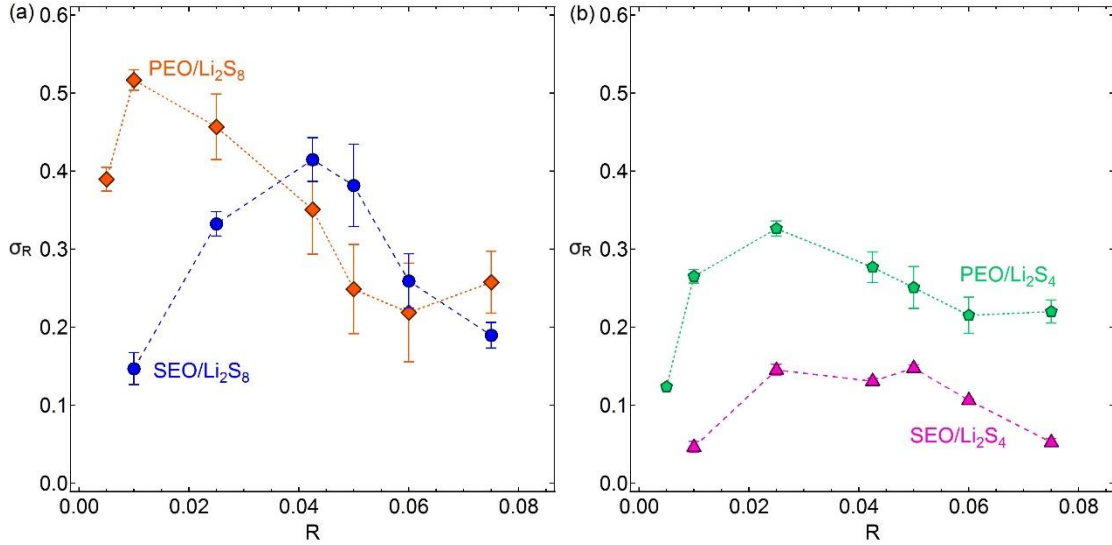


Figure 2.12. (a) Temperature-averaged ratio of polymer/Li<sub>2</sub>S<sub>8</sub> conductivity to polymer/LiTFSI conductivity,  $\sigma_R$ , versus salt concentration,  $R$ , and (b) temperature-averaged ratio of polymer/Li<sub>2</sub>S<sub>8</sub> conductivity to polymer/LiTFSI conductivity,  $\sigma_R$ , versus salt concentration,  $R$ .

In Li-S battery applications, one is interested in suppressing migration of polysulfides without interfering with the migration of the electrolyte salt. It is therefore instructive to examine  $\sigma_R$  defined as the ratio of conductivity of the polymer of interest containing Li<sub>2</sub>S<sub>x</sub> to the conductivity of the same polymer containing LiTFSI at the same value of  $R$ .

$$\sigma_R = \frac{\sigma_{\text{polymer/Li}_2\text{S}_x}}{\sigma_{\text{polymer/LiTFSI}}} \quad (7)$$

Suppression of Li<sub>2</sub>S<sub>8</sub> migration due to the nanostructured nature of SEO is only seen at low salt concentrations;  $\sigma_R$  of SEO is less than that of PEO when  $R < 0.04$  (Figure 2.12a). At higher salt concentrations,  $\sigma_R$  of Li<sub>2</sub>S<sub>8</sub> in SEO and in PEO are comparable, indicating no suppression due to the presence of a nanostructured electrolyte. In contrast, Li<sub>2</sub>S<sub>4</sub> migration in SEO is significantly suppressed compared to that in PEO (Figure 2.12b);  $\sigma_R$  of SEO is less than that of PEO over the entire concentration range. The  $\sigma_R$  versus  $R$  curves of SEO/Li<sub>2</sub>S<sub>x</sub> appeared to be peaked in the vicinity of  $R = 0.04$ , while those of PEO/Li<sub>2</sub>S<sub>x</sub> are peaked at significantly lower salt concentrations.

The data in Figures 2.7-2.12 indicate that Li<sub>2</sub>S<sub>x</sub> species dissociate in both PEO and SEO to generate carrier ions that contribute to ionic conductivity, and their conductivities are somewhat lower than those of LiTFSI in both PEO and SEO. More importantly, Li<sub>2</sub>S<sub>x</sub> migration can be partially suppressed by SEO, but cannot be prevented. However, since the diffusion coefficients and the cation transference numbers for polymer/Li<sub>2</sub>S<sub>x</sub> samples have not yet been measured, it is not clear whether the suppression is due to a reduction in carrier concentration or a reduction in mobility.<sup>25</sup>

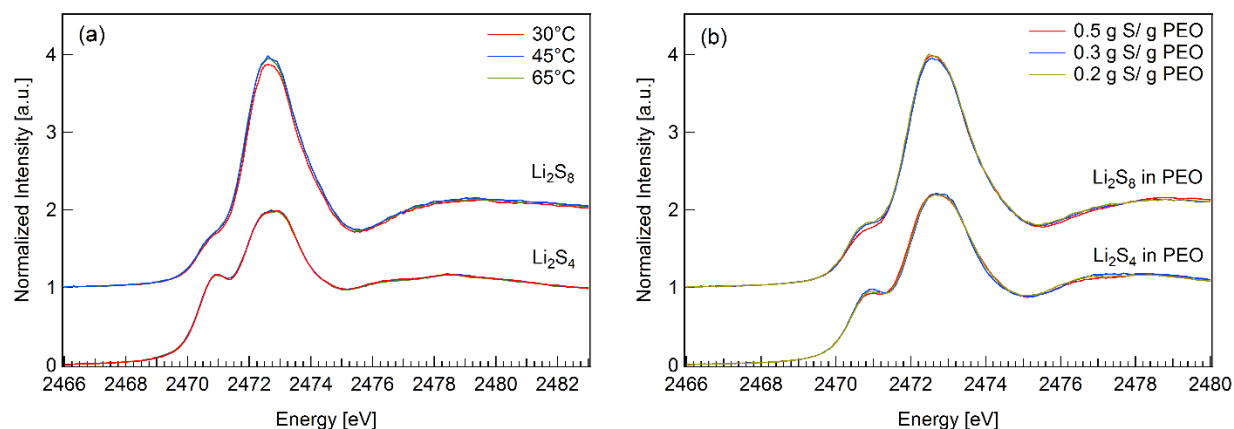


Figure 2.13. XAS sulfur K-edge spectra of  $\text{Li}_2\text{S}_4$  and  $\text{Li}_2\text{S}_8$  in PEO at (a) temperatures of 30, 45, and 65°C, and (b) sulfur concentrations of 0.2, 0.3 and 0.5 g of S per g of PEO. The overlapping spectra suggests no changes in polysulfide speciation as temperature and salt concentration is changed. The range of  $R$  values covered are 0.034 to 0.086 for  $\text{Li}_2\text{S}_8$  and 0.069 to 0.172 for  $\text{Li}_2\text{S}_8$ .

In Figure 2.13, we show XAS spectra obtained from PEO/ $\text{Li}_2\text{S}_8$  and PEO/ $\text{Li}_2\text{S}_4$  mixtures at a variety of temperatures and salt concentrations. The spectra of  $\text{Li}_2\text{S}_8$  and  $\text{Li}_2\text{S}_4$  do not depend on either temperature or salt concentration. We therefore conclude that these species are maintained over the salt concentration and temperature ranges used in these experiments. While we cannot make concrete conclusions about the nature of the polysulfide mixtures used in our study of morphology and conductivity, the data in Figure 2.13 suggest that  $\text{Li}_2\text{S}_8$  and  $\text{Li}_2\text{S}_4$  are likely to remain intact over the temperature and salt concentration range of interest. In reference 29 it was shown that XAS spectra of  $\text{Li}_2\text{S}_x$  ( $x = 2$  through 8) in SEO and PEO were identical. We thus do not expect the presence of the polystyrene block to affect speciation in SEO.

## 2.4 Conclusions

The morphology and the thermal properties of a polystyrene-*b*-poly(ethylene oxide) (SEO) block copolymer containing lithium polysulfides ( $\text{Li}_2\text{S}_x$ ;  $x=4, 8$ ) were studied using small angle X-ray scattering and differential scanning calorimetry. Both SEO/ $\text{Li}_2\text{S}_8$  and SEO/ $\text{Li}_2\text{S}_4$  samples showed a lamellar morphology at all concentrations. The crystallinity of the PEO lamellae was suppressed due to the presence of  $\text{Li}_2\text{S}_x$ , and this suppression was more significant in the case of SEO/ $\text{Li}_2\text{S}_8$  samples relative to SEO/ $\text{Li}_2\text{S}_4$  samples, suggesting that the interactions between PEO and  $\text{Li}_2\text{S}_8$  are more favorable.

The conductivities of SEO/ $\text{Li}_2\text{S}_x$  and PEO/ $\text{Li}_2\text{S}_x$  samples were measured by ac impedance spectroscopy. The conductivities of both SEO and PEO samples containing  $\text{Li}_2\text{S}_8$  are higher than the same polymer containing  $\text{Li}_2\text{S}_4$  at all salt concentrations, indicating that dissociation of  $\text{Li}_2\text{S}_8$  occurs more readily than  $\text{Li}_2\text{S}_4$ . We used normalized conductivity,  $\sigma_n$ , to focus on the effect of morphology on ion transport. Using this analysis, we show that SEO suppresses the migration of polysulfides relative to PEO.

Our study was motivated by the possibility of using nanostructured block copolymer electrolytes to suppress polysulfide migration in Li-S batteries. To examine this possibility, we evaluated  $\sigma_R$ , the ratio of the conductivity of SEO/Li<sub>2</sub>S<sub>x</sub> mixtures to that of SEO/LiTFSI mixtures; LiTFSI is a salt that is commonly used in batteries with PEO-based electrolytes. The values of  $\sigma_R$  range from 0.1 to 0.4 in the case of Li<sub>2</sub>S<sub>8</sub>, and from 0.04 to 0.15 in the case of Li<sub>2</sub>S<sub>4</sub>. This suppression is inadequate for practical applications. In other words, cathode architectures that prevent polysulfides from entering the electrolyte are necessary for enabling Li-S batteries with block copolymer electrolytes. Nevertheless, the results obtained in this study are important as they enable quantification of polysulfide migration in Li-S batteries with imperfect polysulfide encapsulation, a limitation that applies to all known Li-S batteries. To our knowledge, our work represents the first systematic investigation of the effect of molecular structure of polymer electrolytes on polysulfide migration.

## 2.5 Acknowledgements

This work was supported by the Office of Science, Office of Basic Energy Science, U.S. Department of Energy, under Contract DE-AC02-05CH11231 under the Soft Matter Electron Microscopy Program. SAXS measurements were carried out at the Advanced Light Source (Lawrence Berkeley National Lab), beamline 7.3.3, supported by the Office of Science, Office of Basic Energy Science, U.S. Department of Energy, under Contract DE-AC02-05CH11231. XAS experiments were carried out at the Stanford Synchrotron Radiation Lightsource, SLAC National Accelerator Laboratory, supported by the U.S. Department of Energy, Office of Science, Office of Basic Energy Sciences under Contract No. DE-AC02-76SF00515. Elemental analysis is supported by the Microanalytical Laboratory of UC Berkeley, College of Chemistry.

The authors gratefully acknowledge Tod Pascal and David Prendergast for providing the simulation results in Figure 2.1, Elena Kreimer for her assistance in elemental analysis, and Chenhui Zhu of the Advanced Light Source for his help with the X-ray scattering experiments.

## 2.6 Supporting Information

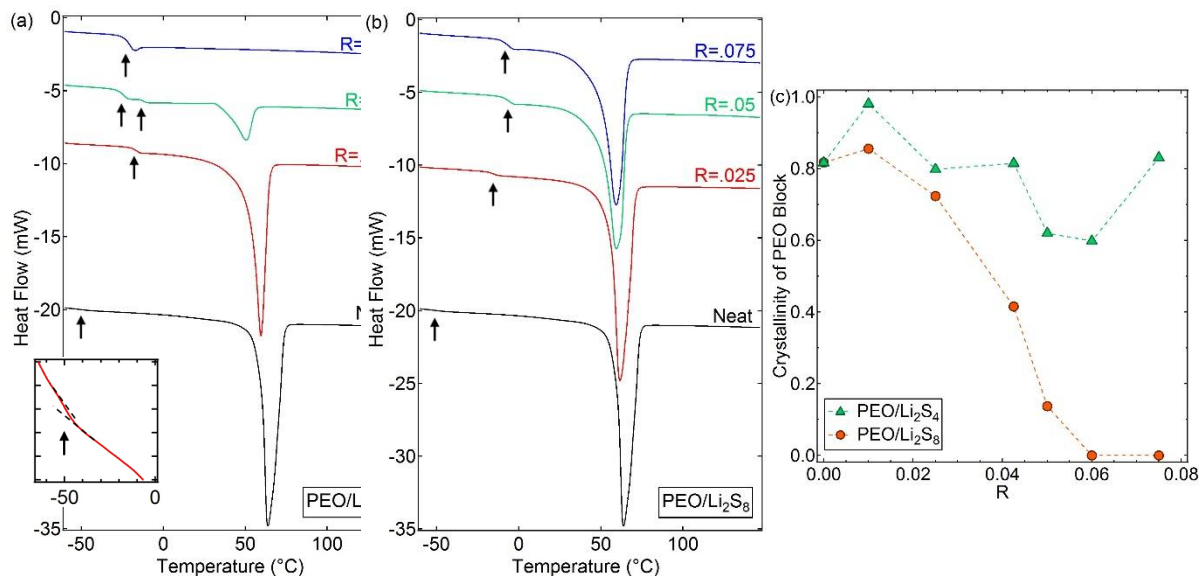


Figure S2.1. DSC scans of (a) PEO/Li<sub>2</sub>S<sub>8</sub> and (b) PEO/Li<sub>2</sub>S<sub>4</sub>. Scans are offset for clarity. Inset in (a) shows the DSC scan of neat PEO on an expanded scale. Arrows show  $T_g^{\text{PEO}}$ . (c) Effect of salt concentration,  $R$ , on the crystallinity of the PEO for PEO/Li<sub>2</sub>S<sub>x</sub> samples.

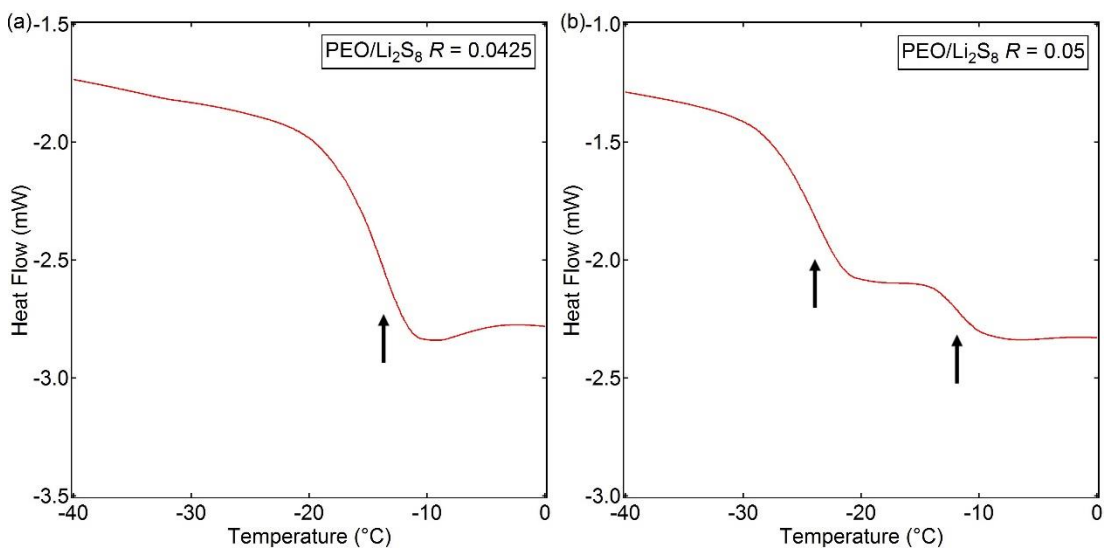


Figure S2.2. Expanded view of DSC scans of PEO/Li<sub>2</sub>S<sub>8</sub> samples with (a)  $R = 0.0425$  and (b)  $R = 0.05$ . Arrows show  $T_g^{\text{PEO}}$ .



## Chapter 3 – Experimental Uv-vis Spectra of Solvated Lithium Polysulfides<sup>†</sup>

### 3.1 Background

There is considerable interest in rechargeable lithium-sulfur batteries because their theoretical specific energy, 2600 Wh/kg, is five times greater than that of current lithium-ion batteries.<sup>30</sup> Elemental sulfur is abundant, nontoxic, and inexpensive compared to cobalt- and iron-based cathodes in conventional lithium-ion batteries.<sup>31</sup> Despite of those advantages, commercial application of lithium-sulfur batteries is limited due to the complexity of the species involved in the redox reactions that produce energy. During the discharge of lithium-sulfur batteries, lithium polysulfide intermediates with chemical formulae  $\text{Li}_2\text{S}_x$  where  $x$  ranges from 2 to 8, are formed. Some of these polysulfides diffuse out of the cathode and dissolve in the electrolyte, migrate towards the anode and results in a permanent loss of active materials in the cathode, shuttle mechanism between the electrodes, capacity fade, formation of an insulating layer at the electrolyte/anode interface, and the compromise of cell life.<sup>9,33,70</sup>

Recent work has focused on designing nanostructured cathodes that confine sulfur and polysulfides within the cathode without impeding transport of lithium ions and electrons that are necessary for the redox reactions.<sup>12–15</sup> While these efforts have improved the cycle life of lithium-sulfur batteries, the diffusion of polysulfides out of the cathode towards the anode has not been completely eliminated. One missing key in attempting to solve the polysulfide dissolution problem is the lack of knowledge of the lithium-sulfur redox reaction mechanism. Design mechanism requires a better understanding of the polysulfide intermediate species formed during the reaction, such as which species are formed, when they are formed and how much of them are formed within the cathode in order to provide chemical and physical methods to solve the problem.

UV-visible spectroscopy has been one of the major techniques used to characterize the polysulfides because polysulfides are well known to absorb UV and visible radiation. UV-vis spectroscopy probes the electron excitations between the molecular orbitals. Polysulfide molecules absorb UV and visible light when the energy of the photons equals to the energy needed to cause transitions between different electronic energy levels. The electronic energy levels are superimposed by many vibrational and rotational energy levels in the molecules and result in broadening of the absorption bands.<sup>71</sup> In solution where there is solvent-solute interactions, the broadening of the absorption bands is even greater. Typical wavelength ranged used to characterize polysulfides is 200 – 800 nm.

Early work of polysulfides were done on sodium and potassium polysulfides synthesized and characterized in the crystalline state, such as  $\text{Na}_2\text{S}_2$ ,  $\text{Na}_2\text{S}_4$ ,  $\text{K}_2\text{S}_2$ ,  $\text{K}_2\text{S}_4$ ,  $\text{K}_2\text{S}_6$ .<sup>72</sup> The only crystalline state lithium polysulfide reported is  $\text{Li}_2\text{S}_2$ .<sup>73–75</sup> However, non-aqueous lithium polysulfide solutions can be made chemically or electronically by the following three ways: (1) direct reaction of elemental S with Li metal,  $2\text{Li} + \frac{x}{8}\text{S}_8 \leftrightarrow \text{Li}_2\text{S}_x$ ; (2), reaction of elemental S with lithium sulfide

---

<sup>†</sup> Part of this work (Figure 3.1 and Figure 3.2) were reported in *J. Phys. Chem. C* **120**, 18403-

18410 (2016)

(Li<sub>2</sub>S),  $\text{Li}_2\text{S} + \frac{x-1}{8} \text{S}_8 \leftrightarrow \text{Li}_2\text{S}_x$ ; (3), electrochemical reduction of S<sub>8</sub>.<sup>30</sup> Absorbance peaks of polysulfides varied in different solvents produced with different methods. The identities of the absorption peaks disagreed from literature to literature, but some have reached agreement over the years. The biggest debate of the polysulfide peaks in literature was probably the assignment of the peak around 617 nm corresponds to a brilliant blue color in polysulfide contained solutions and solids. It was first attributed to the neutral molecules S<sub>x</sub> (x = 2-4) in the 1960s.<sup>76</sup> Later, Giggenbach et al.<sup>77</sup> repeatedly attributed this peak to the disulfide radical anion, S<sub>2</sub><sup>•-</sup>. In the early 1970s, Gruen et al.<sup>78</sup> and Chivers et al.<sup>79</sup> used a combination of ESR, UV-vis, infrared, and resonance Raman spectroscopy and pointed out that the blue color comes from the trisulfur radical anion, S<sub>3</sub><sup>•-</sup>. S<sub>3</sub><sup>•-</sup> and S<sub>2</sub><sup>•-</sup> often coexist in nature,<sup>72</sup> S<sub>2</sub><sup>•-</sup> has a yellow color with an absorbance peak at around 380 nm, and varying the concentration ratio of the two radical anions, S<sub>3</sub><sup>•-</sup> : S<sub>2</sub><sup>•-</sup>, the color of the material will turn from violet-blue (high ratio) to steel-blue, and green (low ratio).<sup>80</sup> Table 1 below shows a summary of peak assignments with different solvents and methods of producing polysulfide solutions by several literature.

Table 1: UV-vis Absorption Peak Assignments in Non-aqueous Solvents in literature; Method A,  $2\text{Li} + \frac{x}{8} \text{S}_8 \leftrightarrow \text{Li}_2\text{S}_x$ ; B,  $\text{Li}_2\text{S} + \frac{x-1}{8} \text{S}_8 \leftrightarrow \text{Li}_2\text{S}_x$ ; C, electrochemical reduction of S<sub>8</sub>

Solvent (dielectric constant)	Method	Absorbance Peak Wavelength (nm)								
		S <sub>8</sub>	S <sub>8</sub> <sup>2-</sup>	S <sub>7</sub> <sup>2-</sup>	S <sub>6</sub> <sup>2-</sup>	S <sub>5</sub> <sup>2-</sup>	S <sub>4</sub> <sup>2-</sup>	S <sub>3</sub> <sup>2-</sup>	S <sub>2</sub> <sup>2-</sup>	S <sub>3</sub> <sup>•-</sup>
<b>DMSO</b> (46.7)	A <sup>81</sup>		492		475		420			618
	C <sup>82</sup>		490, 380		450, 340		310-325	260-270		605-625
<b>DMA</b> (37.8)	C <sup>83</sup>		518,365		450-460					618
<b>DMF</b> (36.7)	C <sup>*</sup>		490, 355	470	450	437	420	330	280	600
	C <sup>84</sup>		500							617
<b>THF (7.58)</b>	A <sup>85</sup>	265					435,285			620-625
<b>TEGDME</b> (7)	B <sup>23</sup>	270-280	560		470,350,300,260	450	420	340		617
	B <sup>71</sup>						503,		338,	

							415, 300		236	
	C <sup>24</sup>	265			332		425			615
<b>Ionic liquid</b>	C <sup>86</sup>				460, 350		440			620

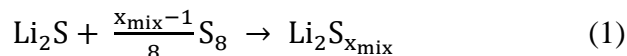
Light absorption in the range of 400 nm to 500nm region is generally attributed to the dianion species S<sub>4</sub><sup>2-</sup>, S<sub>6</sub><sup>2-</sup>, and S<sub>8</sub><sup>2-</sup>.<sup>30,53</sup> It is generally believed that polysulfides with longer chain lengths absorb light at higher wavelengths.<sup>24,30</sup> When chain length increases, the average negative charge density on each sulfur atom decreases,<sup>1</sup> which decreases the HOMO-LUMO gap and moves the primary absorption band toward a longer wavelength. Rauh et al.<sup>30</sup> studied the solubility of polysulfides in several solvents, and found that the solubility increased with the basicity of the solvent, which is related to the Gutmann donor number. They also concluded that the solvent dielectric constant plays a major role in the stability of polysulfide radicals; specifically, polysulfide radicals are produced and stabilized in high dielectric constant solvents, and are not produced in solvents with low dielectric constants such as THF and MA. Supporting this argument, Marmorstein et al.<sup>71</sup> used UV-vis to study chemically produced lithium polysulfide solution in TEGDME, a solvent with a low dielectric constant similar to that of THF, and observed no polysulfide radicals exist. However, recent work has shown that S<sub>3</sub><sup>•-</sup> is stable in TEGDME.<sup>22,23</sup> Canas et al.<sup>24</sup> studied polysulfides dissolved in TEGDME at different concentrations using UV-vis spectroscopy in an Argon filled glove box and observed the absorbance peak at 615 nm corresponds to S<sub>3</sub><sup>•-</sup> radical. Barchasz et al.<sup>23</sup> compared ex-situ UV-vis, ESR, HPLC, and cyclic voltammetry techniques to study Li-S reactions in TEGDME, and proposed a reaction mechanism for sulfur reduction consisting of three steps related to the three plateaus observed in the discharge profile. Long-chain polysulfides such as S<sub>8</sub><sup>2-</sup> and S<sub>6</sub><sup>2-</sup> were produced in the first step, followed by S<sub>4</sub><sup>2-</sup> in the second step, and short-chain polysulfides such as S<sub>3</sub><sup>2-</sup>, S<sub>2</sub><sup>2-</sup>, and S<sup>2-</sup> in the final step. They also claimed that S<sub>3</sub><sup>•-</sup> were produced through the disproportionation reaction, S<sub>6</sub><sup>2-</sup> ↔ 2 S<sub>3</sub><sup>•-</sup>, during the first and second discharge steps. Polysulfide concentration and spectrometer sensitivity might be the reason of the different observations.

In this chapter, we first evaluated the ex-situ uv-vis spectra of chemically synthesized lithium polysulfides in TEGDME to discuss the ambiguity in polysulfide dianion speciation and show the existence of radicals. We then examined the in-situ setups and challenges for Li-S reaction mechanism study. From there we explored a new fluorinated-ether based electrolyte to study reaction mechanism. Challenges and work still needed in order to do in-situ mechanism study were also discussed at the end of this chapter.

## 3.2 Ex-situ UV-vis Study on lithium polysulfides dissolved in ether

### 3.2.1 Lithium polysulfide solution preparation

Solutions of lithium polysulfide dissolved in TEGDME ( $\text{Li}_2\text{S}_{x_{\text{mix}}} \mid \text{TEGDME}$ ) were prepared by adding stoichiometric amounts of  $\text{S}_8$  and  $\text{Li}_2\text{S}$  to TEGDME. The amounts of  $\text{S}_8$  and  $\text{Li}_2\text{S}$  added to solutions were controlled by the following formula:



Here  $x_{\text{mix}}$  is used to denote the polysulfide dianion that would be obtained if a single dianion polysulfide type were formed by the reaction. In reality, the solution is likely a mixture of various polysulfide species in equilibrium, formed through various disproportionation reactions. This distribution of polysulfide species can include both dianions (of the form  $\text{Li}_2\text{S}_x$ ) and radical species (of the form  $\text{LiS}_x$ ). Here  $x_{\text{mix}}$  is used simply as a descriptor of the atomic ratio of lithium to sulfur. Solutions were mixed for at least 24 h at 90 °C in a sealed vial within an argon-filled glovebox. Solution sulfur concentrations used here represent the overall atomic moles of sulfur per volume of solution. For instance, a 10 mM concentration solution contains 10 mmol of atomic S per liter of solution. The millimoles of S atoms represents the sulfur added in the form of  $\text{S}_8$  and  $\text{Li}_2\text{S}$ . To maintain consistent  $x_{\text{mix}}$  values throughout the study, “bulk”, high-concentration solutions were made for each  $x_{\text{mix}}$  value which were then used to produce the lower concentration solutions through dilution. For instance, the  $x_{\text{mix}} = 6$  solutions were made by first preparing a bulk  $x_{\text{mix}} = 6$ , 300 mM solution. This 300 mM solution was then diluted to create the 100, 50, and 10 mM solutions. This procedure was used for all  $x_{\text{mix}}$  values. Additions of TEGDME were performed using a micropipette.

### 3.2.2 UV-vis Spectroscopy measurements

Liquid lithium polysulfide solutions were loaded into quartz cuvette sample holders inside an argon-filled glovebox. The quartz cuvettes had a path width of 1 mm. After loading, the cuvettes were sealed and then placed in closed vials with Teflon tape wrapped between the glass threading of the vial and the cap. The vials were then brought out of the glovebox and to the UV-vis spectrophotometer. These cuvettes containing the samples were taken out of the vials and immediately measured. An Agilent Cary 5000 UV-vis-NIR spectrophotometer was used to measure the samples in a range of wavelengths spanning 200–820 nm. Data were obtained in transmission mode. UV-vis spectra were taken in the range of 300 – 800 nm, below 300 nm, absorbance spectra became oversaturated. Solvent spectra were subtracted from the polysulfide solution spectra. All solutions were measured at room temperature.

### 3.2.3 Ex-situ UV-vis spectra for $\text{Li}_2\text{S}_{x_{\text{mix}}}$ | TEGDME solutions

$\text{Li}_2\text{S}_{x_{\text{mix}}}$  | TEGDME solutions for  $x_{\text{mix}}$  values of 4, 6, 8, and 10 and sulfur concentrations of 10, 50, and 100 mM were prepared for UV-vis measurements. Figure 3.1 shows the different colors of these solutions













TEGDME Concentration ( $C_s$ )	$x_{\text{mix}}$ value			
	4	6	8	10
10 mM				
50 mM				
100 mM				

Figure 3.1. Photographs of UV-Vis Cuvettes Filled with  $\text{Li}_2\text{S}_{x_{\text{mix}}}$  | TEGDME Solutions

All solutions with  $x_{\text{mix}}$  values equal to 4 were green in color for all concentrations. The higher the concentration, the deeper the green. For  $x_{\text{mix}} = 6$ , solutions were light yellow/green at 10 mM, and then became a dark olive/brown color at high concentrations. Solutions with  $x_{\text{mix}} = 8$  were light yellow/green in color at 10 mM, orange/brown at 50 mM, and dark red at 100 mM. The  $x_{\text{mix}} = 10$  solutions were light yellow at 10 mM, orange/brown at 50 mM, and dark red at 100 mM. None of the solutions are blue, the color corresponds to radicals.

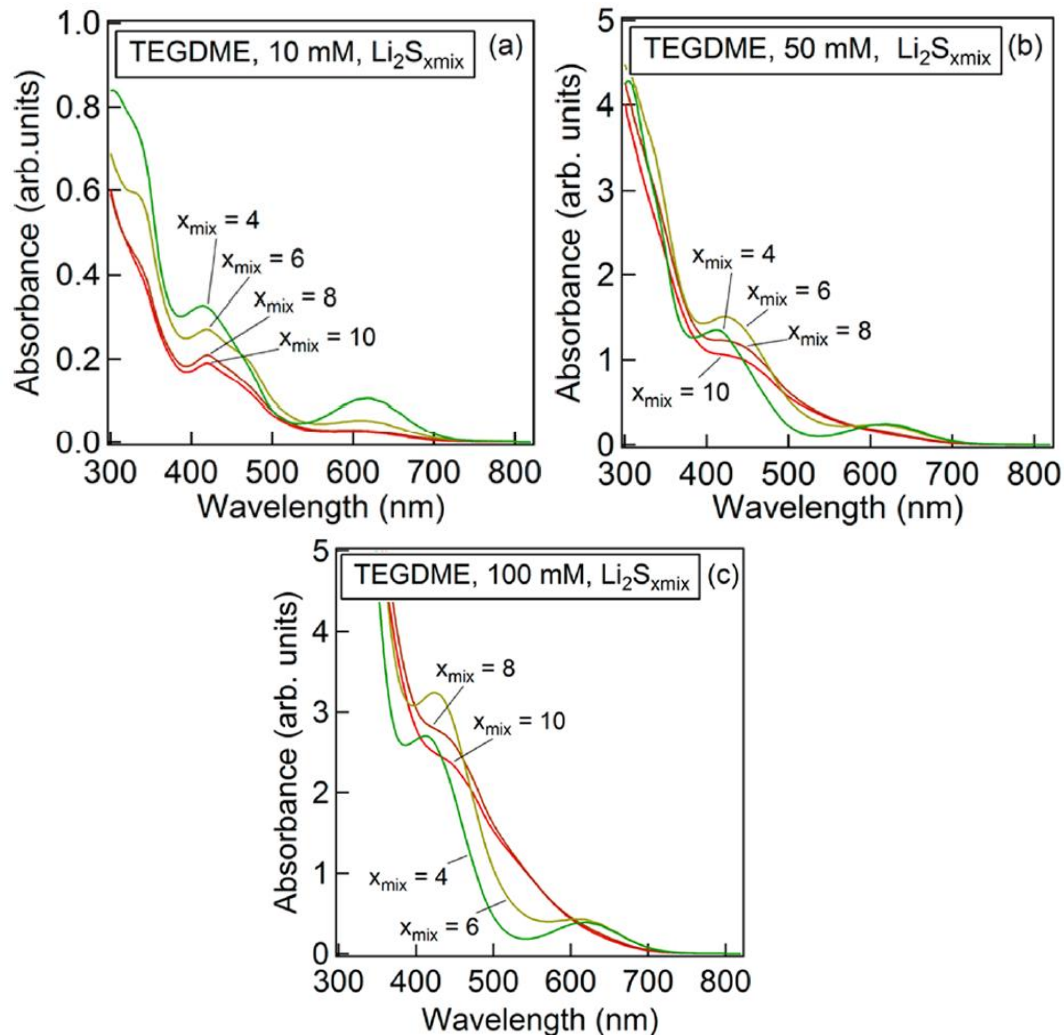


Figure 3.2. UV-vis spectra for lithium polysulfides dissolved in TEGDME solutions at sulfur concentrations of (a) 10 mM, (b) 50 mM, and (c) 100 mM. Corresponding colors:  $x_{mix} = 4$  (green),  $x_{mix} = 6$  (yellow),  $x_{mix} = 8$  (brown),  $x_{mix} = 10$  (red).

Figure 3.2 shows ex-situ UV-vis spectroscopy results for lithium polysulfide dissolved in TEGDME at a variety of  $x_{mix}$  values and sulfur concentrations. For all spectra we observe peaks in three regions, a peak around 340 nm, peaks between 400 – 500 nm, and a broad peak at 617 nm. For ether-based solvents, the peak at 340 nm has been attributed to attributed this peak to  $S_6^{2-}$  dianion,<sup>23</sup> others have attributed this to  $S_3^{2-}$  dianion or  $S_2^{2-}$  dianion<sup>71</sup>. In our results, this peak is the most resolved for low concentrations (10 mM sulfur), and is the strongest for  $x_{mix} = 6$ , which suggest that it may be related to  $S_6^{2-}$  dianion.

The 400 – 500 nm peak region is a little more complicated. For 10 mM solutions, all spectra have two distinctive peaks, one around 420 nm, and one around 480 nm. The relative intensity of the 420 nm peak compared to the peak at 480 nm for  $x_{mix} = 4$  is the largest, and gradually decrease as  $x_{mix}$  increases. The results support the findings by Barchasz et al.<sup>23</sup> that the peak at 420 nm is

related to  $S_4^{2-}$  dianion while the peak at 480 nm is related to longer chain polysulfides such as  $S_6^{2-}$  and  $S_8^{2-}$  dianions. For solutions with higher concentrations, all spectra appear to have only one broad peak, centered at 420 nm for  $x_{\text{mix}} = 4$ , 430 nm for  $x_{\text{mix}} = 6$ , and 460 nm for  $x_{\text{mix}} = 8$  and 10. The peaks for  $x_{\text{mix}} = 8$  and 10 also appear to be broader than the other two, suggesting a convolution of multiple absorbing centers. However, without reliable spectral standards, we cannot confirm the peak assignments and quantitatively determine the relative amount of each polysulfide species.

Lastly, we examine the peak at 617 nm, which is attributed to  $S_3^{\cdot-}$  radical anion. At a 10 mM sulfur concentration, the  $x_{\text{mix}} = 4$  solution has the highest absorbance at 617 nm, followed by  $x_{\text{mix}} = 6$ ,  $x_{\text{mix}} = 8$ , and  $x_{\text{mix}} = 10$ . At 50 mM,  $x_{\text{mix}} = 4$  and  $x_{\text{mix}} = 6$  appear to have similar absorbances at 617 nm, again followed by  $x_{\text{mix}} = 8$  and  $x_{\text{mix}} = 10$ . At 100 mM, an identical trend is observed. The resolved peak signal at 617 nm for  $x_{\text{mix}} = 4$  and  $x_{\text{mix}} = 6$  at all concentrations indicate that polysulfide radical anions are stable in TEGDME. The decrease in the relative peak intensity at 617 nm with increasing  $x_{\text{mix}}$  values seems to suggest that  $S_3^{\cdot-}$  radical anions are produced at a higher state of discharge in a Li-S cell. However, these radical anions are very sensitive to the total polysulfide concentrations, and are only observable with a UV-vis spectrometer at low sulfur concentrations, especially for high  $x_{\text{mix}}$  values.

### 3.3 In-situ UV-vis Setup for Li-S Mechanism Study

#### 3.3.1 Reported in-situ Li-S study using UV-vis Spectroscopy

In-situ experiments that measure the production of polysulfides during the discharge and charge of cells without stopping the cycling or opening up the cell may yield a better understanding of the reaction mechanism. To our knowledge, only two groups have done in-situ uv-vis study of Li-S batteries. Marmorstein et al.<sup>71</sup> used UV-vis spectroscopy to determine the polysulfide speciation dissolved in the solid poly(ethylene oxide) electrolyte with LiTFSI. The light transmit through part of the electrolyte with dissolved polysulfides during battery cycling at 90 °C. They first obtained “standard spectra” for each polysulfide species by dissolving polysulfides stoichiometrically in TEGDME, and used the standards to fit the in situ spectra. Their results indicated that only two polysulfides, Li<sub>2</sub>S<sub>2</sub> and Li<sub>2</sub>S<sub>4</sub>, were stable in the ethylene oxide polymer electrolyte with a single chemical equilibrium:  $\text{Li}_2\text{S}_2 + \frac{1}{4} \text{S}_8 \leftrightarrow \text{Li}_2\text{S}_4$ . They also investigated the effect of temperature on the equilibria of polysulfide species and concluded that increasing temperature shifted the equilibrium towards Li<sub>2</sub>S<sub>4</sub>, and therefore Li<sub>2</sub>S<sub>4</sub> was the primary soluble species in their electrochemical cells. They observed a 20 nm red shift of the in-situ spectra regard to the “standard spectra”, and attributed this red shift to be the interaction with solvent and LiTFSI salt. They also found that the in situ spectra had much broader peaks than the spectra in TEGDME, which was attributed to the higher molecular weight of the PEO electrolyte in the cell. This work however, only probed the species dissolved in the electrolyte, and therefore the result doesn't reflect the reactions happened in the cathode.

In a more recent work Patel et al.<sup>87</sup> studied Li-S battery reaction with a 1 M LiTFSI in TEGDME:DOL combination electrolyte in a reflection mode. In this work, second derivatives of the measured reflectance spectra was used to enhance the differences among the original spectra and to resolve overlapping bands. They observed the major change in peak positions happened between 400 – 650 nm. At the beginning of discharge, they observed a shift of peak towards higher wavelength, indicating the dissolution of long-chain polysulfides into the electrolyte. Continuous discharging shifted the absorption curve towards shorter wavelengths which was related to the formation of short-chain polysulfides. The spectra moved from short wavelengths to longer wavelengths, which corresponded to the change from short-chain polysulfides to long-chain polysulfides. They also found that the spectra at the end of charging was slightly shifted towards lower wavelength compared to the initial spectra, indicating the remaining of mid-length polysulfides in the electrolyte. The limitation of the reflection model is that the depth of light penetration is uncontrolled, and signal mainly came from the electrolyte instead of the cathode.

The main problem associated with these experiments is that both setup detects only the polysulfides dissolved in the electrolyte. In the work by Marmostein et al.<sup>71</sup>, UV-vis light is designed to only probe the ether electrolyte under transmission mode because the cathode is not transparent to light in UV-vis region. In the work by Patel et al.<sup>87</sup>, UV-vis light is used to probe from the anode side of the cell, and only part of the electrolyte layer was detected due to the low transmission depth of UV-vis light in an electrolyte saturated with absorbing species. Since the



nature of the electrolyte affects the solubility and the equilibrium conditions of polysulfide species, such measurements may not reflect the reactions happened inside the cathode.

### 3.3.2 Perfluoropolyether electrolyte

We need an electrolyte that absorbs little UV-vis light so that the light can reach the cathode and probe the polysulfides inside the cathode in order to do in-situ Li-S study with UV-vis reflection mode. An ether-based electrolyte that dissolves little polysulfides would allow us to detect the products in the cathode layer. We have discovered perfluoropolyether (PFPE) as a good candidate for dissolving little polysulfides while maintaining a decent ionic conductivity. The chemical structure of PFPE is shown in Figure 3.3.

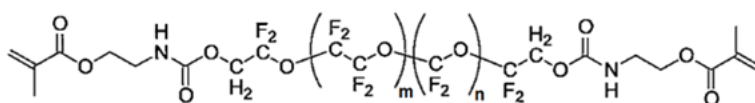


Figure 3.3. Chemical structure for perfluoropolyether

We examined the UV-vis light absorption of PFPE based electrolyte in a Li-S cell with ex-situ UV-vis transmission mode. An  $Li_2S_8$  based cathode is casted onto an aluminum mesh current collector. A lithium ring is used as an anode attached to a nickel ring with the same size for even charge distribution. These features were introduced to enable the passage of light through the cell. A solid electrolyte layer is used to separate the electrodes. We compared two types of electrolyte layer, one is a simple ether based electrolyte of polystyrene-b-poly(ethylene oxide) with lithium bis(trifluoromethanesulfonyl)imide (LiTFSI), SEO/LiTFSI, and the other one with a double layer of SEO/LiTFSI and PFPE/LiTFSI. Each cell is vacuum sealed using a pouch materials with quartz windows on both sides in a glove box, and then discharged and charged five times between 1.5 V and 3.2 V at a constant rate of C/40 using a Biologic Potentiostat. After the last cycle, the cells were taken to a UV-vis spectrometer for transmission measurement. Figure 3.4 is a schematic shows the cell configuration and ex-situ UV-vis measurement setup for the cell with PFPE.

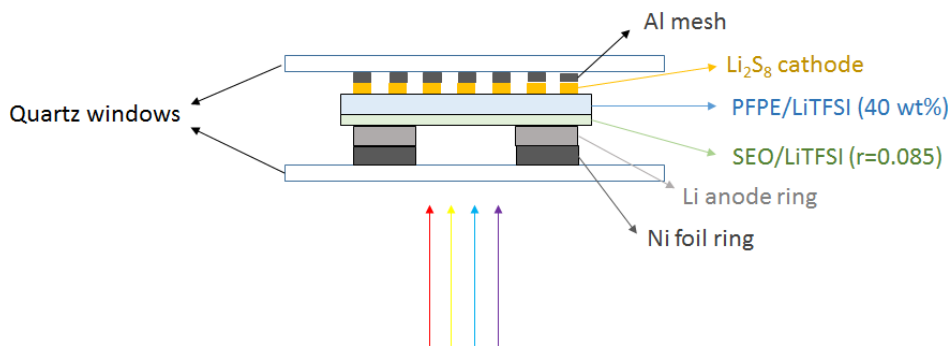


Figure 3.4. Schematic of ex-situ UV-vis measurement for a Li-S cell containing PFPE electrolyte

UV-vis light cannot pass through the thick lithium or nickel, nor parts with cathode and aluminum mesh on, however, it passes through the electrolyte layer and measures the absorbing species inside the electrolyte layer.

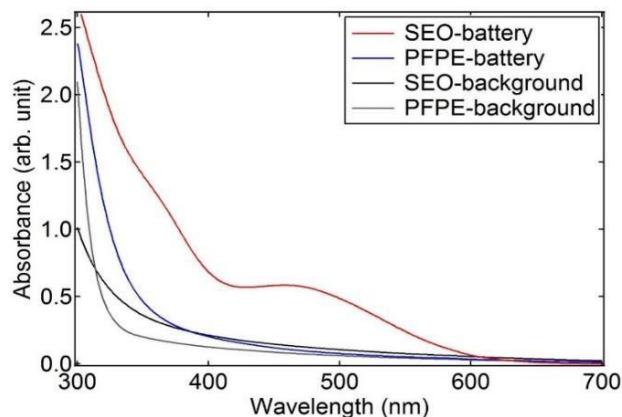


Figure 3.5. UV-vis transmission spectra of Li-S cell electrolyte after 5 cycles showing no polysulfide peaks (in blue) with the addition of a fluorinate layer (PFPE) indicating no polysulfide signal from the electrolyte versus the cell using just SEO electrolyte without PFPE layer (in red) showing indicating polysulfide signals coming from the electrolyte.

Figure 3.5 shows the spectra for the cells with only SEO electrolyte, cell with both SEO and PFPE electrolyte, and backgrounds of pure electrolyte films not in contact with sulfur containing species. The double bonds in polystyrene backbones absorb UV below 300 nm and are responsible for the rising in signal below 340 nm. Polysulfides absorb between 340 nm to 550 nm. From Figure 3.5 we see that all electrolyte films (SEO/LiTFSI, PFPE/LiTFSI) not in contact with sulfur do not have absorption peaks at wavelength above 340 nm. Comparing the spectra for the two cells, we clearly see polysulfide signals in the cell using only SEO/LiTFSI as the electrolyte. The absence of polysulfide peaks in the cell including PFPE/LiTFSI electrolyte indicates that little polysulfides dissolved into the electrolyte during cycling and that light transmission through the electrolyte layer is high for wavelength above 340 nm. Therefore, we can use PFPE as an electrolyte layer for in-situ Li-S study using UV-vis reflectance mode since most of the visible light that are sensitive to polysulfides can pass the electrolyte layer and probe the cathode. Figure 3.6 is a schematic shows the experimental setup for in-situ UV-vis study of such a cell.

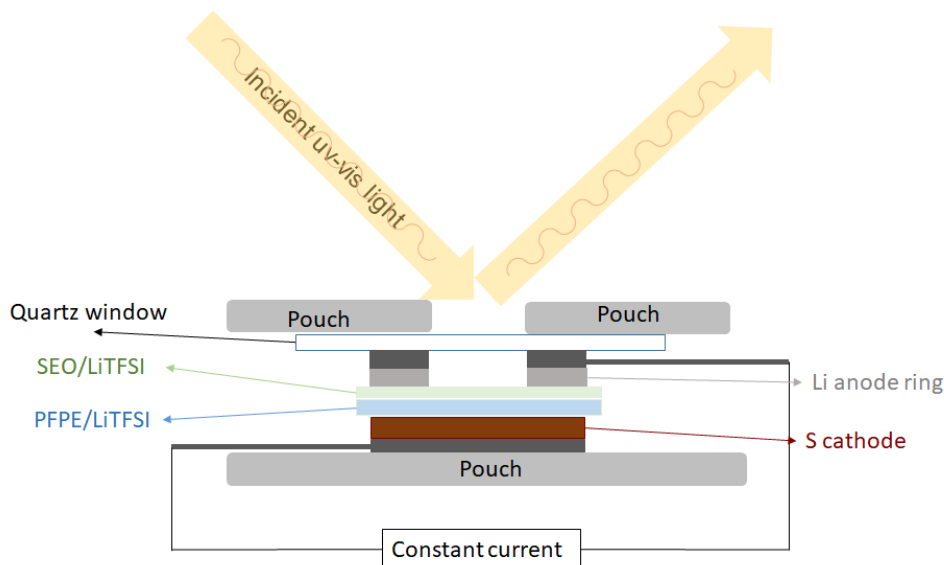


Figure 3.6. Schematic of in-situ UV-vis setup for Li-S reaction mechanism study using PFPE electrolyte

### 3.3.3 Challenges with in-situ UV-vis study for Li-S reactions

There are two main challenges associated with the current use of UV-vis spectroscopy technique in studying Li-S reactions. The first one is the difficulty to distinguish species that absorb at similar wavelengths. As shown in the ex-situ spectra in Figure 3.2, some broad peaks can be really difficult to deconvolute without knowing how many absorption centers are present.

Another challenge with the characterization of lithium polysulfides using UV-vis spectroscopy is the difficulty in getting standard spectra for each polysulfides. The current reference spectra are obtained by measuring stoichiometrically chemically mixed lithium polysulfide solutions. However, since lithium polysulfides cannot be separated, and the equilibrium of the different polysulfide species in those solutions are not certain, the measured spectra do not represent single species spectra. One way to solve this problem is through computational method. To our knowledge, the only computational calculation of polysulfides spectra was presented by Kawase et al.<sup>25</sup> This work uses Time-Dependent Density Functional Theory to simulate UV-vis spectra for lithium polysulfide molecules. However, the simulation performed in this work assumed a vacuum environment, and the optimized shape of polysulfide chains in vacuum were linear. Pascal et al.<sup>19</sup> performed MD simulation on lithium polysulfides in an explicit solvation environment with TEGDME and DMF, and found that the sulfur chains bend into a claw shape wrapping around one lithium ion in both solvents. Altering the structure and the interaction between polysulfides and solvent could change the excitation states. Therefore, a more complicated simulation with the consideration of the correct structure of polysulfides in a solvent and the effect of solvent-polysulfide interaction is needed to obtain more reliable reference spectra of lithium polysulfides.

### **3.4 Conclusions**

We reported experimental studies of Li-S reaction products using UV-vis spectroscopy. The spectra depend on the average state of discharge, as well as sulfur concentrations. Ambiguity in peak assignments arise both from convoluted multi-absorption centers, as well as lack of spectra standards for different polysulfides. We also concluded that polysulfide radical anions are stable in ether-based electrolytes. We reported a perfluoropolyether electrolyte materials that dissolves little polysulfides and can be used in in-situ Li-S reaction mechanism studies because of its absorption in visible light range. Finally, we discussed the challenges using UV-vis to study Li-S reaction mechanisms and concluded that computational methods are needed to explore UV-vis spectral standards for different lithium polysulfides.

### **3.5 Acknowledgements**

This work was supported by the Assistant Secretary for Energy Efficiency and Renewable Energy, Office of Vehicle Technologies of the U.S. Department of Energy under Contract DEAC02-05CH11231 under the Battery Materials Research program. UV-vis spectroscopy was performed under a User Project at The Molecular Foundry.

## Chapter 4 – Computational Optical Spectra of Solvated Lithium Polysulfides

### 4.1 Introduction

Coupling experimental spectroscopy methods and computational predictions of electronic excited states of molecules upon light irradiation has received considerable interest in the recent years.<sup>88</sup> These excited states calculations provide valuable insight into the chemistry of the reaction mechanisms.<sup>89</sup> For example, the theoretical X-ray absorption spectra calculated by Pascal et al.<sup>1,28</sup> were used to interpret the experimental spectra during discharge of a Li-S battery to study the intermediate species produced during cycling.

Linear response time dependent density functional theory (LR-TDDFT) has risen to be one of the most popular methods to calculate optical absorption and other spectra of medium- and large-sized molecules due to its unprecedented balance between accuracy and efficiency.<sup>90</sup> To our knowledge, there is only one published report on computation optical spectra of lithium polysulfides.<sup>91</sup> However, without a proper solvation model, the structures of the polysulfides are linear, which represents the equilibrium structure in vacuum, while polysulfides should obtain a claw-shaped structure while being solvated by ether molecules as demonstrated by Pascal et al.<sup>1</sup> Different structures may result in a completely different spectra due to the difference in local electron density distribution.

We aim to find out the complexity necessary to compute reliable optical spectra for solvated lithium polysulfides using TDDFT. TDDFT of molecules and clusters can be efficiently evaluated with localized basis sets, such as Gaussians. The Q-Chem quantum chemistry package<sup>92</sup> has been used here for such cluster calculations. As an alternative, to explore improved descriptions of condensed phases, we model them under periodic boundary conditions using a plane-wave basis set. These calculations use a finite-frequency generalization of density functional perturbation theory to compute optical absorption.<sup>93</sup>

In this study, we will compare the two methods within LR-TDDFT calculations applied to lithium polysulfides ( $\text{Li}_2\text{S}_x$  where  $x$  ranges from 2 to 8) in vacuum and solvent environments. Configurations of lithium polysulfides solvated in diglyme and dimethylformamide (DMF) structures were previously produced using first-principles molecular dynamics simulations.<sup>1</sup> We will systematically explore the necessary steps needed to produce physically representative optical spectra in these systems.

### 4.2 Structures

The original configurations of condensed phase lithium polysulfides solvated in diglyme and DMF molecules previously produced using first-principles molecular dynamics simulations has about 16 diglyme molecules per lithium polysulfide molecule or 27 DMF molecules per lithium polysulfide molecule. Each system has more than 100 configurations. For a particular configuration with a desired number of solvent molecules in Gaussian calculations, one unit cell

with one lithium polysulfide molecule and the surrounding solvent molecules are used, and extra solvent molecules were manually removed from the outer most solvation layer to the inner most (the ones directly coordinate with lithium). In order to explore the solvent effect, the configurations of polysulfides in vacuum were obtained by removing all solvent molecules around it in order to maintain a structure comparable to the ones used including solvent molecules.

## 4.3 Results and Discussion

### 4.3.1 Gaussian Calculations: Basis set and Functionals

Gaussian calculations require choosing a basis set, a set of one-particle functions used to build molecular orbitals, in combination with a functional, a theoretical approximation for the exchange-correlation energy. There are a lot of basis sets and functionals developed to choose from. In general, the bigger the basis set, the higher the level of functional used, the more reliable the calculated results, but suffer from higher computational costs. We will systematically examine three of the most widely used basis sets developed by Dunning et al.<sup>94</sup> : cc-pVDZ, cc-pVTZ, and cc-pVQZ. The 'cc-p', stands for 'correlation-consistent polarized' and the 'V' indicates they are valence-only basis sets. "DZ", "TZ", "QZ" each stands for double-zeta, triple-zeta, and quadruple-zeta, with increasing basis size. The choice of functional strongly depends on the chemical system.<sup>95</sup> The functional needed to describe covalently bonded isolated molecules would be different than the functional needed to describe ionic crystals and metal clusters. We decide to evaluate the three popular functionals in chemistry community: blyp, b3lyp, and cam-b3lyp (with increasing level of complication). Figure 4.1 (a) and (b) shows the results for calculating a Li<sub>2</sub>S complex.

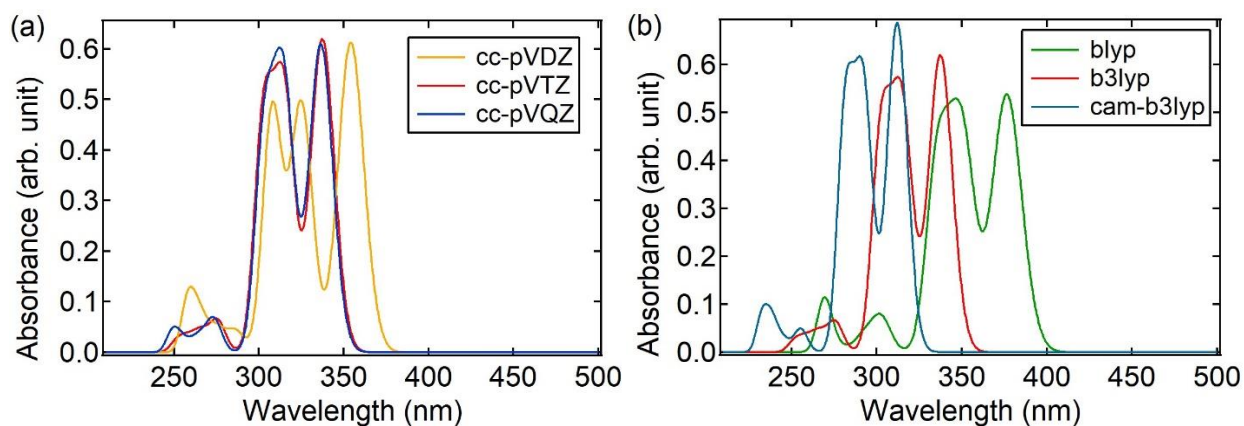


Figure 4.1 (a) Different basis sets and (b) functionals used to calculate Li<sub>2</sub>S

We look for numerical convergence in the spectra in order to select the least expensive model that gives us good accuracy. Figure 4.1(a) shows the calculations for different basis sets using b3lyp functional. Numerical convergence at cc-pVTZ is achieved but not at cc-pVDZ. Figure 4.1(b) shows the calculations for different functionals using cc-pVTZ basis set, and the result

shows no convergence. However cam-b3lyp takes significantly longer to compute, and would not be realistic in the larger systems we have, therefore we choose to use b3lyp for the rest of Gaussian calculations, because b3lyp is the most widely used functional in literature and has been proved to have a sufficient accuracy in many systems.<sup>96</sup>

#### 4.3.2 Gaussian Calculations: Solvent Effect

There are various solvent models to account for the behavior of solvated systems. The most common way is implicit solvent model, which represents solvent as a continuous medium surrounding the solute molecule. Implicit solvent models are generally computationally efficient, and are mostly used in liquids, where the [potential of mean force](#) can be applied to approximate the averaged behavior of many highly dynamic solvent molecules.<sup>97</sup> However, these models fail to account for the local fluctuations due to solvent ordering around a solute molecule. In contrast to the continuum models, explicit solvent models treat solvent molecules explicitly. Explicit solvent models can provide a better description of local solvent-solute interactions, but are more computationally expensive, especially in our Gaussian calculations where the computational time increases with the size of the system to the power of 3 to 4. We will examine the effect of solvent with different solvent models.

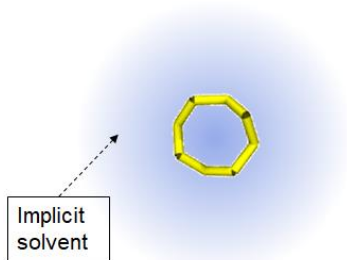


Figure 4.2. Schematic of an S<sub>8</sub> molecule with implicit solvent around it

We first wanted to see if including any solvent model will have effect on our calculations compared to putting a molecule in vacuum. To do that we examined one of commonly used implicit solvent models in Qchem, the Polarizable continuum model (PCM). Figure 4.2 shows a schematic of a S<sub>8</sub> molecule surrounded by a medium with a dielectric constant equal to that of diglyme.

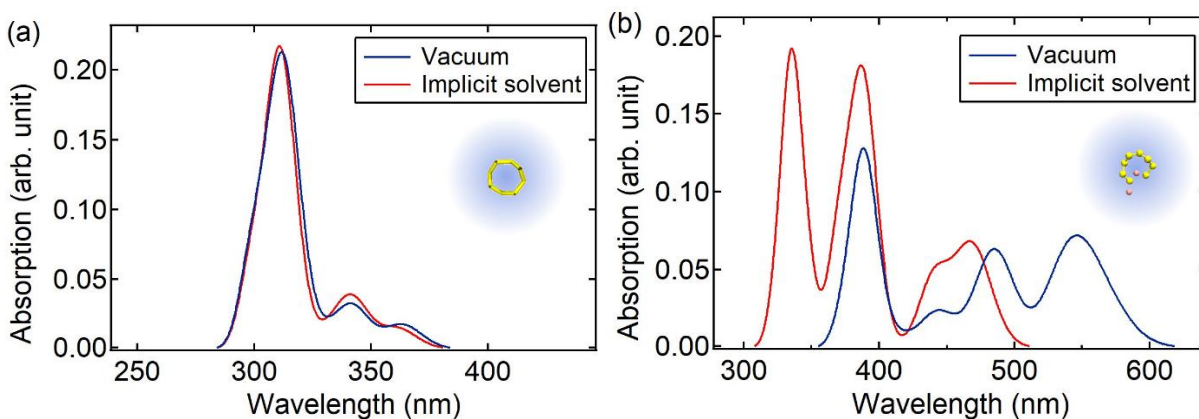


Figure 4.3 Comparing calculations of vacuum vs implicit solvent model for (a) an  $S_8$  molecule, and (b)  $Li_2S_8$  molecule surround by implicit solvent with the mean dielectric field equal to that of diglyme.

Figure 4.3 (a) shows the calculated optical spectra for  $S_8$  in vacuum and in an implicit solvent environment. The similarity in the spectra indicates that providing a continuum solvent model did not have any effect on the calculated spectra for an  $S_8$  molecule. However, when do we do the same comparison for an  $Li_2S_8$  molecule, the spectra look quite different indicating that solvent does affect the calculation. The difference in the two scenario originates from an uneven charge distribution in  $Li_2S_8$ . Implicit solvent model provides a dielectric constant equal to the solvent ( $\approx 7$ ) which is different than vacuum, and the dielectric constant affects the coulombic force that changes the electronic interactions.  $S_8$  have all delocalized charges and it doesn't have a dipole. Therefore, the effective charge on each sulfur atom is zero, indicates that the coulombic interaction between the atoms are zero, and will not be affected by the change in dielectric constant of the surrounding environment. On the other hand,  $Li_2S_8$  has more localized charges, and it has a dipole, therefore the additional dielectric constant term changes the electrostatic interactions and results in difference in calculated spectra. Although  $S_8$  optical spectra calculations may not be affected by solvent, all of the lithium polysulfides are similar to  $Li_2S_8$ , with localized electrons and therefore the spectra calculations depend strongly on solvent.



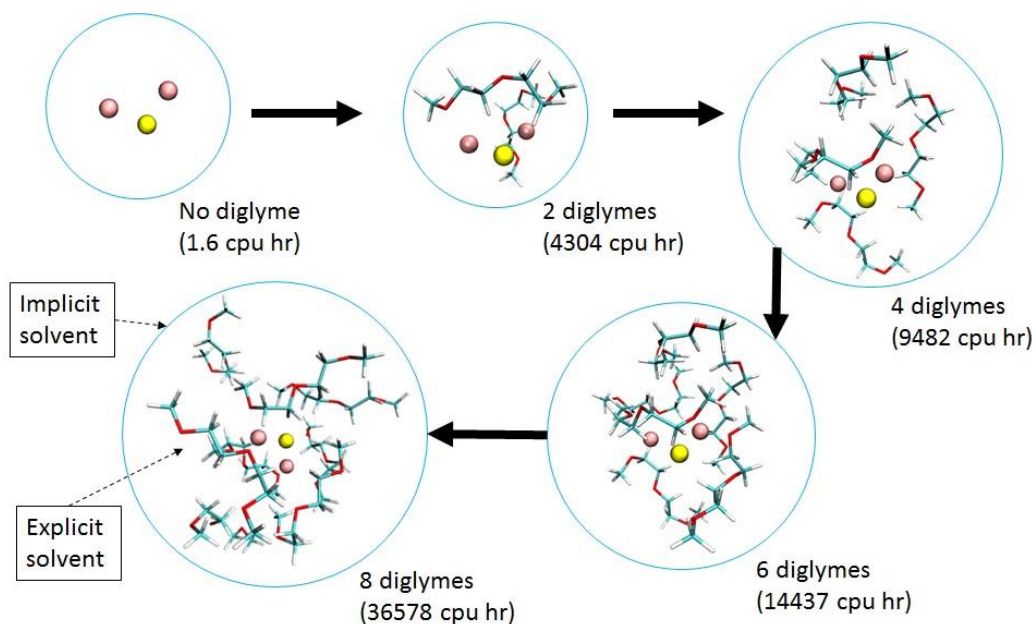


Figure 4.4. Adding 2 - 8 explicit molecules into the calculation, the numbers inside parenthesis indicates the number of cpu hours needed for the calculation

To examine the effect of local solvent-solute interactions, we explicitly add diglyme molecules in our system. Since adding explicit solvent molecules significantly increase the computational cost, we decided to use  $\text{Li}_2\text{S}$  as a theoretical example to explore explicit solvent effect on calculated spectra since  $\text{Li}_2\text{S}$  is a simple molecule and is similar to all other lithium polysulfides such that it has very localized point charges and it has a dipole. We slowly add 2 diglyme molecules at a time into the system, starting from the ones that closely coordinate with lithium ions, with implicit solvent filling up the space and the surrounding as illustrated in Figure 4.4. Explicit solvent calculations are less popular in literature due to its high computational cost. Due to the size of the computation, we used a smaller basis set, cc-pVDZ instead of cc-pVTZ, to explore explicit solvent effect, and the approximated cpu hours listed in parenthesis in Figure 4.5 corresponds to each spectra calculation.

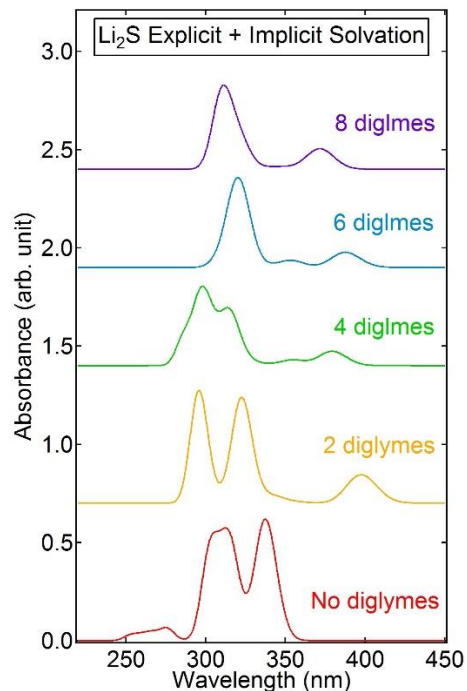


Figure 4.5. Calculated uv-vis spectra for  $\text{Li}_2\text{S}$  in diglyme with different number of solvent molecules

Figure 4.5 shows the calculated optical spectra for a solvated  $\text{Li}_2\text{S}$  molecule in diglyme using implicit-explicit hybrid solvent model with different numbers of explicit solvent molecules. The bottom line is results from implicit solvent model with no diglymes. The most amount of diglymes we included was eight. The significant change in spectra shape as we increase the number of diglyme molecules indicate a strong effect of local solvent-solute interactions on optical spectra calculation for a solvated  $\text{Li}_2\text{S}$  molecule. The spectra should eventually converge as we add more and more solvent molecules into the system that captures all local solvent-solute interactions. However in our calculations, the spectra has not quite converged with only eight diglyme molecules solvating the  $\text{Li}_2\text{S}$  molecule. Unfortunately we were unable to calculate spectra with more than 8 diglymes due to the increasing demand in computational space. Gaussian calculations are not parallel efficient and therefore all calculations had to be done on one node, a larger system would exceed our computational ability with Gaussian calculations.

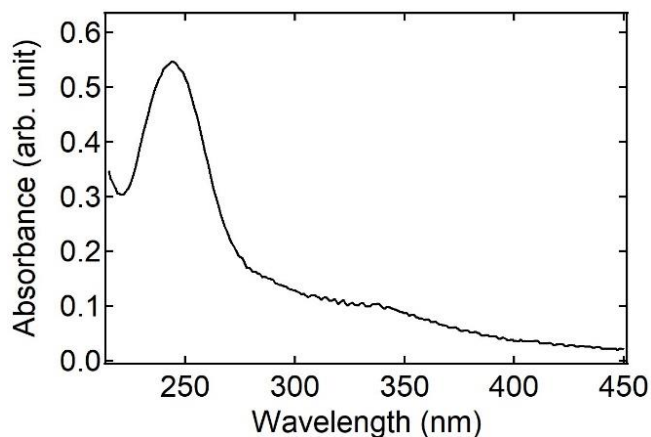


Figure 4.6. Experimental spectra of  $\text{Li}_2\text{S}$  in diglyme

Figure 4.6 shows the experimental optical spectrum for  $\text{Li}_2\text{S}$  in diglyme. Comparing Figure 4.5 and 4.6 we find that even our best calculation with 8 diglyme molecules and implicit solvent around  $\text{Li}_2\text{S}$  does not represent the experimental spectrum. The higher wavelength peak location is offset by about 50 nm, and the relative intensity of the two peaks differ significantly. The discrepancy between the calculated and the experimental spectra is due to: (1) The functional (b3lyp) and basis set (cc-pVDZ) used is not comprehensive enough (Figure 4.1), (2) Number of solvent molecules used is not enough as our spectra has not fully converged, and (3) The calculated spectrum represented one structure while the experimental spectra is an average over different solvated  $\text{Li}_2\text{S}$  structures.

(3) can be easily solved by calculating the spectra over many different structures obtained from MD simulation, and take the average. To solve (1) and (2), we both need higher computational power to accommodate the increased level of complexity in functionals and basis set, and system size. However increasing the level of complexity as well as system size would run into memory limits due to the inefficiency in parallel calculations for Gaussian methods. Therefore we will explore a parallel efficient method, plane wave calculations, to continue exploring what are the necessary steps to take to reliably compute optical spectra for solvated lithium polysulfides.

### 4.3.3 Plane-wave calculations

In a plane-wave calculation, the system is modeled under periodic boundary conditions instead of a finite cluster. These calculations use a finite-frequency generalization of density functional perturbation theory, a plane-wave basis set and pseudopotentials to compute optical absorption. The QUANTUM ESPRESSO suite<sup>93</sup> has been used for the calculations. In all the plane-wave calculations, the Brillouin zone is sampled at the  $\Gamma$ -point only, the exchange-correlation potential is substituted by the PBE generalized-gradient approximation.

We first optimize the parameters in plane-wave calculations using a system of an  $\text{Li}_2\text{S}_3$  molecule surrounded by two diglyme molecules in vacuum. Each of the lithium is coordinated by

two sulfur from the sulfur chain and two oxygen from diglyme. The parameters needed to be optimized are the wave function cutoff energy, size of the repeating unit (box size), and number of self-consistent iterations. We determined to the wave function cutoff energy to be 30 eV, beyond which the homo-lumo gap converges to three decimal points in eV. Number of iterations required depends on the box size selection, and the spectra are generally found to have converged at an iteration of 9000 for box size > 20 (Figure S4.1). We decided to use 10000 for all calculations. Figure 4.7 shows the convergence with increasing box size: (a) shows the schematic of increasing box size, and (b) the calculated spectra. All spectra presented in this section has the horizontal axis of energy in eV instead of wavelength in nm. An increase in energy corresponds to a decrease in wavelength.

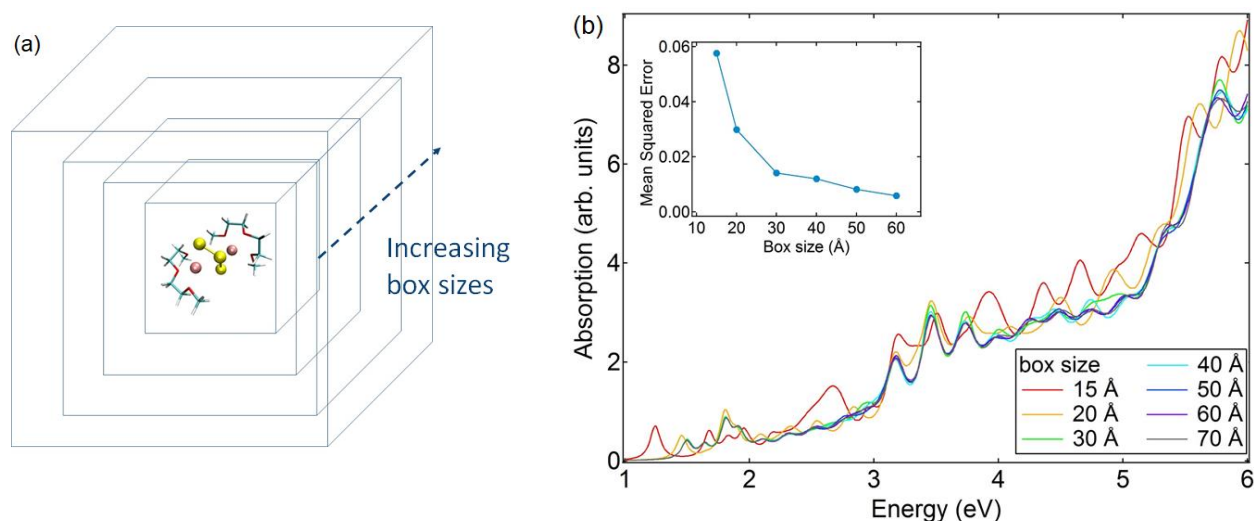


Figure 4.7. (a) Schematic and (b) plane wave spectra calculation of repeating unit cells of Li<sub>2</sub>S<sub>3</sub> with two diglyme molecules coordinating the lithium ions in a vacuum box

The spectra in Figure 4.7(b) converges with increasing box size. The spectra tend to differ more at higher energies. Since we are calculating optical spectra only, we only need to consider energy up to 6 eV (206.6 nm). The inset shows the mean squared error of box sizes from 15 to 60 with respect to box size 70, all calculated with 5000 iterations and 30 eV for wave function cut off energy. We see that at the spectra converges at box size of 40.

Theoretically, the optical spectra calculated using plane-wave calculations and Gaussian calculations with the same level of theory (PBE) for the same system in vacuum for the same system should be the same if all parameters are optimized. In practical, we compare the two methods by finding the most optimized configuration for both calculations. Figure 4.8 compares the most optimized plane-wave basis set calculations to Gaussian calculations using different basis sets for the system of two diglyme molecules per Li<sub>2</sub>S<sub>3</sub> molecule.

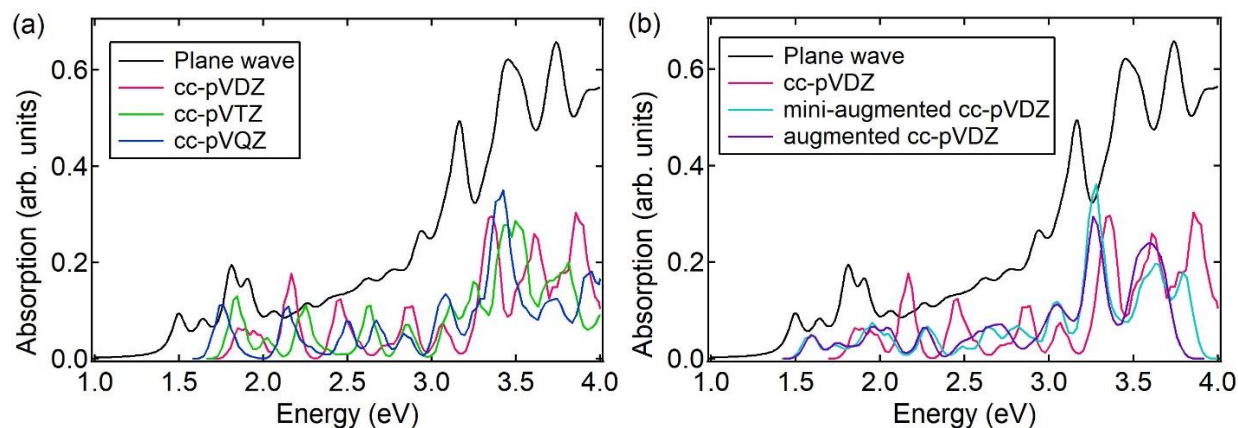


Figure 4.8. Comparing plane wave calculations to Gaussian calculations with (a) non-augmented basis sets and (b) augmented basis sets of a cluster of  $\text{Li}_2\text{S}_3$  with two diglyme molecules coordinating the lithium ions in vacuum

For the most optimized plane-wave calculations, we chose to use a wave function cutoff energy of 30 eV, a box size of 40, and 10000 self-consistent iterations to generate a spectra for the system of  $\text{Li}_2\text{S}_3$  with two diglymes, it represents the best computational results we can obtain at the current level of theory that uses PBE generalized-gradient approximation to approximate the exchange-correlation potential.

We re-evaluated the basis sets at this level of theory. Figure 4.8 (a) indicates no convergence of the spectra with the selected set of basis sets in Gaussian calculations, and they do not match the plane-wave result. In Figure 4.8 (b), augmentation is added for the cc-pVDZ basis set, the convergence at mini-augmented cc-pVDZ and the matching of the line shape in the resulting spectra to that from plane-wave method indicates that augmentation in the basis set for Gaussian calculations is needed. Surprisingly, we could not compute the spectra for this system using a larger basis set such as mini-augmented cc-pVTZ with Gaussian calculations due to its parallel inefficiency. Comparing Figure 4.8(a) and 4.8(b), the position shift between the spectra calculated from the two methods is probably due to the insufficient basis set used in Gaussian calculations. Therefore we should use a parallel efficient method like plane-wave method to calculate the optical spectra for solvated lithium polysulfides.

Combining all results above, we need a functional of cam-b3lyp or higher, an explicit solvent model (with more than 8 diglyme molecules per polysulfide), and a parallel efficient method, such as plane-wave calculations to compute reliable optical spectra for solvated lithium polysulfides, as shown in the schematic in Figure 4.9. In this case, all vacuum space is replaced with DMF molecules and the morphology is obtained from MD simulations as mentioned above.



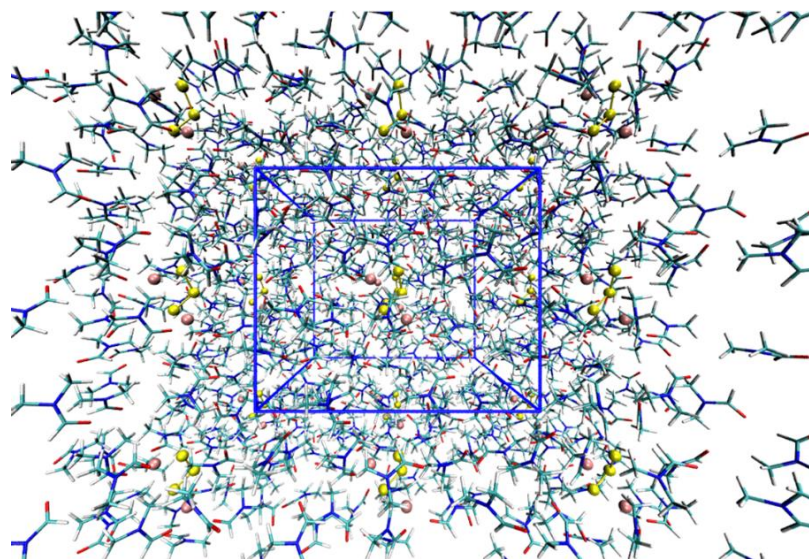


Figure 4.9. Schematic of infinitely repeating unit cells of  $\text{Li}_2\text{S}_3$  with 27 DMF molecules (approximately three solvation shells) simulated with first-principles molecular dynamics.

Unfortunately, current QUANTUM ESPRESSO suites for plane-wave calculations do not support a high level of theory equivalent to cam-b3lyp or higher. And should such a package being developed in the future, the work requires a large computational cost. Therefore we do not have the computational power to compute reliable optical spectra for condensed-phase solvated polysulfides in ether at the moment.

#### 4.4 Conclusions

We explored the necessary steps needed to reliably simulate optical spectra for solvated lithium polysulfides with LR-TDDFT calculations. A high level of functional to approximate the exchange-correlation function such as cam-b3lyp or higher is needed. Explicit solvent molecules are important for capturing the local solvent-solute interactions between polysulfides and ether solvents. We also compared the results using Gaussian orbitals and plane-wave basis sets and the results suggest that the two methods are comparable at their most optimized state. For a large system such as lithium polysulfides with explicit ether solvents, plane-wave calculations are efficient at achieving numerical convergence. We currently lack the computational power to calculate reliable optical spectra for such a large condensed-phase system.

#### 4.5 Acknowledgements

This work is supported by the Assistant Secretary for Energy Efficiency and Renewable Energy, Office of Vehicle Technologies of the US Department of Energy under Contract DE-AC02-05CH11231 under the Battery Materials Research Program. Computational work is performed at Lawrence Berkeley National Laboratory as part of a user project at the Molecular Foundry under the same Contract.

## 4.6 Supporting Information

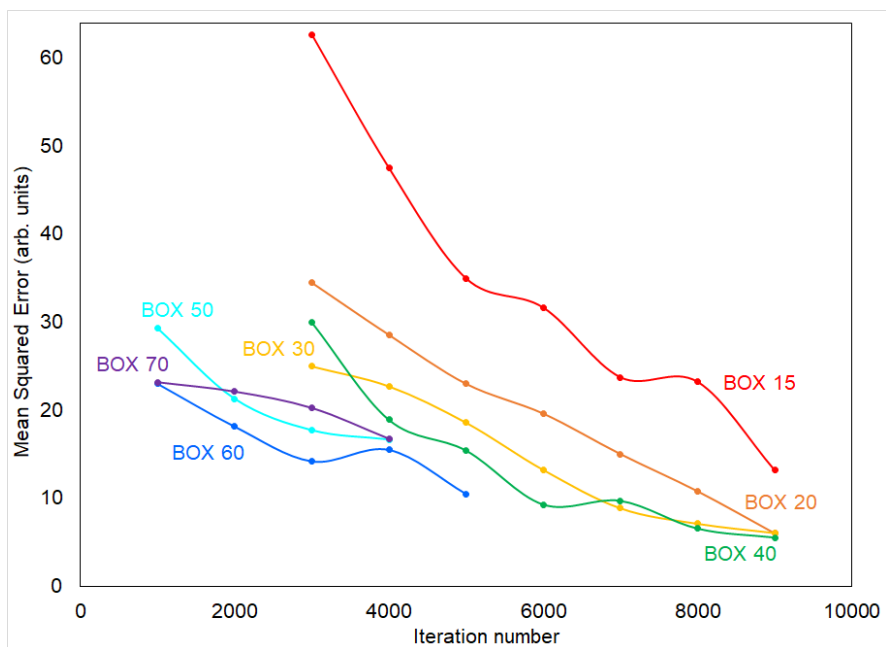


Figure S4.1. Mean Squared Error vs Iteration number for different box sized, calculated with respect to iteration number of 10000, all calculated with a wave function cut off energy of 30 eV.

## Chapter 5. Discharge Mechanism in a Solid-State Lithium-Sulfur Cell by Operando X-ray Absorption Spectroscopy<sup>†</sup>

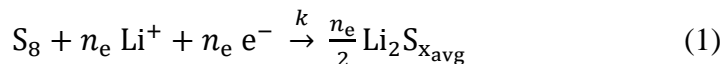
### ABSTRACT

The reduction of sulfur during discharge in a lithium-sulfur (Li-S) cell is known to occur in a series of reaction steps that involve lithium polysulfide intermediates. We present an operando study of the discharge of a solid-state Li-S cell using X-ray absorption spectroscopy (XAS). In theory, the average chain length of the polysulfides,  $x_{\text{avg,cell}}$ , at a given depth of discharge is determined by the number of electrons delivered to the sulfur cathode. The dependence of  $x_{\text{avg,cell}}$  measured by XAS on the depth of discharge is in excellent agreement with theoretical predictions. XAS is also used to track the formation of  $\text{Li}_2\text{S}$ , the final discharge product, as a function of depth of discharge. The XAS measurements were used to estimate rate constants of a series of simple reactions commonly accepted in literature. While the overall rate of reaction in the cathode is controlled by the current used to discharge the cell, the relative rate constants are not controlled by the current. To our knowledge, this work presents the first estimate of rate constants for discharge reactions in Li-S cells.

### 5.1 Introduction

Lithium-sulfur (Li-S) batteries have been considered as attractive alternative to current Li-ion batteries due to their large theoretical capacity (1672 mAh/g) and theoretical energy density (2600 Wh/kg). Sulfur is a particularly attractive cathode material for large format cells because it is cheap and abundant.<sup>1-4</sup> While there are numerous practical problems that have prevented the commercialization of rechargeable Li-S batteries, a significant barrier is the lack of understanding of the reaction mechanism that underlies this chemistry.<sup>5-10</sup> The redox reactions in the sulfur cathode occur in steps.<sup>11</sup> Some of the products in these steps are soluble lithium polysulfides intermediates.<sup>12-14</sup> The chemical formulae of lithium polysulfides are generally expressed as  $\text{Li}_2\text{S}_x$  where  $x$ , the length of the sulfur chain in the polysulfide is generally assumed to be between 2 and 8.<sup>15</sup> The dissolution of these species into the electrolyte is one of the primary problems that must be overcome before rechargeable Li-S batteries are commercialized. It also interferes with fundamental studies of redox reactions in the sulfur cathode.

The discharge reaction in the sulfur cathode of a Li-S cell can be written as equation (1).



We define  $n_e$  as the moles of electrons delivered to the sulfur cathode per mole of  $\text{S}_8$  in the cathode. The discharge reaction is complete when  $n_e = 16$  and the only product in the cathode is  $\text{Li}_2\text{S}$ . Our interest is to determine the state of the cathode during the intermediate steps of the discharge process. It is well known that numerous partially reduced sulfur species exist in the

---

<sup>†</sup> This work is submitted to *J. Electrochem. Soc.*

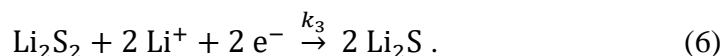
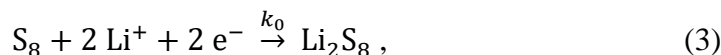


cathode during these intermediate steps. Despite these complexities, equation (1) must hold. In other words, the distribution of polysulfides obtained at a particular value of  $n_e$  must be such that the average chain length of the polysulfides,  $x_{\text{avg}}$ , is given by equation (2), which arises due to mole balance of sulfur in equation (1).

$$x_{\text{avg}} = \frac{16}{n_e} \quad (2)$$

To our knowledge, the validity of equation (2) has not been experimentally established.

Many reactions have been proposed<sup>11</sup> for the stepwise reduction of sulfur. We begin our discussion with a simple series of steps given below:



In the simplest case, the overall sulfur reduction reaction rate is governed by the discharge rate imposed on the Li-S cell. This will be true if effects such as transport limitations in the electrolyte and blocking of electrode surfaces due to insulating products are negligible. The discharge rate is typically expressed as  $C/\square$  where  $\square$  is the number of hours required to fully discharge the cathode. The overall rate of the discharge reaction is controlled by  $dn_e/dt$ , which is held constant during a galvanostatic discharge. If we start with a sulfur cathode containing  $m$  grams of sulfur (0.171 mg), and discharge it with a current,  $i$  in mA (0.0143 mA), then  $n_e$  at a given time,  $t$  in hours, is given by equation (7).

$$n_e = \frac{16it}{1672m} \quad (7)$$

where we have used the fact that the theoretical capacity of the sulfur cathode is 1672 mAh per g of sulfur.

The electrons delivered by the potentiostat to the cathode participate in all of the reactions (3)-(6). The distribution of polysulfides in the cathode at time  $t$  will be determined by the relative rate constants,  $k_0/k_1$ ,  $k_2/k_1$ , and  $k_3/k_1$ . (Our use of  $k_1$  to normalize rate constants will be made clear shortly.) Our objective is to estimate some of the relative rate constants that characterize reactions in a model sulfur cathode.

In the past decade, different techniques have been used to study the reaction mechanism in Li-S cells. Each technique has its own advantages and limitations.<sup>9,11</sup> Electrochemical measurements such as cyclic voltammetry (CV)<sup>16,17</sup> and rotating-ring disk electrode (RRDE)<sup>18</sup> are powerful approaches for determining the state of discharge but lack of the ability to distinguish different

reaction products. X-ray diffraction (XRD) can be used to detect the presence of crystalline species such as  $\text{Li}_2\text{S}$  and  $\text{S}_8$  but it is insensitive to the presence of amorphous polysulfides.<sup>19,20</sup> UV-vis,<sup>21–23</sup> Raman,<sup>24,25</sup> NMR<sup>26,27</sup> and X-ray absorption spectroscopy (XAS)<sup>28–39</sup> can, in principal be used to detect polysulfides. In references 20–38, measured spectra are used to infer the presence of certain specific polysulfide species. Such inferences rely on spectral signatures of pure polysulfides. Unfortunately there is no consensus on how polysulfides might be purified nor is there consensus on unique spectral fingerprints of different polysulfides.

In this paper, we present results of an operando XAS study of a solid-state Li-S cell. Our measurements enable independent measurements of  $x_{\text{avg}}$  and  $n_e$ , thereby enabling a test of the validity of equation (2). The XAS data also enable determination of the moles of  $\text{Li}_2\text{S}$  formed during discharge. These measurements enable determination of relative rate constants that characterize sulfur oxidation in the cathode,  $k_2/k_1$  and  $k_3/k_1$ .

## 5.2 Experimental Section

The separator/electrolyte and cathode were stored inside an argon-filled glove box (MBraun) with  $\text{H}_2\text{O}$  and  $\text{O}_2$  concentrations maintained at less than 0.1 ppm. Cell assembly was performed inside the same glovebox.

**Separator/electrolyte film preparation.** The separator/electrolyte films were prepared using a block copolymer of polystyrene-b-poly(ethylene oxide) (SEO) synthesized using methods described in the work by Hadjichristidis et al.<sup>40</sup> and purified using methods described in the work by Teran et al.<sup>41</sup> The molecular weights of polystyrene and poly(ethylene oxide) are 200 kg/mol and 222 kg/mol, respectively. Lithium perchlorate ( $\text{LiClO}_4$ , Sigma-Aldrich) was dried for 24 hours under vacuum at  $90^\circ\text{C}$  before use. The separator/electrolyte films containing SEO and  $\text{LiClO}_4$  were prepared according to the method described in the work by Wujcik et al.<sup>42</sup> The thickness of separator/electrolyte film used was 22  $\mu\text{m}$ .

**Cathode preparation.** Cathode slurries containing  $\text{S}_8$  (Alfa Aesar),  $\text{Li}_2\text{S}$  (Sigma-Aldrich) carbon black (Denka),  $\text{LiClO}_4$ , and SEO (identical  $\text{LiClO}_4/\text{SEO}$  composition to that of the electrolyte separator) was mixed in n-methylpyrrolidone (NMP). The slurry was composed of 89 wt% of NMP.  $\text{S}_8$  and  $\text{Li}_2\text{S}$  were mixed in a 256:46 weight ratio to produce  $\text{Li}_2\text{S}_x$  with an average  $x$  value of 8 as the starting material. Due to the insulating properties, both ionic and electronic, of  $\text{S}_8$ ,  $\text{Li}_2\text{S}_8$  was used as the starting material in order to ensure better contact between the active material, the electrolyte and carbon black. The slurry was mixed overnight at  $90^\circ\text{C}$  and subsequently mixed using a homogenizer (Polytron) set to 15,000 RPM. Homogenization was done for five minutes and repeated three times, with two minute rests between each cycle to prevent the solution from heating up to undesirable temperatures. The resulting slurry was then casted onto an 18  $\mu\text{m}$  thick aluminum foil current collector using a doctor blade. The film was dried under Argon at  $60^\circ\text{C}$  for 10 hours and then placed under static vacuum overnight at room temperature. The resulting cathode had an average thickness of 16  $\mu\text{m}$ , with the resulting composition: 12.8 wt%  $\text{Li}_2\text{S}_8$ , 51.4 wt% SEO, 5.5 wt%  $\text{LiClO}_4$ , and 30.3 wt% carbon.

**Cell Assembly and Cycling.** A pouch cell was prepared according to the method described in the work by Wujcik et al.<sup>37</sup> The assembled and sealed Li-S pouch cell was kept at rest at room temperature in an argon environment for 48 hours before taking measurements. The cell was then taken out of the argon-filled glovebox and placed on a sample holder connected to a heating source. It was then held at a temperature of 90°C for 1.5 hours allowing the development of cathode/electrolyte and anode/electrolyte interfaces. The cell was charged to partially form S<sub>8</sub>, and then discharged at 90°C at a C/20 rate using a VMP3 Potentiostat (Bio-Logic). Figure 1 shows a schematic of the assembled cell. The discharge and charge rate was calculated using the measured mass of the cathode electrode, the known weight percent of sulfur in the cathode, and assuming a theoretical capacity of 1672 mA-h/g for sulfur. The voltage window was kept between 1.5 V and 3.0 V.

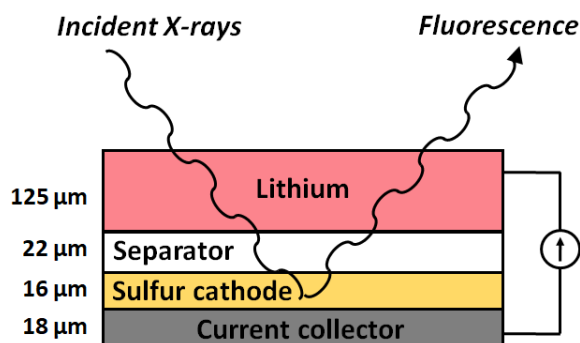


Figure 1. Schematic of a Li-S cell used for operando XAS study

**X-ray absorption spectroscopy.** XAS measurements were performed at beamline 4-3 of the Stanford Synchrotron Radiation Lightsource. Preliminary XAS experiments were performed at beamline 5.3.1 of the Advanced Light Source. Measurements were taken in fluorescence mode using a four element Vortex detector, with 0.1 eV energy resolution around the absorption K-edge. One scan took roughly 10 minutes to collect, equivalent to roughly 13.9 mA-h/g of capacity passed per scan. The beam spot size was 2 mm<sup>2</sup> and was not moved during cycling. The cell holder was inside a helium-filled chamber during the in operando measurements. Calibration of the X-ray energy was performed using sodium thiosulfate (Sigma-Aldrich), setting the first peak maximum to 2472.02 eV.

**XAS Spectra Analysis.** All spectra were analyzed using the Athena X-ray absorption spectroscopy program. Raw XAS spectra were used to calculate the “total sulfur” intensity based on methods described by our previous work.<sup>42</sup> For peak deconvolution and product analysis, all spectra were normalized and self-absorption corrected using the Athena XAS analysis package. The initial spectra were fitted with 4 Gaussian peaks and a step function. After 50 mAh/g the spectra were fitted with 6 Gaussians to account for the increasing skewness in the main-edge peak due to blue shift of the main-edge peak for mid-chain and short-chain polysulfides. Example of fitting an experimental spectra with 6 Gaussian peaks and a step function is shown in Figure S5.1.

## 5.3 Results and Discussion

### 5.3.1 Theoretical XAS spectra analysis

Theoretical XAS spectra for different lithium polysulfides were presented by Pascal et al. in a previous publication,<sup>42</sup> and the results are summarized in Figure 5.1(a). In the inset of Figure 5.1(a), we show a typical molecular conformation of one of the polysulfides,  $\text{Li}_2\text{S}_8$ . Polysulfides with chain length between 3 and 8 have two charged terminal sulfurs and the remainder of the internal sulfurs are uncharged. The two kinds of sulfurs give rise to two distinctive XAS features: a pre-edge peak corresponding to the two charged end-chain sulfurs and a main-edge peak corresponding to the internal sulfurs. The area under the theoretical pre-edge peak of each polysulfide is denoted by  $A_p^{\text{Th}}$ . Similarly the area under the theoretical main-edge peak of each polysulfide is denoted by  $A_m^{\text{Th}}$ . The spectral features of the polysulfides are approximated as a sum of Gaussian peaks and the areas under selected peaks were used to compute  $A_p^{\text{Th}}$  and  $A_m^{\text{Th}}$  as outlined in Figure S5.2. In Figure 5.1(b) we plot the ratio,  $A_m^{\text{Th}}/A_p^{\text{Th}}$ , as a function of polysulfide chain length,  $x$  in  $\text{Li}_2\text{S}_x$  ( $3 \leq x \leq 8$ ). The line in Figure 5.1(b) is a least squares linear fit. We use this linear fit as a “calibration” to determine the average chain length of polysulfides in our cell,  $x_{\text{avg}}$ , using measured values of pre-edge and main-edge areas,  $A_p$  and  $A_m$ . The straight line in Figure 5.1(b) can be represented as

$$x = 0.8732 A_m/A_p + 1.9326. \quad (8)$$

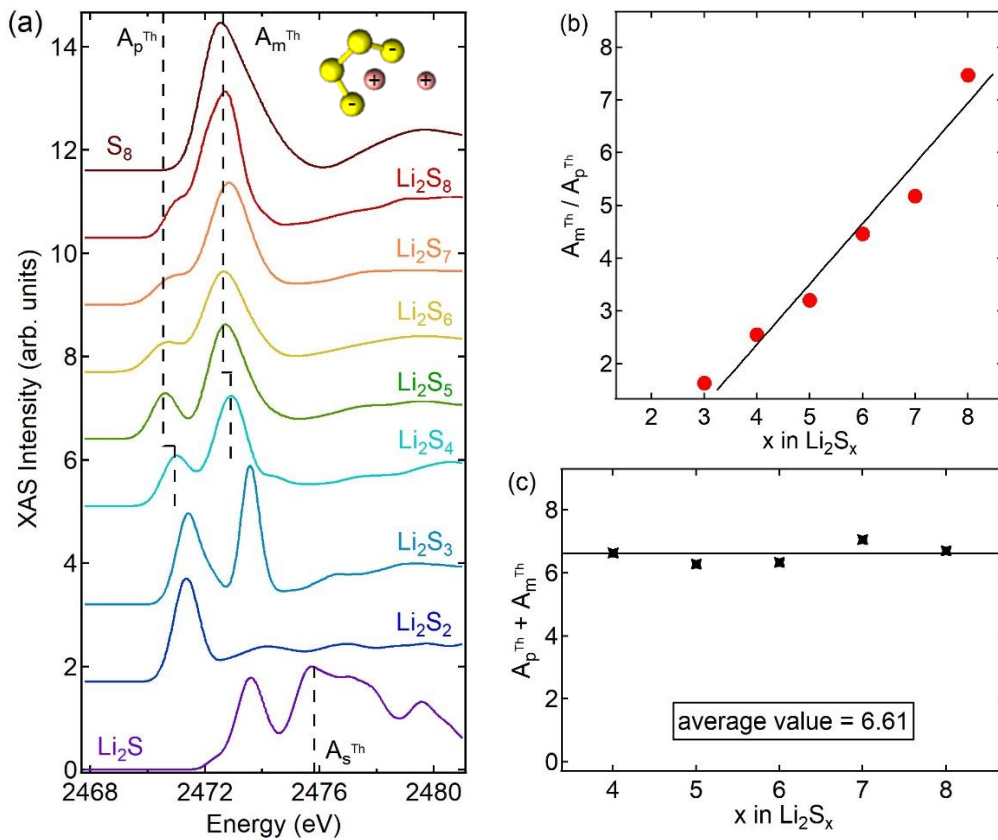
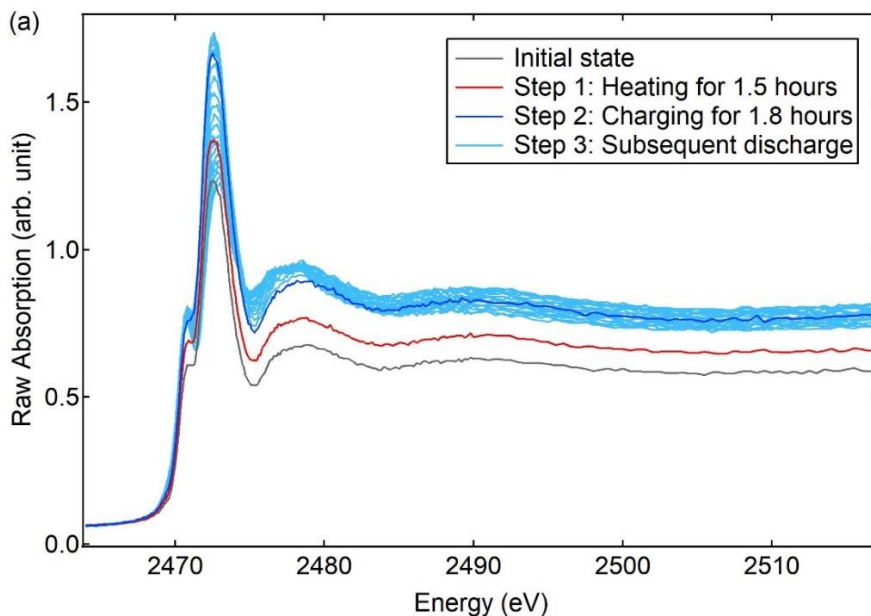


Figure 5.1. (a) Theoretical XAS spectra from Pascal et al.<sup>42</sup>, (b) linear relationship between  $x$  for  $\text{Li}_2\text{S}_x$  ( $3 \leq x \leq 8$ ) and the area ratio of main-edge peak to pre-edge peak,  $A_m/A_p$ , and (c) sum of pre-edge and main-edge peak areas per mole of  $\text{Li}_2\text{S}_x$  ( $4 \leq x \leq 8$ ) from theoretical spectra

In Figure 5.1(c) we plot the sum,  $(A_p^{\text{Th}} + A_m^{\text{Th}})$ , as a function of  $x$  in  $\text{Li}_2\text{S}_x$  ( $4 \leq x \leq 8$ ). To a good approximation,  $(A_p^{\text{Th}} + A_m^{\text{Th}})$  is 6.61, independent of  $x$ . The theoretical spectrum of  $\text{Li}_2\text{S}$  contains a unique peak at 2476 eV that is not present in any of the polysulfidies. The area under this peak,  $A_s^{\text{Th}}$ , was calculated by approximating the theoretical  $\text{Li}_2\text{S}$  spectrum by a sum of Gaussian peaks as shown in Figure S5.3. The value of  $A_s^{\text{Th}}$  is 3.07. We use this to estimate the moles of  $\text{Li}_2\text{S}$ . In our cell is determined by estimating the area under the peak at 2476 eV,  $A_s$ .

### 5.3.2 Total Sulfur signal

The XAS cell was made with  $\text{Li}_2\text{S}_8$  in the cathode. Our use of  $\text{Li}_2\text{S}_8$  facilitated dispersion of the sulfur species in the cathode. Our main objective is to determine the state of the sulfur-containing cathode as the cell is discharged. We used a relatively thin cathode and adjusted the sulfur content in the cathode to ensure that all of the sulfur-containing species in the cell could be detected by XAS. The cell was placed in the XAS sample stage, heated to 90 °C for 1.5 h, charged at C/20 until the voltage reached 3.0 V, and then discharged at C/20. Figure 5.2(a) shows all of the raw XAS spectra during these experiments. The magnitude of the high energy plateau attained between 2500 and 2575 eV is indicative of the total amount of sulfur detected. We define  $I_0$  to be the average value of the raw XAS signal between 2500 and 2575 eV obtained just prior to discharge. We define  $I_n$  as the average value of the raw XAS signal in the same energy range obtained during other scans. The time dependence of the cell potential during these experiments is shown in Figure 5.2(b). The corresponding values of  $I_n/I_0$  versus time shows are shown in Figure 5.2(c).



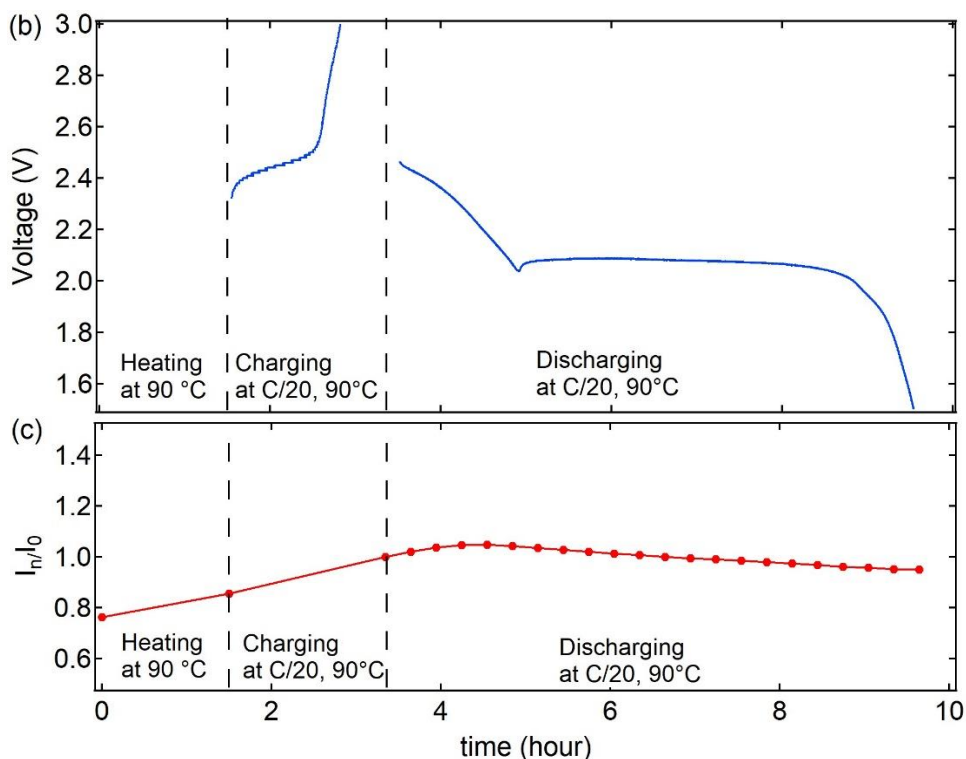


Figure 5.2. (a) All raw XAS spectra, (b) time dependence of voltage and (c) time dependence of  $I_n/I_0$  before and during cycling

If our cell was perfectly designed, then  $I_n/I_0$  would be independent of time. In our case,  $I_n/I_0$  increased by about 12% during the heating step, and increased by about another 16% during the charging step. During the discharge step, however,  $I_n/I_0$  remained approximately constant, varying between 1.05 and 0.95. The constancy of  $I_n/I_0$  during discharge indicates that all (or nearly all) of the products of sulfur reduction were detected by XAS experiment.

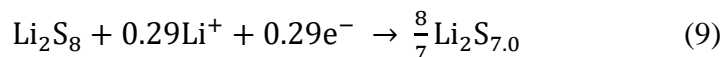
### 5.3.3 Discharge products from spectra

The raw spectra shown in Figure 5.2(a) were normalized and corrected for self-absorption. All of the normalized spectra exhibited a pre-edge peak around 2471 eV and a main-edge peak around 2473 eV. This enables calculation of the areas under the pre-edge,  $A_p$ , and main-edge peak,  $A_m$ . These areas can be used to determine the average polysulfide chain length in the cell,  $x_{\text{avg,cell}}$  ( $x$  for  $\text{Li}_2\text{S}_x$ ), using equation (8). After the heating step,  $x_{\text{avg,cell}}$  equals 7.0. After the charging step,  $x_{\text{avg,cell}}$  reached 8.1.

An ideal cell would be one wherein all of the  $\text{Li}_2\text{S}_8$  in the cathode remained in the cathode after the heating step, and at the end of discharge, all of the  $\text{Li}_2\text{S}_8$  would have been converted to  $\text{S}_8$ . In other words,  $x_{\text{avg,cell}}$  would equal 8.0 in the ideal cell after the heating step, and  $x_{\text{avg,cell}}$  would equal infinity after the charging step. It is evident that our cell is far from ideal. The observed departure from ideality after the heating step is attributed to the dissolution of  $\text{Li}_2\text{S}_8$  into the separator,

subsequent reactions with the lithium metal anode, and shuttling of the resulting shorter polysulfides back into the cathode.

About 0.29 moles of Li per mole of S<sub>8</sub> was reacted to bring the average chain length from 8 to 7.0 during the 48 hours rest at room temperature according to equation (9).



The cell was then charged at a C/20 rate. The average chain length increased to 8.1 after charging indicating some remaining polysulfides (likely Li<sub>2</sub>S<sub>8</sub>) inside the cathode was converted to S<sub>8</sub>. The charging time corresponds to  $n_e = 1$ , 1 moles of electron delivered to the cathode per mole of S<sub>8</sub>, but the conversion of  $x_{\text{avg,cell}} = 7.0$  to  $x_{\text{avg,cell}} = 8.1$  corresponds to a transfer of 0.27 moles of electrons per mole of S<sub>8</sub>. The significant inefficiency in charging (27%) mainly comes from the shuttling effect. For an ideal charge, lithium ions are stripped from the cathode, move through the separator, combines with an electron in the anode and gets deposited onto the anode as lithium metal. In our Li-S cell, lithium ions arriving at the anode side can further reduce the long chain polysulfides at the anode/separators interface into short-chain polysulfides with additional electrons coming from the anode. This is the main reason prevents Li-S cells from fully charged.

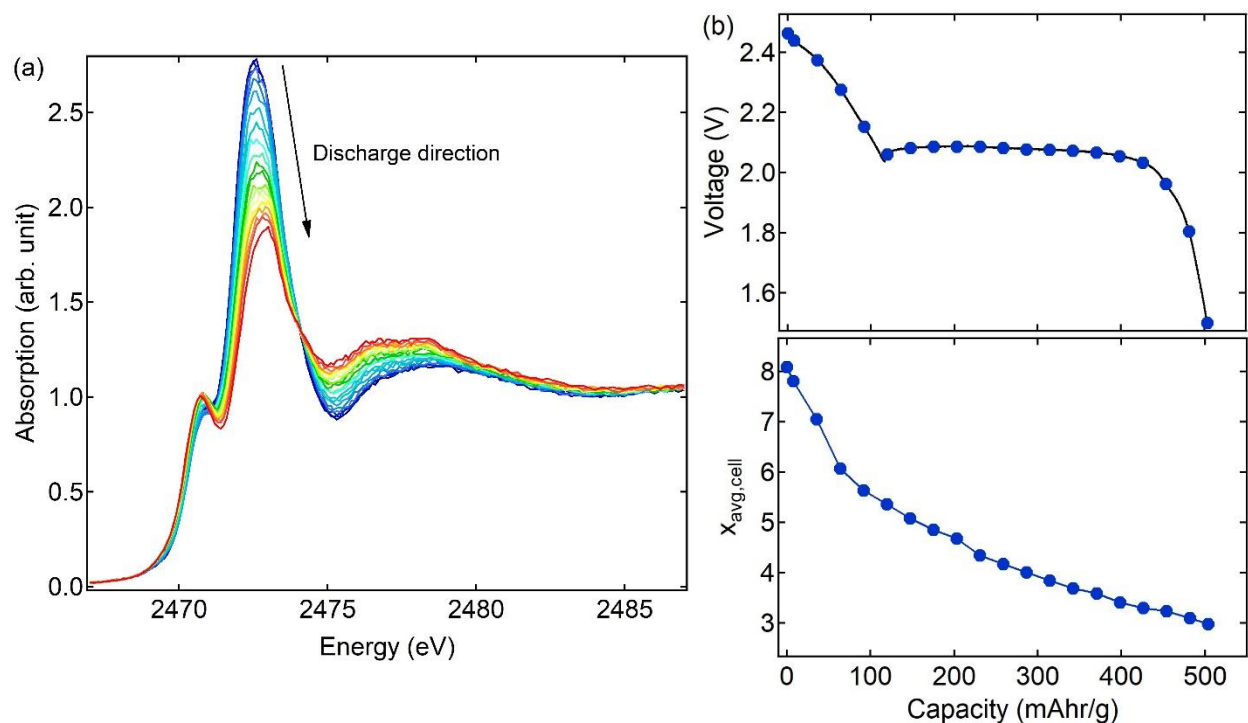


Figure 5.3(a) Normalized and self-absorption corrected in operando XAS spectra and (b) voltage profile and average polysulfide chain length during discharge

Figure 5.3(a) shows selected in operando spectra with normalization and self-absorption correction during discharge. Figure 5.3(b) shows the discharge profile and the calculated average chain length during discharge. A low discharge capacity of 503.25 mA-h/g is likely due to slow charge transfer in a block copolymer electrolyte. Using the peak ratio analysis we calculated the



average chain-length throughout discharge where  $x_{\text{avg,cell}}$  dropped monotonically from 8.1 at the beginning of discharge to 3.0 at the end of discharge. This corresponds to  $n_e = 3.36$ , slightly lower than the actual value, 4.82 moles of electrons per mole of  $S_8$  transferred, calculated from the discharge capacity (The theoretical capacity value of 1672 mA-h/g would correspond to  $n_e = 16$ ). The discrepancy (72% discharge efficiency) could be due to the lack of ability of the peak ratio analysis to capture very short chain polysulfides such as  $Li_2S$  and  $Li_2S_2$  because the ratio analysis is limited to polysulfides with chain length of 3 or longer (Figure 5.1a). Note that where the decrease in  $x_{\text{avg,cell}}$  values slows down coincides with the end of the high voltage plateau, indicating a fundamental change in reaction mechanism. The high voltage plateau is likely due to the conversion of solid state  $S_8$  to liquid state long-chain polysulfides ( $Li_2S_8$ ,  $Li_2S_7$ ,  $Li_2S_6$ ), and the reaction is fast due to the high solubility of these long-chain polysulfides.<sup>43</sup> Post high-voltage plateau region corresponds to the conversion of longer-chain polysulfides to mid-chain and short-chain polysulfides, and these reactions are slower due to the products' lower solubility in an ether-based electrolyte.<sup>43</sup> It is worth mentioning that we did not observe a significant amount of radicals forming during discharge from the lack of peak features at lower energy range ( $\sim 2468$  eV<sup>42</sup>).

Based on the simulated spectra in Figure 5.1(a), solid-phase  $Li_2S$  has unique absorption peaks at 2474 eV and 2476 eV due to its crystal bonding structure compared to amorphous polysulfide. In literature people have been using these two peaks to identify the formation of  $Li_2S$ .<sup>27,30,44,45</sup> However since polysulfides ( $Li_2S_x$ ,  $2 \leq x \leq 8$ ) main-edge peaks around 2472.7 eV are broad which will be affected by any signal at 2474 eV, we therefore use the peak at 2476 eV,  $A_s$ , to quantify the formation of  $Li_2S$ . Figure 5.4 is a discharged spectrum illustrating the locations of  $A_p$ ,  $A_m$ , and  $A_s$ .

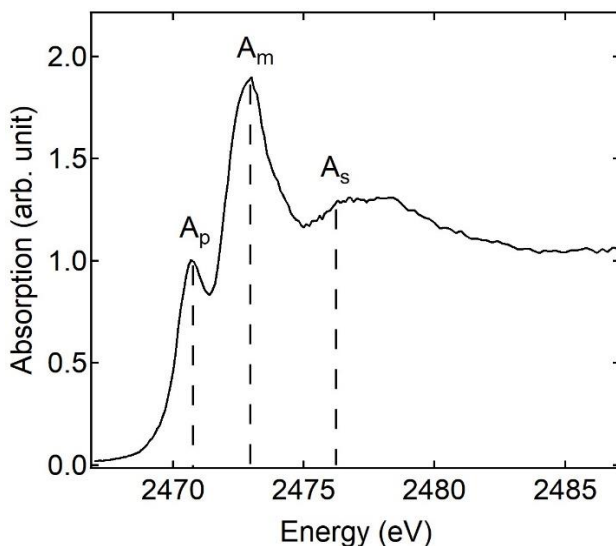


Figure 5.4. Illustration of peaks with areas  $A_p$ ,  $A_m$ , and  $A_s$  for a discharged spectrum

From theoretical spectra analysis in Figure 5.1, the sum of pre-edge and main-edge peaks, ( $A_p + A_m$ ), stays roughly constant for 1 mole of polysulfides across different  $x$  values. We also fitted Gaussian peaks to the theoretical  $Li_2S$  spectra to obtain the area under the 2476 eV peak,  $A_s^{\text{Th}}$ . The



ratio of the theoretical spectra peak areas,  $\frac{A_s^{\text{Th}}}{A_p^{\text{Th}}+A_m^{\text{Th}}} = C_s$ , is a calibration constant indicating that for 1 mole of  $\text{Li}_2\text{S}$  formed per mole of polysulfides, we will get a peak ratio  $\frac{A_s}{A_p+A_m}$  equals to  $C_s$ .  $\text{Li}_2\text{S}$  is not considered as a polysulfide here. Therefore, we can calculate  $m_{\text{Li}_2\text{S}}$ , moles of  $\text{Li}_2\text{S}$  formed per mole of polysulfides during discharge, from the ratio  $\frac{A_s}{A_p+A_m}$  obtained from the experimental spectra:  $m_{\text{Li}_2\text{S}} = \frac{A_s}{A_p+A_m} / C_s$ . Figure 5.5 plots  $\frac{A_s}{A_p+A_m}$  on the left axis and  $m_{\text{Li}_2\text{S}}$ , on the right axis versus discharge capacity.

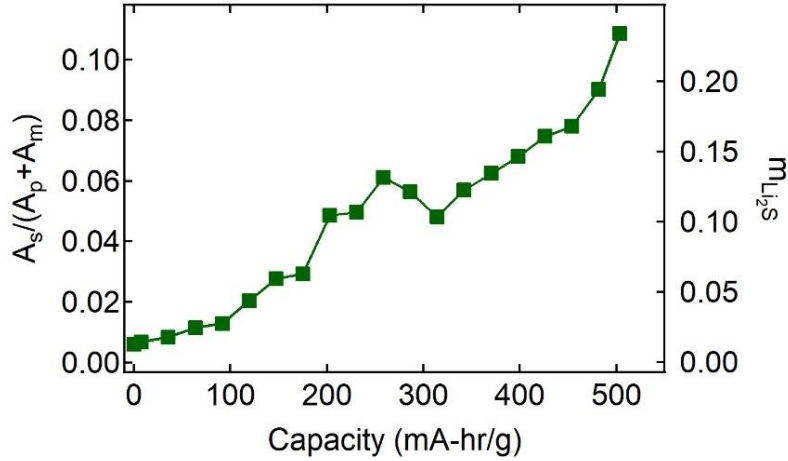


Figure 5.5. Ratio of 2476 eV peak,  $A_s$ , to sum of peak areas for pre-edge and main-edge,  $A_p + A_m$ , on the left axis and moles of  $\text{Li}_2\text{S}$  formed per mole of polysulfides,  $m_{\text{Li}_2\text{S}}$ , on the right axis versus discharge capacity

$m_{\text{Li}_2\text{S}}$  started at a low value and increases throughout discharge. The increase in  $m_{\text{Li}_2\text{S}}$  becomes significant from about 100 mA-hr/g, which is around the beginning of second plateau, suggests that  $\text{Li}_2\text{S}$  started to form at the beginning of the second voltage plateau. Ideally  $m_{\text{Li}_2\text{S}}$  should start at zero, but the arbitrary low value at the beginning of discharge is likely due to the limitation in spectra fitting. This finding of an early formation of crystalline  $\text{Li}_2\text{S}$  is consistent with those found by Waluś et al.<sup>18,124</sup>, Dominko et al.<sup>111</sup> and Conder et al.<sup>125</sup>, suggesting that the reaction mechanism of forming solid phase products is not successive, but rather, simultaneous with the formation of other mid-chain and short-chain polysulfides.  $m_{\text{Li}_2\text{S}}$  reached 0.233 at the end of discharge, corresponds to a molar ratio of approximately 1:4 for  $\text{Li}_2\text{S}$  to polysulfides. It is worth mention that recent studies suggest that  $\text{Li}_2\text{S}_2$  may be crystalline as well,<sup>73-75</sup> and should it form during discharge, may contribute to the higher energy absorption peaks as well.

### 5.3.4 Relating average discharge products to $n_e$

We want to further examine how the redox reduction species in our Li-S cell are related to the number of electrons passed during discharge. Figure 5.6 plots the theoretical and experimental  $X_{\text{avg,cell}}$  versus  $n_e$ .  $n_e$  is the moles of electrons delivered to the cathode per mole of  $\text{S}_8$ . The value of

$n_e$  should, in principal, equal to the value of moles of lithium delivered to the cathode per mole of  $S_8$ . The black curve represents equation (1), the theoretical case where  $x$  in  $Li_2S_x$  is reduced from infinity ( $S_8$ ) with no electrons passed per  $S_8$  (neutral) to 1 ( $Li_2S$ ) with 16 electrons passed per  $S_8$  molecule (each sulfur atom has a valence of 2-). The starting point of the experimental data is assumed to start from  $Li_2S_{8.09}$  ( $n_e = 1.98$ ).

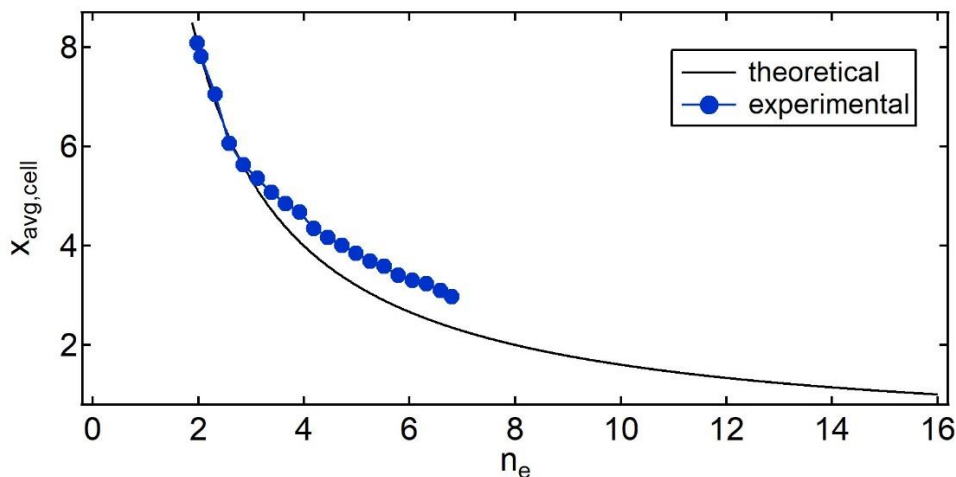


Figure 5.6. Theoretical and experimental average chain length,  $X_{avg,cell}$ , vs number of electrons delivered per  $S_8$  molecule,  $n_e$

There is a large discrepancy between the theoretical value and the experimental data. This discrepancy can be explained by the fact that sulfur-containing species inside the cathode are at a larger probing depth than sulfur-containing species dissolved into the separator. Because the anode side faces the incoming X-ray source as well as the detector, it is much easier for the fluorescence signal from sulfur species inside the separator to reach the detector than signal from sulfur species inside the cathode to be detected. And most of the polysulfides lost into the separator can no longer be electrochemically reduced due to a lack of electron supply from the cathode. These lost polysulfides mostly stayed as long-chain polysulfides,  $Li_2S_x$  ( $6 \leq x \leq 8$ ), has a higher solubility than mid-chain and short-chain polysulfides,<sup>43</sup> and therefore increases the overall detected  $X_{avg,cell}$  value especially at higher depth of discharge.

We therefore need to refine the theoretical model including the effect of lost polysulfides into the separator. We assumed that 10% of all sulfur atoms were lost into the separator in the form of polysulfides. We also assumed that these dissolved polysulfides stayed as a mixture of long-chain polysulfides during discharge with an average chain length of  $x_{avg,sep} = 6.97$ , the equilibrium chain length reached when the cell was at rest before cycling. To calculate the percentage of signal detected from the cathode and the separator, we assumed a simple model where all polysulfides in the separator has an average transmission equal to polysulfides at the middle of the separator layer and all sulfur-containing species in the cathode has an average transmission equal to species from the middle of the cathode layer. The transmission of sulfur-containing species from the middle of the separator layer and the middle of the cathode layer is about 62.3% and 39.8%, respectively, calculated using the known electrolyte and cathode composition with the method described in our

previous work.<sup>41</sup> Assuming 10% of sulfur-containing species are in the separator, we can calculate the percentage of detected signal coming from sulfur-containing species inside the electrolyte,  $D_{\text{sep}} = 14.8\%$ , and the percentage of signal coming from sulfur-containing species inside the cathode,  $D_{\text{cathode}} = 85.2\%$ . This allows us to separate the average products inside the cathode from the ones in the separator, and we can calculate the average chain length inside the cathode,  $X_{\text{avg,cathode}}$ , based on equation (10):

$$X_{\text{avg,cathode}} * D_{\text{cathode}} + X_{\text{avg,sep}} * D_{\text{sep}} = X_{\text{avg,cell}} \quad (10)$$

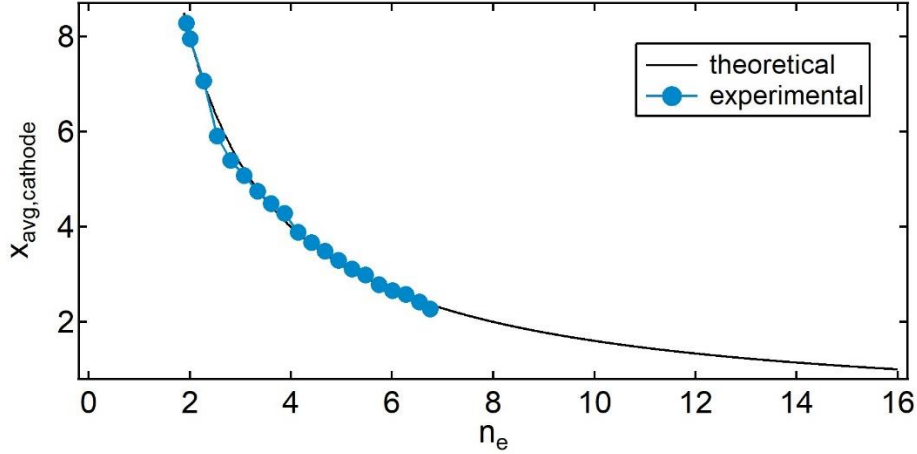


Figure 5.7. Theoretical and experimental average chain length inside the cathode,  $X_{\text{avg,cathode}}$ , vs number of electrons delivered per  $S_8$  molecule,  $n_e$

Figure 5.7 plots the theoretical and experimental  $X_{\text{avg,cathode}}$  versus  $n_e$ . The good agreement between theoretical model and experimental data suggest that our assumptions were good approximations of what happened in the cell, that before and during discharge, about 10% of sulfur-containing species dissolved into the separator and can no longer participate in electrochemical reactions due to lack of electron supply. The rest of the sulfur-containing species remained inside the cathode went through redox reactions and brought the average chain length from  $X_{\text{avg,cathode}} = 8.28$  to  $X_{\text{avg,cathode}} = 2.28$ .

We further decompose the products into polysulfides ( $\text{Li}_2\text{S}_x$ ,  $2 \leq x \leq 8$ ) with average chain length of  $X_{\text{avg,PS}}$  and  $\text{Li}_2\text{S}$  using  $m_{\text{Li}_2\text{S}}$  from Figure 5.5.  $X_{\text{avg,PS}}$  can be calculated with equation (11):

$$\text{Li}_2\text{S}_{X_{\text{avg,PS}}} + m_{\text{Li}_2\text{S}} \text{Li}_2\text{S} = (1 + m_{\text{Li}_2\text{S}})\text{Li}_2\text{S}_{X_{\text{avg,cathode}}} \quad (11)$$

Combining all information about polysulfides and  $\text{Li}_2\text{S}$  formed inside the cathode gives us insight of the reactions and species formed inside the cathode during discharge. Figure 5.8 plots  $X_{\text{avg,PS}}$  on the left axis and  $m_{\text{Li}_2\text{S}}$  on the right axis versus  $n_e$  during discharge.

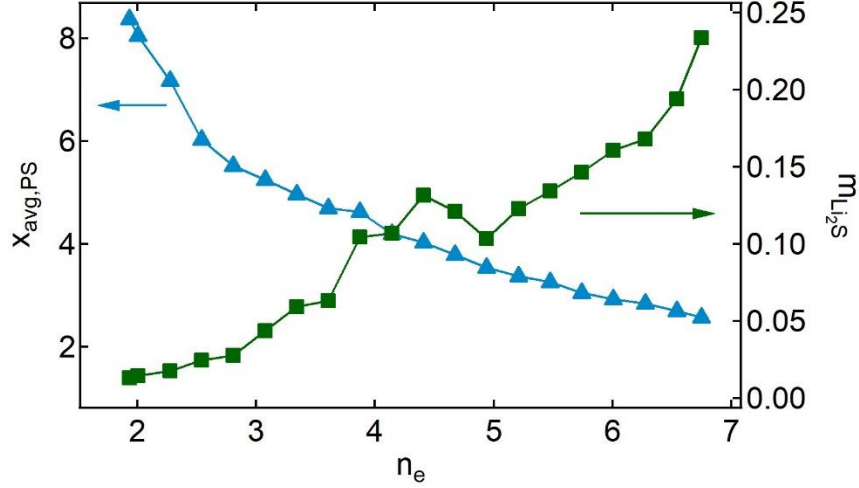
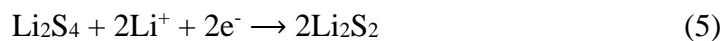
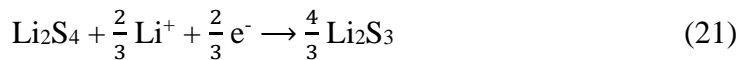
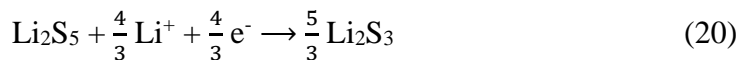
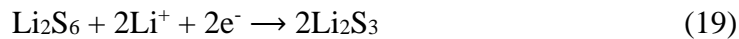
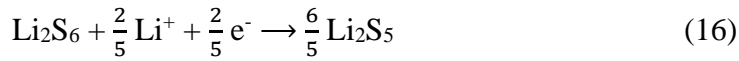
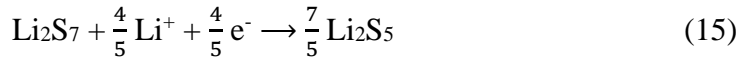
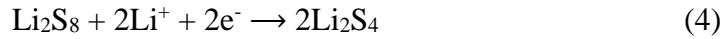
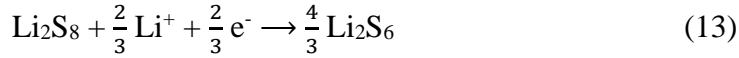
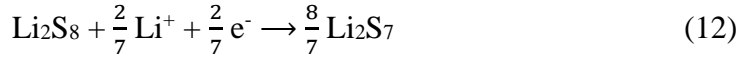
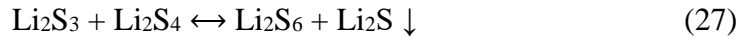
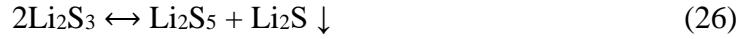
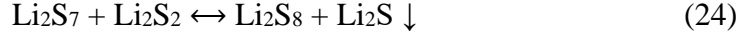
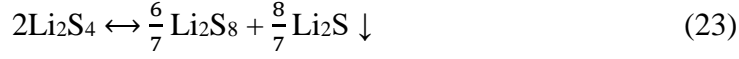
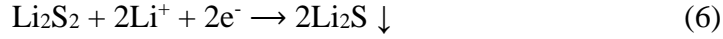
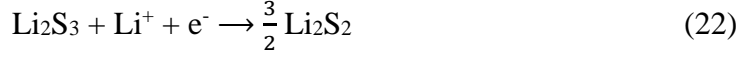


Figure 5.8. Average polysulfide chain length inside the cathode,  $X_{avg,PS}$ , on the left axis, and molar ratio of  $Li_2S$  to polysulfides,  $m_{Li_2S}$ , vs number of electrons delivered per  $S_8$  molecule,  $n_e$

Equations listed below are some of the discharge reactions that have been proposed in previous reports.<sup>15–17,32,46,51–57</sup>





Not all these reactions are equally likely to happen. For example, equation (13) requires the presence of 11 particles (7  $\text{Li}_2\text{S}_8$  molecules, 2  $\text{Li}^+$ , and 2  $\text{e}^-$ ) at one reaction site simultaneously. Such reactions are less likely to play a significant role in Li-S discharge. For simplicity, we pick equations (3)-(6) as a set of representative reactions to analyze our system. Since we started with almost  $\text{Li}_2\text{S}_8$ , we construct a simple model using equations (4)-(6) with reaction rates  $k_1$ ,  $k_2$ , and  $k_3$ . From the model we obtain equations (29)-(33):

$$\frac{dC_8}{dt} = -k_1 C_8 \quad (29)$$

$$\frac{dC_4}{dt} = 2 k_1 C_8 - k_2 C_4 \quad (30)$$

$$\frac{dC_2}{dt} = 2 k_2 C_4 - k_3 C_2 \quad (31)$$

$$\frac{dC_1}{dt} = 2 k_3 C_2 \quad (32)$$

$$\frac{dn_e}{dt} = -2 (k_1 C_8 + k_2 C_4 + k_3 C_2) \quad (33)$$

Where  $C_8$ ,  $C_4$ ,  $C_2$ ,  $C_1$  are the molar concentrations of  $\text{Li}_2\text{S}_8$ ,  $\text{Li}_2\text{S}_4$ ,  $\text{Li}_2\text{S}_2$ , and  $\text{Li}_2\text{S}$ , respectively. Equations (34)-(36) are the definitions of  $X_{\text{avg,cathode}}$ ,  $X_{\text{avg,PS}}$ , and  $m_{\text{Li}_2\text{S}}$  using the molar concentrations of the four species involved in the model.

$$X_{\text{avg,cathode}} = \frac{8 C_8 + 4 C_4 + 2 C_2 + C_1}{C_8 + C_4 + C_2 + C_1} \quad (34)$$

$$X_{\text{avg,PS}} = \frac{8 C_8 + 4 C_4 + 2 C_2}{C_8 + C_4 + C_2} \quad (35)$$

$$m_{\text{Li}_2\text{S}} = \frac{C_1}{C_8 + C_4 + C_2} \quad (36)$$

Equations (29)-(33) are solved by empirically fitting different values of  $k_1$ ,  $k_2$ , and  $k_3$ . The solved  $C_8$ ,  $C_4$ ,  $C_2$ ,  $C_1$  at each  $t$  are used to predict  $X_{\text{avg,cathode}}$ ,  $X_{\text{avg,PS}}$ ,  $m_{\text{Li}_2\text{S}}$ , and  $n_e$  at each  $t$ . Figure 5.9 (a)-(d) shows the experimentally measured and the model predicted values of  $X_{\text{avg,cathode}}$ ,  $X_{\text{avg,PS}}$ ,  $m_{\text{Li}_2\text{S}}$ , and  $n_e$ , respectively. The experimental values of  $m_{\text{Li}_2\text{S}}$  in were subtracted by a constant so that  $m_{\text{Li}_2\text{S}}$  at  $t = 0$  is zero.

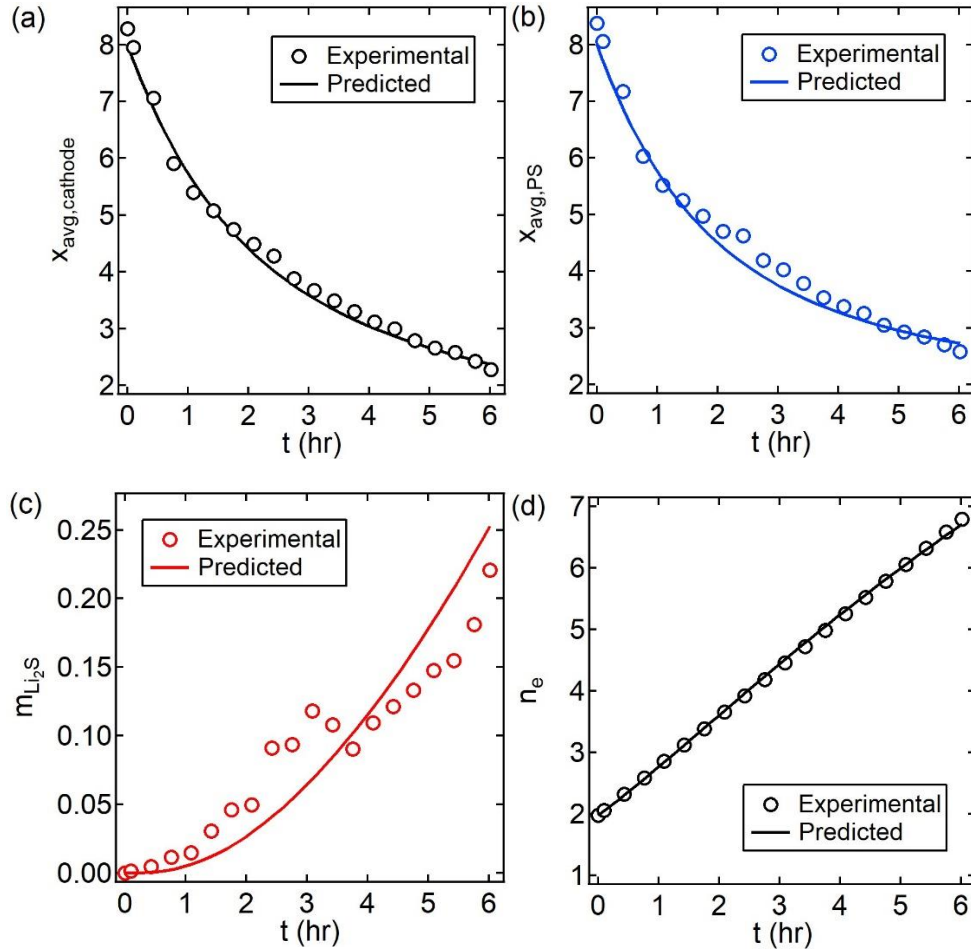


Figure 5.9. Comparing experimental measures and the predicted values of (a)  $X_{\text{avg,cathode}}$ , (b)  $X_{\text{avg,PS}}$ , (c)  $m_{\text{Li}_2\text{S}}$ , and (d)  $n_e$  versus  $t$ , time in hours, using the three-reaction model fitted with  $k_1 = e^{-1}$ ,  $k_2 = \frac{3}{4}e^{-1}$ , and  $k_3 = \frac{1}{6}e^{-1}$ .

By using a set of reaction constants,  $k_1 = e^{-1}$ ,  $k_2 = \frac{3}{4}e^{-1}$ , and  $k_3 = \frac{1}{6}e^{-1}$ , the values of  $X_{\text{avg,cathode}}$ ,  $X_{\text{avg,PS}}$ , and  $n_e$  fitted well in Figure 5.9(a), (b), and (d). The model under predicted the formation of  $\text{Li}_2\text{S}$  at first suggesting that other reactions mechanisms were involved in the production of  $\text{Li}_2\text{S}$  at an earlier discharge state such as those proposed in equations (23)-(28). The model predicts that the reduction of the longest-chain polysulfides ( $\text{Li}_2\text{S}_8$ ) into mid-chain polysulfides ( $\text{Li}_2\text{S}_4$ ) was the fastest. The reaction rate of reducing mid-chain polysulfides ( $\text{Li}_2\text{S}_4$ ) to short-chain polysulfides ( $\text{Li}_2\text{S}_2$ ) was 75% the rate of the previous reaction, and the rate of reducing short-chain polysulfides ( $\text{Li}_2\text{S}_2$ ) to  $\text{Li}_2\text{S}$  was much slower, approximately a fraction of  $\frac{1}{6}$  of the speed of the first reaction.

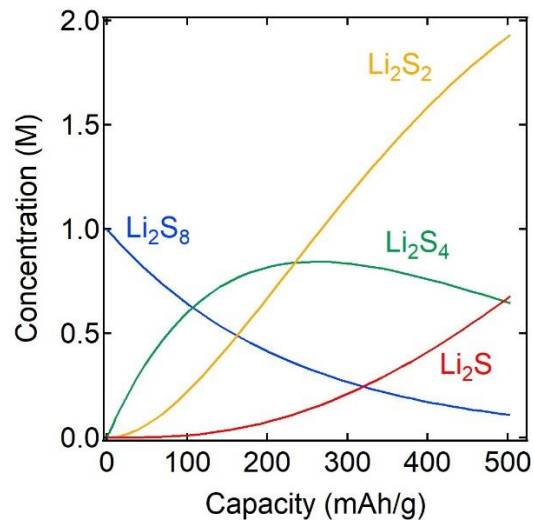


Figure 5.10 Concentration profile of  $\text{Li}_2\text{S}_8$ ,  $\text{Li}_2\text{S}_4$ ,  $\text{Li}_2\text{S}_2$ , and  $\text{Li}_2\text{S}$  predicted by model

Figure 5.10 plots the model predicted concentrations of  $\text{Li}_2\text{S}_8$ ,  $\text{Li}_2\text{S}_4$ ,  $\text{Li}_2\text{S}_2$ , and  $\text{Li}_2\text{S}$  versus discharge capacity. We acknowledge that this is an over-simplified model that in reality, the presence of other species and reactions will affect both the concentration profiles presented in Figure 5.10 as well as the rate constants presented in Figure 5.9.

## 5.4 Conclusion

In this work, we demonstrated a study where all sulfur-containing species through the entire depth of a Li-S cell were detected. With lithium facing the incoming X-ray and detector, we were able to avoid photon-transparent cathode substrate and make a cell with thin cathode and separator layers. Using a block copolymer electrolyte, we were able to construct a solid-state Li-S cell.  $\text{Li}_2\text{S}_8$  was used as active material inside cathode instead of  $\text{S}_8$  to provide better contact between the active materials and the solid electrolyte. In operando XAS spectra were taken before and throughout the charge-discharge cycle. Inefficiency in the initial charge revealed that lithium polysulfide dissolved into the separator layer reacted with lithium metal at the anode. The average value of polysulfide chain-length,  $x$  in  $\text{Li}_2\text{S}_x$ , were calculated using the peak ratio analysis method and a simple model assuming 10% of sulfur-containing species lost into the separator was used to fit the experimental data and separate the products inside the cathode. We explored the relationship between the average discharge polysulfide chain length inside the cathode,  $X_{\text{avg,cathode}}$ , and the number of electrons passed per S atom,  $n_e$ , at different stages of discharge. During the higher voltage plateau, while a small amount of  $\text{S}_8$  was converted to  $\text{Li}_2\text{S}_8$ , the major electrochemical reaction was the reduction of  $\text{Li}_2\text{S}_8$  to  $\text{Li}_2\text{S}_6$  (about 75%). During the transition region between the two plateaus,  $\text{Li}_2\text{S}_8$  continued to be reduced to  $\text{Li}_2\text{S}_6$  while almost half of  $\text{Li}_2\text{S}_6$  was reduced to  $\text{Li}_2\text{S}_4$ . Chemical reactions took place during these two stages did not affect our analysis based on  $X_{\text{avg,cathode}}$ . The longer lower voltage plateau is associated with the formation of  $\text{Li}_2\text{S}_2$  and  $\text{Li}_2\text{S}$  both electrochemically and chemically. The early formation of  $\text{Li}_2\text{S}$  in this region supports what have been reported in several literature that chemical disproportionation reactions play an important role in the formation of  $\text{Li}_2\text{S}$ . About 20% of sulfur-containing species were  $\text{Li}_2\text{S}$  at the end of discharge.

Due to the similarity in the peak locations for different lithium polysulfides, XAS may not be the best tool to differentiating different polysulfides produced during discharge. A spectroscopy with simple distinctive peaks for different polysulfides and well-established spectra standards would be better for Li-S reaction mechanism study.

## 5.5 Acknowledgements

This work was supported by the Assistant Secretary for Energy Efficiency and Renewable Energy, Office of Vehicle Technologies of the US Department of Energy under Contract DE-AC02-05CH11231 under the Battery Materials Research program. Use of the Stanford Synchrotron Radiation Lightsource, SLAC National Accelerator Laboratory, is supported by the U.S. Department of Energy, Office of Science, Office of Basic Energy Sciences under Contract No. DEAC02-76SF00515. The Advanced Light Source is supported by the Director, Office of Science, Office of Basic Energy Sciences, of the U.S. Department of Energy under Contract No. DE-AC02-05CH11231.



## 5.6 Supporting Information

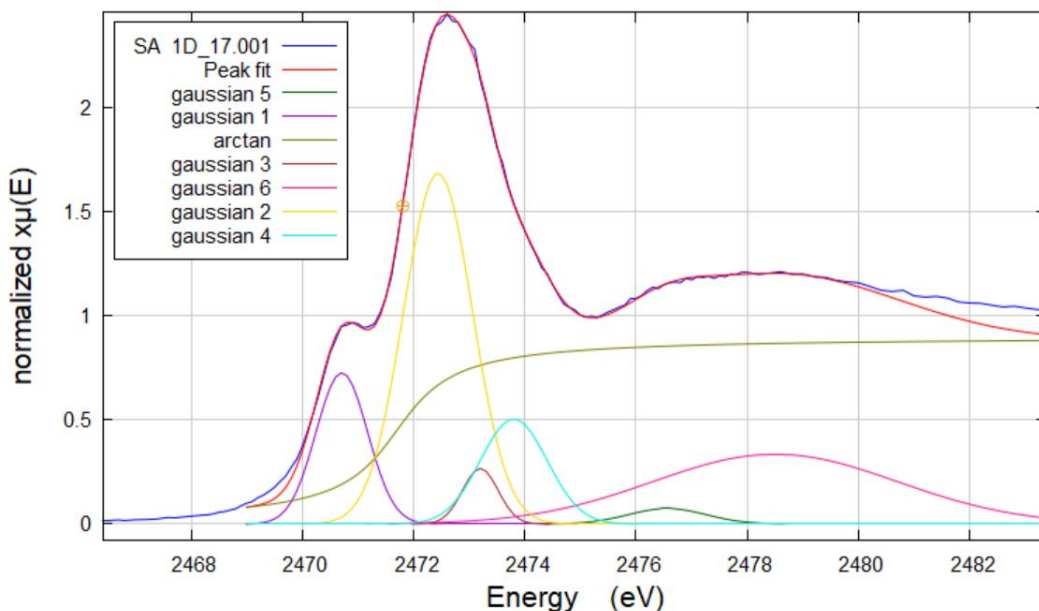


Figure S5.1. Example of fitting a discharge XAS spectra with 6 Gaussian peaks and a step function: 1 Gaussian centered at 2470.71 eV for the pre-edge peak, 2 Gaussians centered at 2472.44 eV and 2473.20 eV for the main-edge peak, 1 Gaussian centered at 2473.80 eV, 1 Gaussian centered at 2476.56 eV, and 1 Gaussian centered at 2478.50 eV.

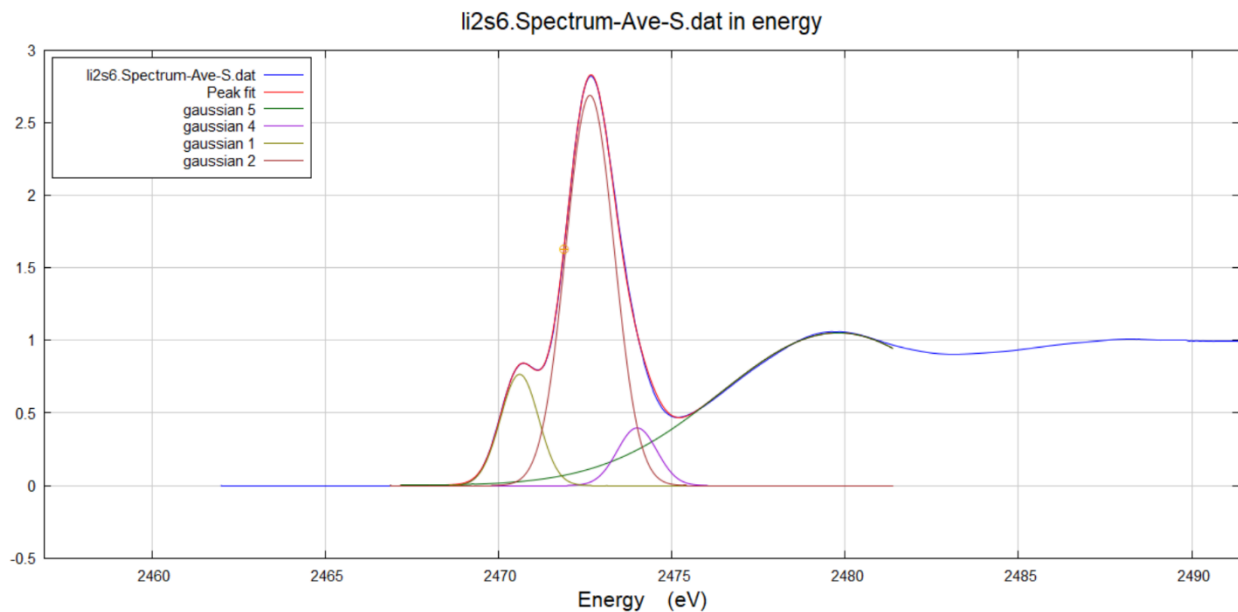


Figure S5.2. Example of fitting a theoretical XAS spectra ( $\text{Li}_2\text{S}_6$ ) with 1 Gaussian peak centered at 2470.61 eV for the pre-edge peak and 2 Gaussian peaks centered at 2472.64 eV and 2474.00 eV for the main-edge peak due to the skewness in the main-edge peak.

Note that equation (8) differs slightly from our previous work. The refitting used two Gaussian peaks instead of one to fit the main-edge peak to improve overall fitting due to the skewness in the main-edge peak.

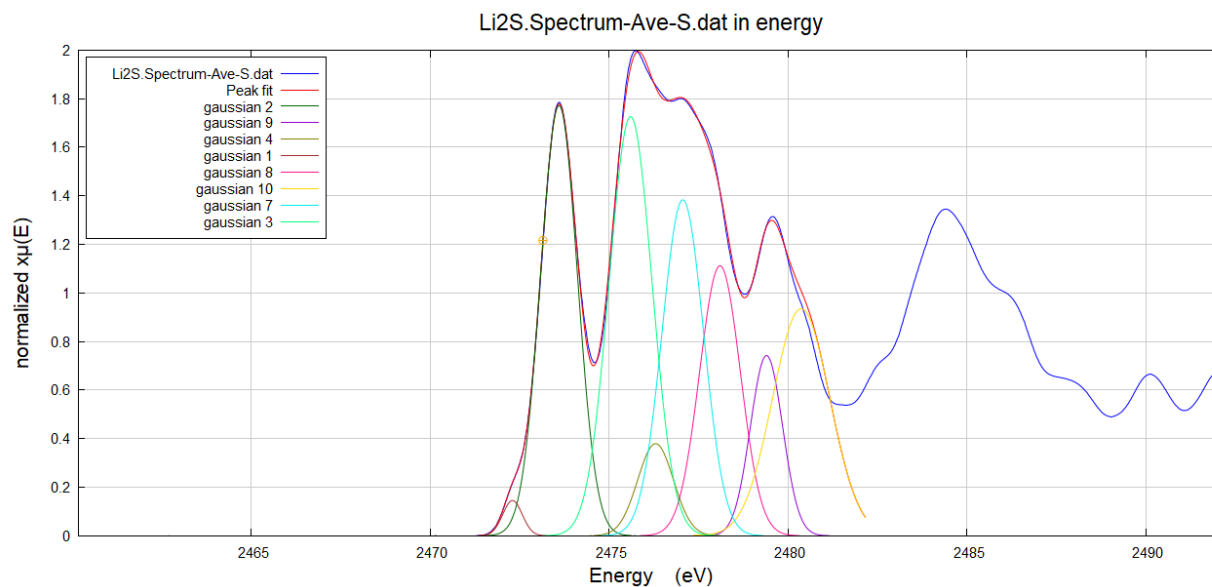


Figure S3. Fitting  $\text{Li}_2\text{S}$  theoretical XAS spectrum with 10 Gaussian peaks centered at 2472.30 eV, 2473.60 eV, 2475.60 eV, 2476.30 eV, 2477.06 eV, 2478.10 eV, 2479.40 eV, and 2480.37 eV. The sum of the areas under peaks centered at 2475.60 eV and 2476.30 eV is  $A_s^{\text{Th}}$ .

## Chapter 6 – Summary

Li-S batteries are well-known for their high theoretical specific energy density and specific capacity. However, significant capacity fading and limited cycle life due to the dissolution of lithium polysulfide intermediate species formed during discharge prevents the commercialization of rechargeable Li-S batteries. Design mechanism requires a better understanding of the reactions during discharge and charge in order to make a better battery. The objective of this study is to answer some of the fundamental questions related to lithium polysulfides such as which lithium polysulfides are produced and when they are formed during discharge, and once they are formed, how do they interact with other components in the cathode such as the electrolyte. We used a polystyrene-*b*-poly(ethylene oxide) (SEO) block copolymer as our separator as well as the solvent of the electrolyte.

In chapter 2, we presented the first measurements of ionic conductivity of the polysulfides in a nanostructured block copolymer. Polysulfides were found to not only dissolve, but also dissociate in an ether-based electrolyte. SAXS measurements on SEO/Li<sub>2</sub>S<sub>x</sub> mixtures revealed a lamellar morphology. DSC measurements indicated that SEO/Li<sub>2</sub>S<sub>8</sub> interactions were more favorable than SEO/Li<sub>2</sub>S<sub>4</sub> interactions. The effect of nanostructure on transport of Li<sub>2</sub>S<sub>x</sub> was quantified by calculating a normalized conductivity, which is proportional to the ratio of the conductivity of SEO/Li<sub>2</sub>S<sub>x</sub> to that of the PEO/Li<sub>2</sub>S<sub>x</sub>. The normalized conductivities of both polysulfides peaked at intermediate concentrations, indicating that lithium polysulfides acted as a conductive salt in the nano-structured block copolymer. The efficacy of block copolymer electrolytes in Li-S batteries was evaluated by comparing ionic conductivities of polymer electrolytes containing Li<sub>2</sub>S<sub>x</sub> with those containing lithium bis(trifluoromethanesulfonyl)imide (LiTFSI), a common salt used in PEO-based battery electrolytes. The transport of Li<sub>2</sub>S<sub>x</sub> species in SEO is suppressed by factors ranging from 0.4 to 0.04 relative to LiTFSI, depending on *x* and salt concentration.

In Chapter 3, we used UV-vis spectroscopy to investigate Li-S reaction products. UV-vis spectra were taken for chemically synthesized lithium polysulfides. Evidence of polysulfide radical anions suggested that once formed, polysulfide radicals are stable in an ether-based electrolyte. The spectra curve and peak locations depended on the average state of discharge, as well as sulfur concentrations. Lack of spectra standards limited our ability to differentiate different species. In-situ study is challenging due to the short penetration depth of UV-vis radiation through sulfur-containing materials. We therefore discussed the potential use of a perfluoropolyether (PFPE) electrolyte in in-situ studies using UV-vis spectroscopy. Ex-situ UV-vis analysis of cells with and without the PFPE electrolyte confirmed that the amount of polysulfides dissolved in PFPE was below the detection limit of a UV-vis spectrometer.

In Chapter 4, we aim at producing reliable UV-vis spectra standards for lithium polysulfides dissolved in an ether environment using computational methods. By comparing two methods within Time-Dependent Density Functional Theory (TDDFT) calculations, Gaussian approximation method and plane wave approximation method, we systematically explored the necessary steps needed to produce physically representative optical spectra in these systems.

Explicit solvent molecules are important for capturing the local solvent-solute interactions between polysulfides and ether solvents. For a large system such as lithium polysulfides with explicit ether solvents, plane-wave calculations are efficient at achieving numerical convergence. A high level of functional to approximate the exchange-correlation function such as cam-b3lyp or higher is needed to calculate reliable spectra, but we currently lack the computational power to do these calculations.

Lastly, in Chapter 5, we performed Li-S discharge mechanism study using in operando X-ray Absorption Spectroscopy (XAS). In operando XAS spectra were taken before throughout the charge-discharge cycle. Lack of variation in the total amount of sulfur species detected indicated that all sulfur-containing species through the entire depth of a Li-S cell were captured. By calculating the average value of polysulfide chain-length,  $x$  in  $\text{Li}_2\text{S}_x$ , using the peak ratio analysis method, we examined the relationship between the state of redox reduction reactions and the number of electrons actually passed in a Li-S cell during galvanostatic discharge. We also proposed a series of reaction mechanism based on the analysis. During the higher voltage plateau, while a small amount of  $\text{S}_8$  was converted to  $\text{Li}_2\text{S}_8$ , the major electrochemical reaction was the reduction of  $\text{Li}_2\text{S}_8$  to  $\text{Li}_2\text{S}_6$  (about 75%). During the transition region between the two plateaus,  $\text{Li}_2\text{S}_8$  continued to be reduced to  $\text{Li}_2\text{S}_6$  while almost half  $\text{Li}_2\text{S}_6$  was reduced to  $\text{Li}_2\text{S}_4$ . The lower voltage plateau was longer than the other two regions, and was associated with the formation of solid phase products such as  $\text{Li}_2\text{S}_2$  and  $\text{Li}_2\text{S}$  both electrochemically and chemically. The early formation of  $\text{Li}_2\text{S}$  in this region suggested that chemical disproportionation reactions played an important role in the formation of  $\text{Li}_2\text{S}$ .

## Chapter 7 – References

1. Pascal, T. a *et al.* The X-ray Absorption Spectra of Dissolved Polysulfides in Lithium – Sulfur Batteries from First Principles. (2014). doi:10.1021/jz500260s
2. Armand, M. & Tarascon, J. M. Building better batteries. *Nature* **451**, 652–657 (2008).
3. Song, M.-K., Cairns, E. J. & Zhang, Y. Lithium/sulfur batteries with high specific energy: old challenges and new opportunities. *Nanoscale* **5**, 2186 (2013).
4. Bruce, P. G., Freunberger, S. a., Hardwick, L. J. & Tarascon, J.-M. Li–O<sub>2</sub> and Li–S batteries with high energy storage. *Nat. Mater.* **11**, 172–172 (2011).
5. Girishkumar, G., McCloskey, B., Luntz, A. C., Swanson, S. & Wilcke, W. Lithium-air battery: Promise and challenges. *J. Phys. Chem. Lett.* **1**, 2193–2203 (2010).
6. Imanishi, N. & Yamamoto, O. Rechargeable lithium-air batteries: Characteristics and prospects. *Mater. Today* **17**, 24–30 (2014).
7. Zhao, E. *et al.* Advanced Characterization Techniques in Promoting Mechanism Understanding for Lithium-Sulfur Batteries. *Adv. Funct. Mater.* **1707543**, 1–21 (2018).
8. Manthiram, A., Fu, Y., Chung, S., Zu, C. & Su, Y. Rechargeable Lithium – Sulfur Batteries. *Chem. Rev.* **114**, 11751–87 (2014).
9. Akridge, J. R., Mikhaylik, Y. V. & White, N. Li/S fundamental chemistry and application to high-performance rechargeable batteries. *Solid State Ionics* **175**, 243–245 (2004).
10. Zheng, D. *et al.* The Progress of Li – S Batteries — Understanding of the Sulfur Redox Mechanism : Dissolved Polysulfide Ions in the Electrolytes. **1700233**, (2018).
11. Mikhaylik, Y. V. & Akridge, J. R. Polysulfide shuttle study in the Li/S battery system. *J. Electrochem. Soc.* **151**, A1969–A1976 (2004).
12. Wang, J. L., Yang, J., Xie, J. Y., Xu, N. X. & Li, Y. Sulfur - Carbon nano-composite as cathode for rechargeable lithium battery based on gel electrolyte. *Electrochem. commun.* **4**, 499–502 (2002).
13. Ji, X., Lee, K. T. & Nazar, L. F. A highly ordered nanostructured carbon-sulphur cathode for lithium-sulphur batteries. *Nat. Mater.* **8**, 500–506 (2009).
14. Fu, Y. & Manthiram, A. Orthorhombic bipyramidal sulfur coated with polypyrrole nanolayers as a cathode material for lithium-sulfur batteries. *J. Phys. Chem. C* **116**, 8910–8915 (2012).
15. Simmonds, A. G. *et al.* Inverse vulcanization of elemental sulfur to prepare polymeric electrode materials for Li-S batteries. *ACS Macro Lett.* **3**, 229–232 (2014).
16. Jung, Y. *et al.* Effect of Organic Solvents and Electrode Materials on Electrochemical Reduction of Sulfur. *Int. J. Electrochem. Sci.* **3**, 566–577 (2008).

17. Lu, Y. C., He, Q. & Gasteiger, H. A. Probing the lithium-sulfur redox reactions: A rotating-ring disk electrode study. *J. Phys. Chem. C* **118**, 5733–5741 (2014).
18. Waluś, S. *et al.* New insight into the working mechanism of lithium-sulfur batteries: in situ and operando X-ray diffraction characterization. *Chem. Commun. (Camb)*. **49**, 7899–901 (2013).
19. Nelson, J. *et al.* In operando X-ray Diffraction and Transmission X-ray Microscopy of Lithium Sulfur Batteries In operando X-ray Diffraction and Transmission X-ray Microscopy of Lithium Sulfur Batteries. *J. Am. Chem. Soc.* **134**, 6337–6343 (2012).
20. Lowe, M. A., Gao, J. & Abruña, H. D. Mechanistic insights into operational lithium-sulfur batteries by in situ X-ray diffraction and absorption spectroscopy. *RSC Adv.* **4**, 18347 (2014).
21. Cañas, N. A., Wolf, S., Wagner, N. & Friedrich, K. A. In-situ X-ray diffraction studies of lithium-sulfur batteries. *J. Power Sources* **226**, 313–319 (2013).
22. See, K. A. *et al.* Ab initio structure search and in situ <sup>7</sup>Li NMR studies of discharge products in the Li-S battery system. *J. Am. Chem. Soc.* **136**, 16368–16377 (2014).
23. Barchasz, C., Molton, F. & Duboc, C. Lithium/Sulfur Cell Discharge Mechanism: An Original Approach for Intermediate Species Identification. *Anal. Chem.* **84**, 3973–3980 (2012).
24. Cañas, N. a., Fronczek, D. N., Wagner, N., Latz, A. & Friedrich, K. A. Experimental and Theoretical Analysis of Products and Reaction Intermediates of Lithium–Sulfur Batteries. *J. Phys. Chem. C* **118**, 12106–12114 (2014).
25. Wujcik, K. H. *et al.* Lithium Polysulfide Radical Anions in Ether-Based Solvents. *J. Phys. Chem. C* **120**, 18403–18410 (2016).
26. Hagen, M. *et al.* In-Situ Raman Investigation of Polysulfide Formation in Li-S Cells. *J. Electrochem. Soc.* **160**, A1205–A1214 (2013).
27. Wu, H. L., Huff, L. A. & Gewirth, A. A. In situ raman spectroscopy of sulfur speciation in lithium-sulfur batteries. *ACS Appl. Mater. Interfaces* **7**, 1709–1719 (2015).
28. Wujcik, K. H., Wang, D. R., Pascal, T. A., Prendergast, D. & Balsara, N. P. In Situ X-ray Absorption Spectroscopy Studies of Discharge Reactions in a Thick Cathode of a Lithium Sulfur Battery. *J. Electrochem. Soc.* **164**, A18–A27 (2017).
29. Wild, M. *et al.* Lithium sulfur batteries, a mechanistic review. *Energy Environ. Sci.* **8**, 3477–3494 (2015).
30. Rauh, R. D., Abraham, K. M., Pearson, G. F., Surprenant, J. K. & Brummer, S. B. A Lithium/Dissolved Sulfur Battery with an Organic Electrolyte. *J. Electrochem. Soc.* **126**, 523–527 (1979).
31. Yamin, H. Lithium Sulfur Battery. *J. Electrochem. Soc.* **135**, 1045 (1988).

32. Kolosnitsyn, V. S. & Karaseva, E. V. Lithium-sulfur batteries: Problems and solutions. *Russ. J. Electrochem.* **44**, 506–509 (2008).
33. Cheon, S.-E. *et al.* Rechargeable Lithium Sulfur Battery I. *J. Electrochem. Soc.* **150**, A800 (2003).
34. Zheng, G., Yang, Y., Cha, J. J., Hong, S. S. & Cui, Y. Hollow carbon nanofiber-encapsulated sulfur cathodes for high specific capacity rechargeable lithium batteries. *Nano Lett.* **11**, 4462–4467 (2011).
35. Balsara, N. P. & Newman, J. Comparing the energy content of batteries, fuels, and materials. *J. Chem. Educ.* **90**, 446–452 (2013).
36. Aurbach, D., Zinigrad, E., Cohen, Y. & Teller, H. A short review of failure mechanisms of lithium metal and lithiated graphite anodes in liquid electrolyte solutions. *Solid State Ionics* **148**, 405–416 (2002).
37. Goodenough, J. B. & Kim, Y. Challenges for rechargeable Li batteries. *Chem. Mater.* **22**, 587–603 (2010).
38. Harry, K. J., Hallinan, D. T., Parkinson, D. Y., MacDowell, A. a & Balsara, N. P. Detection of subsurface structures underneath dendrites formed on cycled lithium metal electrodes. *Nat. Mater.* **13**, 69–73 (2014).
39. Singh, M. *et al.* Effect of molecular weight on the mechanical and electrical properties of block copolymer electrolytes. *Macromolecules* **40**, 4578–4585 (2007).
40. Panday, A. *et al.* Effect of molecular weight and salt concentration on conductivity of block copolymer electrolytes. *Macromolecules* **42**, 4632–4637 (2009).
41. Mullin, S. a., Stone, G. M., Panday, A. & Balsara, N. P. Salt Diffusion Coefficients in Block Copolymer Electrolytes. *J. Electrochem. Soc.* **158**, A619 (2011).
42. Yuan, R. *et al.* Ionic conductivity of low molecular weight block copolymer electrolytes. *Macromolecules* **46**, 914–921 (2013).
43. Teran, A. a., Tang, M. H., Mullin, S. a. & Balsara, N. P. Effect of molecular weight on conductivity of polymer electrolytes. *Solid State Ionics* **203**, 18–21 (2011).
44. Chintapalli, M. *et al.* Effect of grain size on the ionic conductivity of a block copolymer electrolyte. *Macromolecules* **47**, 5424–5431 (2014).
45. Stone, G. M. *et al.* Resolution of the Modulus versus Adhesion Dilemma in Solid Polymer Electrolytes for Rechargeable Lithium Metal Batteries. *J. Electrochem. Soc.* **159**, A222 (2012).
46. Monroe, C. & Newman, J. The Impact of Elastic Deformation on Deposition Kinetics at Lithium/Polymer Interfaces. *J. Electrochem. Soc.* **152**, A396–A404 (2005).
47. Newman, J. & Thomas-Alyea, K. E. *Electrochemical Systems*. (John Wiley & Sons, 2012).

48. Seyferth, D. Sulfur in Organic and Inorganic Chemistry. *Organometallics* **1**, 1555 (1982).
49. Kamyshny, A., Goifman, A., Gun, J., Rizkov, D. & Lev, O. Equilibrium distribution of polysulfide ions in aqueous solutions at 25 degrees C: a new approach for the study of polysulfides' equilibria. *Environ. Sci. Technol.* **38**, 6633–6644 (2004).
50. Wujcik, K. H. *et al.* Fingerprinting Lithium-Sulfur Battery Reaction Products by X-ray Absorption Spectroscopy. *J. Electrochem. Soc.* **161**, A1100–A1106 (2014).
51. Chang, D., Lee, S., Kim, S. & Kim, H. Binary electrolyte based on tetra ( ethylene glycol ) dimethyl ether and 1 , 3-dioxolane for lithium – sulfur battery. *Change* **112**, 452–460 (2002).
52. Agostini, M. & Hassoun, J. A lithium-ion sulfur battery using a polymer, polysulfide-added membrane. *Sci. Rep.* **5**, 7591 (2015).
53. Teran, A. a. & Balsara, N. P. Effect of lithium polysulfides on the morphology of block copolymer electrolytes. *Macromolecules* **44**, 9267–9275 (2011).
54. Chen, S., Dai, F., Gordin, M. L. & Wang, D. Exceptional electrochemical performance of rechargeable Li-S batteries with a polysulfide-containing electrolyte. *RSC Adv.* **3**, 3540–3543 (2013).
55. Barghamadi, M., Kapoor, A. & Wen, C. A Review on Li-S Batteries as a High Efficiency Rechargeable Lithium Battery. *J. Electrochem. Soc.* **160**, A1256–A1263 (2013).
56. Su, Y.-S., Fu, Y., Cochell, T. & Manthiram, A. A strategic approach to recharging lithium-sulphur batteries for long cycle life. *Nat. Commun.* **4**, 2985 (2013).
57. Hexemer, A. *et al.* A SAXS/WAXS/GISAXS beamline with multilayer monochromator. *J. Phys. Conf. Ser.* **247**, (2010).
58. Ilavsky, J. *et al.* High-energy ultra-small-angle X-ray scattering instrument at the Advanced Photon Source. *J. Appl. Crystallogr.* **45**, 1318–1320 (2012).
59. Huggins, R. A. Simple method to determine electronic and ionic components of the conductivity in mixed conductors a review. *Ionics (Kiel)*. **8**, 300–313 (2002).
60. Devaux, D., Bouchet, R., Glé, D. & Denoyel, R. Mechanism of ion transport in PEO/LiTFSI complexes: Effect of temperature, molecular weight and end groups. *Solid State Ionics* **227**, 119–127 (2012).
61. Simon, F. T. & Rutherford, J. M. Crystallization and melting behavior of polyethylene oxide copolymers. *J. Appl. Phys.* **35**, 82–86 (1964).
62. Li, X. & Hsu, S. L. An analysis of the crystallization behavior of poly(ethylene oxide)/poly(methyl methacrylate) blends by spectroscopic and calorimetric techniques. *J. Polym. Sci. Polym. Phys. Ed.* **22**, 1331–1342 (1984).
63. Przylusky, J. & Wiczorek, W. DSC Studies of Polymeric Electrolytes. **38**, 2229–2238 (1992).



64. Wieczorek, W. Composite polyether based solid electrolytes. The Lewis acid-base approach. *Solid State Ionics* **85**, 67–72 (1996).
65. Pielichowski, K. & Flejtuch, K. Differential scanning calorimetry studies on poly(ethylene glycol) with different molecular weights for thermal energy storage materials. *Polym. Adv. Technol.* **13**, 690–696 (2002).
66. Lin, J.-H., Woo, E. M. & Huang, Y.-P. Effect of Lithium Salt and Poly(4-vinyl phenol) on Crystalline and Amorphous Phases in Poly(ethylene oxide). *J. Polym. Sci. Part B Polym. Phys.* **44**, 3357–3368 (2006).
67. Minelli, M., Giacinti Baschetti, M., Hallinan, D. T. & Balsara, N. P. Study of gas permeabilities through polystyrene-block-poly(ethylene oxide) copolymers. *J. Memb. Sci.* **432**, 83–89 (2013).
68. *Polymer Electrolyte Reviews*. (Elsevier Applied Science, 1987).
69. Lascaud, S. *et al.* Phase Diagrams and Conductivity Behavior of Poly(ethylene oxide)-Molten Salt Rubbery Electrolytes. *Macromolecules* **27**, 7469–7477 (1994).
70. Mikhaylik, Y. V. & Akridge, J. R. Polysulfide Shuttle Study in the Li/S Battery System. *J. Electrochem. Soc.* **151**, A1969 (2004).
71. Marmorstein, D. *et al.* Electrochemical performance of lithium-sulfur cells with three different polymer electrolytes. *J. Power Sources* **89**, 219–226 (2000).
72. Steudel, R. Inorganic Polysulfides  $S_n^{2-}$  and Radical Anions  $S_n^{\cdot-}$ . *Top. Curr. Chem.* 127–152 (2003). doi:10.1007/b13183
73. Yang, G., Shi, S., Yang, J. & Ma, Y. Insight into the role of  $Li_2S_2$  in Li–S batteries: a first-principles study. *J. Mater. Chem. A* **3**, 8865–8869 (2015).
74. Paoella, A. *et al.* Transient existence of crystalline lithium disulfide  $Li_2S_2$  in a lithium-sulfur battery. *J. Power Sources* **325**, 641–645 (2016).
75. Liu, Z., Balbuena, P. B. & Mukherjee, P. P. Revealing Charge Transport Mechanisms in  $Li_2S_2$  for Li–Sulfur Batteries. *J. Phys. Chem. Lett.* **8**, 1324–1330 (2017).
76. Lux, H. & Benninger, S. Losungen des Schwefels in Dimethylformamid. **2493**, 2485–2493 (1968).
77. Giggenbach, W. On the nature of the blue solution of sulfur. *J. Inorg. Nucl. Chem.* **30**, 3189–3201 (1968).
78. Gruen, D. M., Mcbeth, R. L. & Zielen, A. J. Nature of Sulfur Species in Fused Salt Solutions. *J. Am. Chem. Soc.* **93**, 6691–6693 (1971).
79. Chivers, T. & Drummond, I. Characterization of the Trisulfur Radical Anion  $S_3^-$  in Blue Solutions of Alkali Polysulfides in Hexamethylphosphoramide. *Inorg. Chem.* **141**, 18–20 (1972).

80. Reinen, D. & Lindner, G.-G. The nature of the chalcogen color centers in ultramarine-type solids. *Chem. Soc. Rev.* **28**, 75–84 (1999).
81. Martin, R. P., Doub, W. H., Roberts, J. L. & Sawyer, D. T. Further Studies of the Electrochemical Reduction of Sulfur in Aprotic Solvents. *Inorg. Chem.* **12**, 1921–1925 (1973).
82. Kim, B.-S. In Situ Spectroelectrochemical Studies on the Reduction of Sulfur in Dimethyl Sulfoxide Solutions. *J. Electrochem. Soc.* **140**, 115 (1993).
83. Paris, J. & Plichon, V. Electrochemical reduction of sulphur in dimethylacetamide. *Electrochim. Acta* **26**, 1823–1829 (1981).
84. Levillain, E., Gaillard, F. & Lelieur, J. P. Polysulfides in dimethylformamide: only the redox couples S-n(-)/S-n(2-) involved. *J. Electroanal. Chem.* **440**, 243–250 (1997).
85. Tobishima, S. I., Yamamoto, H. & Matsuda, M. Study on the reduction species of sulfur by alkali metals in nonaqueous solvents. *Electrochim. Acta* **42**, 1019–1029 (1997).
86. Manan, N. S. A. *et al.* Electrochemistry of sulfur and polysulfides in ionic liquids. *J. Phys. Chem. B* **115**, 13873–13879 (2011).
87. Patel, M. U. M. & Dominko, R. Application of in operando UV/Vis spectroscopy in lithium-sulfur batteries. *ChemSusChem* **7**, 2167–2175 (2014).
88. Casida, M. E. & Huix-Rotllant, M. Progress in Time-Dependent Density-Functional Theory. (2011). doi:10.1146/annurev-physchem-032511-143803
89. González, L., Escudero, D. & Serrano-Andrés, L. Progress and challenges in the calculation of electronic excited states. *ChemPhysChem* **13**, 28–51 (2012).
90. Maitra, N. T. Perspective: Fundamental aspects of time-dependent density functional theory. *J. Chem. Phys.* **144**, (2016).
91. Kawase, A., Shirai, S., Yamoto, Y., Arakawa, R. & Takata, T. Electrochemical reactions of lithium-sulfur batteries: An analytical study using the organic conversion technique. *Phys. Chem. Chem. Phys.* **16**, 9344–9350 (2014).
92. Shao, Y. *et al.* Advances in molecular quantum chemistry contained in the Q-Chem 4 program package. *Mol. Phys.* **113**, 184–215 (2015).
93. Giannozzi, P. *et al.* Quantum ESPRESSO: a modular and open-source software project for quantum simulations of materials. (2009). doi:10.1088/0953-8984/21/39/395502
94. Dunning, T. H. Gaussian basis sets for use in correlated molecular calculations. I. The atoms boron through neon and hydrogen. *J. Chem. Phys.* **90**, 1007–1023 (1989).
95. Rappoport, D., Crawford, N. R. M., Furche, F. & Burke, K. Approximate Density Functionals: Which Should I Choose? *Encycl. Inorg. Chem.* (2009). doi:10.1002/0470862106.ia615

96. Burke, K. & Wagner, L. O. DFT in a nutshell. *Int. J. Quantum Chem.* **113**, 96–101 (2013).
97. Roux, B. & Simonson, T. Implicit solvent models. *Biophys. Chem.* **78**, 1–20 (1999).
98. Ji, X. & Nazar, L. F. Advances in Li-S batteries. *J. Mater. Chem.* **20**, 9821–9826 (2010).
99. Manthiram, A., Fu, Y. & Su, Y. S. Challenges and prospects of lithium-sulfur batteries. *Acc. Chem. Res.* **46**, 1125–1134 (2013).
100. Yin, Y. X., Xin, S., Guo, Y. G. & Wan, L. J. Lithium-sulfur batteries: Electrochemistry, materials, and prospects. *Angew. Chemie - Int. Ed.* **52**, 13186–13200 (2013).
101. Pascal, T. A. *et al.* Liquid Sulfur Impregnation of Microporous Carbon Accelerated by Nanoscale Interfacial Effects. *Nano Lett.* **17**, 2517–2523 (2017).
102. Wang, D. R., Wujcik, K. H., Teran, A. A. & Balsara, N. P. Conductivity of Block Copolymer Electrolytes Containing Lithium Polysulfides. *Macromolecules* **48**, 4863–4873 (2015).
103. Han, D.-H. *et al.* Time-Resolved In Situ Spectroelectrochemical Study on Reduction of Sulfur in N,N[<sup>sup</sup>']-Dimethylformamide. *J. Electrochem. Soc.* **151**, E283 (2004).
104. Nelson, J. *et al.* *In operando* X-ray Diffraction and Transmission X-ray Microscopy of Lithium Sulfur Batteries. *In operando X-ray Diffraction and Transmission X-ray Microscopy of Lithium Sulfur Batteries.* (2012). doi:10.1021/ja2121926
105. A. Huff, L., L. Rapp, J., Baughman, J., Rinaldi, P. & Gewirth, A. *Identification of lithium-sulfur battery discharge products through <sup>6</sup>Li and <sup>33</sup>S solid-state MAS and <sup>7</sup>Li solution NMR spectroscopy.* *Surface Science* **631**, (2014).
106. Gao, J., Lowe, M. A., Kiya, Y. & Abruña, H. D. Effects of liquid electrolytes on the charge-discharge performance of rechargeable lithium/sulfur batteries: Electrochemical and in-situ X-ray absorption spectroscopic studies. *J. Phys. Chem. C* **115**, 25132–25137 (2011).
107. Lowe, M. a., Gao, J. & Abruña, H. D. Mechanistic insights into operational lithium–sulfur batteries by in situ X-ray diffraction and absorption spectroscopy. *RSC Adv.* **4**, 18347 (2014).
108. Cuisinier, M. *et al.* Sulfur Speciation in Li – S Batteries Determined by Operando X - ray Absorption Spectroscopy. *J. Phys. Chemistry Lett.* **4**, 3227–3232 (2013).
109. Cuisinier, M. *et al.* Unique behaviour of nonsolvents for polysulphides in lithium–sulphur batteries. *Energy Environ. Sci.* **7**, 2697 (2014).
110. Cuisinier, M., Hart, C., Balasubramanian, M., Garsuch, A. & Nazar, L. F. Radical or Not Radical: Revisiting Lithium-Sulfur Electrochemistry in Nonaqueous Electrolytes. *Adv. Energy Mater.* **5**, 1–6 (2015).
111. Dominko, R. *et al.* Analytical Detection of Polysulfides in the Presence of Adsorption Additives by Operando X-ray Absorption Spectroscopy. *J. Phys. Chem. C* **119**, 19001–

- 19010 (2015).
112. Wujcik, K. H. *et al.* Characterization of Polysulfide Radicals Present in an Ether-Based Electrolyte of a Lithium-Sulfur Battery during Initial Discharge Using in Situ X-Ray Absorption Spectroscopy Experiments and First-Principles Calculations. *Adv. Energy Mater.* **5**, (2015).
  113. Gorlin, Y. *et al.* Operando Characterization of Intermediates Produced in a Lithium-Sulfur Battery. *J. Electrochem. Soc.* **162**, A1146–A1155 (2015).
  114. Gorlin, Y. *et al.* Understanding the Charging Mechanism of Lithium-Sulfur Batteries Using Spatially Resolved Operando X-Ray Absorption Spectroscopy. *J. Electrochem. Soc.* **163**, A930–A939 (2016).
  115. Zhang, L., Sun, D., Feng, J., Cairns, E. J. & Guo, J. Revealing the electrochemical charging mechanism of nano-sized Li<sub>2</sub>S by in-situ and operando X-ray absorption spectroscopy. *Nano Lett.* [acs.nanolett.7b02381](https://doi.org/10.1021/acs.nanolett.7b02381) (2017). doi:10.1021/acs.nanolett.7b02381
  116. Miller, E. C., Kasse, R. M., Heath, K. N., Perdue, B. R. & Toney, M. F. Operando Spectromicroscopy of Sulfur Species in Lithium-Sulfur Batteries. *J. Electrochem. Soc.* **165**, A6043–A6050 (2018).
  117. Wujcik, K. H., Velasco-velez, J., Hao, C., Pascal, T. & Teran, A. A. Fingerprinting lithium - sulfur battery reaction products by X - ray absorption spectroscopy.
  118. Ye, Y. *et al.* X-ray Absorption Spectroscopy Characterization of a Li/S Cell. *Nanomaterials* **6**, 14 (2016).
  119. Patel, M. U. M. *et al.* X-ray Absorption Near-Edge Structure and Nuclear Magnetic Resonance Study of the Lithium-Sulfur Battery and its Components. *ChemPhysChem* **15**, 894–904 (2014).
  120. Zhang, L., Sun, D., Feng, J., Cairns, E. J. & Guo, J. Revealing the electrochemical charging mechanism of nanosized Li<sub>2</sub>S by in situ and operando X-ray absorption spectroscopy. *Nano Lett.* **17**, 5084–5091 (2017).
  121. Hadjichristidis, N., Iatrou, H., Pispas, S. & Pitsikalis, M. Anionic polymerization: high vacuum techniques. *J. Polym. Sci. Part A Polym. Chem.* **38**, 3211–3234 (2000).
  122. Berkeley, U. C. & Andrew, A. Block Copolymer Electrolytes : Thermodynamics , Ion Transport , and Use in Solid- State Lithium / Sulfur Cells By Alexander Andrew Teran A dissertation submitted in partial satisfaction of the requirements for the degree of Doctor of Philosophy in Chemica. (2013).
  123. Pascal, T. A., Wujcik, K. H., Wang, D. R., Balsara, N. P. & Prendergast, D. Thermodynamic origins of the solvent-dependent stability of lithium polysulfides from first principles. *Phys. Chem. Chem. Phys.* **19**, 1441–1448 (2017).
  124. Waluš, S. *et al.* Lithium/Sulfur Batteries Upon Cycling: Structural Modifications and Species Quantification by in Situ and Operando X-Ray Diffraction Spectroscopy. *Adv.*

- Energy Mater.* **5**, 1–5 (2015).
125. Conder, J. *et al.* Direct observation of lithium polysulfides in lithium-sulfur batteries using operando X-ray diffraction. *Nat. Energy* **2**, 1–7 (2017).
  126. Wang, G., Zheng, D., Liu, D., Yang, X. Q. & Qu, D. Sulfur redox reactions on nanostructured highly oriented pyrolytic graphite (HOPG) electrodes: Direct evidence for superior electrocatalytic performance on defect sites. *Carbon N. Y.* **119**, 460–463 (2017).
  127. Patel, M. U. M. *et al.* Li-S battery analyzed by UV/vis in operando mode. *ChemSusChem* **6**, 1177–1181 (2013).
  128. Dominko, R., Patel, M. U. M., Bele, M. & Pejovnik, S. Sulphured Polyacrylonitrile Composite Analysed by in operando UV-Visible Spectroscopy and 4-electrode Swagelok Cell. *Acta Chim. Slov.* 569–577 (2016). doi:10.17344/acsi.2016.2366
  129. Zou, Q. & Lu, Y. C. Solvent-Dictated Lithium Sulfur Redox Reactions: An Operando UV-vis Spectroscopic Study. *J. Phys. Chem. Lett.* **7**, 1518–1525 (2016).
  130. Wang, Q. *et al.* Direct Observation of Sulfur Radicals as Reaction Media in Lithium Sulfur Batteries. *J. Electrochem. Soc.* **162**, A474–A478 (2015).